FEDERAL UNIVERSITY OF JUIZ DE FORA

COLLEGE OF ENGINEERING

GRADUATE PROGRAM IN COMPUTATIONAL MODELING

Tatiana Danelon de Assis

Modeling nanoparticle-stabilized foam flow in porous media: Mathematical analysis and uncertainty quantification

Juiz de Fora

2024

Tatiana Danelon de Assis

Modeling nanoparticle-stabilized foam flow in porous media: Mathematical analysis and uncertainty quantification

Thesis submitted to the Graduate Program in Computational Modeling in Federal University of Juiz de Fora, as partial fulfillment of the requirements for the degree of Doctor in Computational Modeling.

Advisor: Prof. D.Sc. Grigori Chapiro

Juiz de Fora

2024

Ficha catalográfica elaborada através do Modelo Latex do CDC da UFJF
com os dados fornecidos pelo(a) autor(a)

Danelon, Tatiana.
Modeling nanoparticle-stabilized foam flow in porous media: Mathematical analysis and uncertainty quantification / Tatiana Danelon de Assis. – 2024.
127 f. : il.

Advisor: Grigori Chapiro
Doctorate Thesis – Federal University of Juiz de Fora, College of engineering. Graduate Program in Computational Modeling, 2024.

1. Nanoparticle-stabilized foam. 2. Porous media. 3. Non-strictly hyperbolic conservation laws. 4. Uncertainty quantification. 5. Sensitivity analysis. I. Chapiro, Grigori, orient. II. Título.

Tatiana Danelon de Assis

Modeling nanoparticle-stabilized foam flow in porous media: Mathematical analysis and uncertainty quantification

Tese apresentada ao Programa de Pós-Graduação em Modelagem Computacional da Universidade Federal de Juiz de Fora como requisito parcial à obtenção do título de Doutora em Modelagem Computacional. Área de concentração: Modelagem Computacional.

Aprovada em 13 de janeiro de 2025.

BANCA EXAMINADORA

Prof. Dr. Grigori Chapiro - Orientador

Universidade Federal de Juiz de Fora

Prof.Dr. Bernardo Martins Rocha

Universidade Federal de Juiz de Fora

Prof. Dr. Pavel Bedrikovetsky

Adelaide University (Adelaide, Austrália)

Prof. Dr. Rouhi Farajzadeh

Delft University of Technology (Delft, Países Baixos)

Shell International Ltd.

Prof. Dr. Denis Voskov

Delft University of Technology (Delft, Países Baixos)

Juiz de Fora, 19/12/2024.

Documento assinado eletronicamente por **Grigori Chapiro**, **Professor(a)**, em 13/01/2025, às 08:24, conforme horário oficial de Brasília, com fundamento no § 3º do art. 4º do Decreto nº 10.543, de 13 de novembro de 2020.

Documento assinado eletronicamente por **Rouhi Farajzadeh**, **Usuário Externo**, em 13/01/2025, às 08:26, conforme horário oficial de Brasília, com fundamento no § 3º do art. 4º do Decreto nº 10.543, de 13 de novembro de 2020.

Documento assinado eletronicamente por **Denis Viktorovich Voskov**, **Usuário Externo**, em 13/01/2025, às 08:27, conforme horário oficial de Brasília, com fundamento no § 3º do art. 4º do Decreto nº 10.543, de 13 de novembro de 2020.

Documento assinado eletronicamente por **Bernardo Martins Rocha**, **Professor(a)**, em 14/01/2025, às 10:46, conforme horário oficial de Brasília, com fundamento no § 3º do art. 4º do Decreto nº 10.543, de 13 de novembro de 2020.

Documento assinado eletronicamente por **Pavel Bedrikovetski**, **Usuário Externo**, em 14/01/2025, às 11:29, conforme horário oficial de Brasília, com fundamento no § 3º do art. 4º do Decreto nº 10.543, de 13 de novembro de 2020.

A autenticidade deste documento pode ser conferida no Portal do SEI-Ufjf (www2.ufjf.br/SEI) através do ícone Conferência de Documentos, informando o código verificador **2167984** e o código CRC **6F7FB1F0**.

ACKNOWLEDGMENTS

Firstly, I would like to thank my advisor, Prof. Grigori Chapiro, for his guidance and support throughout my research.

Since this thesis involves different areas, many people contributed to each of them. I am thankful to each co-author of the articles produced during my doctoral studies, as their contributions were essential throughout the entire process. Special thanks to D.Sc. Pavel Sejas and D.Sc. Luis Lozano for their advice on mathematical proofs, and to D.Sc. Juliana Façanha for helpful suggestions regarding the application of this work.

I am also thankful to the Professors of the Graduate Program in Computational Modeling for the knowledge shared over the years, as well as the coordination team and administrative staff for their unwavering support.

I thank the entire LAMAP team for valuable discussions, which were essential in improving the quality of my research. Special thanks to Jhuan Cedro, Gabriel Brandão, Giulia Fritis, and Andrés Castrillon for helping me several times.

I want to thank my husband for his unconditional support, as well as to my parents, family, and friends for their constant encouragement.

Finally, I gratefully acknowledge support from Shell Brasil through the project "Avançando na modelagem matemática e computacional para apoiar a implementação da tecnologia 'Foam-assisted WAG' em reservatórios do Pré-sal" (ANP 23518-4) at UFJF and the strategic importance of the support given by ANP through the R&D levy regulation.

ABSTRACT

This work proposes a local equilibrium model and a population balance model to study foam flow assisted by nanoparticles in porous media. In both cases, we include the nanoparticle effect reducing foam mobility in a version of the Stochastic Bubble Population model, based on literature experimental data for silica nanoparticles. The population balance nanoparticle-stabilized foam model, besides including foam texture as a variable, incorporates particle retention and the resulting permeability reduction.

The local equilibrium model is a non-strictly hyperbolic system of conservation laws. We obtain the global analytical solution, which allows us to quantify the effect of nanoparticles on foam flow. When only gas is injected, the breakthrough time and water production increase with the nanoparticle concentration, but this effect is less pronounced for high concentrations. Counterintuitively, during water-gas co-injection for a certain parameter range, adding nanoparticles yields a negligible effect on water production. We also investigate a simplified version of this model (using quadratic relative permeability functions), allowing for algebraic expressions to construct the solution profiles. We conduct uncertainty quantification and sensitivity analysis for the quadratic model, focusing on breakthrough time, water production, and pressure drop. Nanoparticles significantly reduce uncertainty propagation due to foam stabilization. Our findings indicate that the effect of nanoparticles exceeds the model's uncertainty, suggesting that measuring it experimentally is statistically feasible. We achieve convergence even using the Monte Carlo method, evidencing how analytical solutions drastically reduce computational costs.

For the population balance model, we obtain a semi-analytical solution under steady-state conditions. We study foam flow considering nanoparticle concentrations of 0.1, 0.5, and 1.0 wt%, with and without NaCl, using retention parameters from experiments. Higher concentrations increase foam viscosity, reduce water saturation, and improve sweep efficiency, while 0.1 wt% shows minimal impact. Neglecting nanoparticle retention generally underestimates pressure drop, especially in scenarios with significant retention. However, while retained nanoparticles increase pressure by reducing permeability, the loss of suspended nanoparticles decreases pressure by reducing the foam's apparent viscosity. Consequently, when considering both nanoparticle loss and reduced permeability, the pressure drop is higher than in models that ignore retention. In contrast, omitting retention effects on permeability, the pressure drop is lower.

Keywords: Nanoparticle-stabilized foam. Flow in porous media. Particle retention. Uncertainty quantification. Sensitivity analysis.

RESUMO

Este trabalho propõe um modelo em equilíbrio local e um modelo de balanço populacional para estudar o escoamento de espuma estabilizada por nanopartículas em meios porosos. Em ambos, incluímos o efeito das nanopartículas reduzindo a mobilidade da espuma em uma versão do modelo SBP (*Stochastic Bubble Population model*), com base em experimentos da literatura para nanopartículas de sílica. O modelo de balanço populacional, além de incluir a textura da espuma como variável, incorpora retenção de partículas e redução de permeabilidade.

O modelo em equilíbrio local é um sistema não estritamente hiperbólico de leis de conservação. Obtemos a solução analítica global, que nos permitiu quantificar o efeito das nanopartículas no escoamento de espuma. Quando apenas gás é injetado, o tempo de *breakthrough* e a produção de água aumentam com a concentração de nanopartículas, mas esse efeito é menos pronunciado para altas concentrações. Contraintuitivamente, durante a coinjeção gás-água para uma certa faixa de parâmetros, adicionar nanopartículas resulta em um efeito insignificante na produção de água. Também investigamos uma versão simplificada deste modelo (usando permeabilidades relativas quadráticas), possibilitando expressões algébricas para construir os perfis de solução. Estudamos a propagação de incertezas e sensibilidade para o modelo quadrático, com foco no tempo de *breakthrough*, produção de água e queda de pressão. As nanopartículas reduzem significativamente a propagação da incertezas devido à estabilização da espuma. Os resultados sugerem que seria estatisticamente viável medir o efeito das nanopartículas experimentalmente. Atingimos a convergência mesmo usando o método de Monte Carlo, evidenciando como as soluções analíticas reduzem drasticamente os custos computacionais.

Para o modelo de balanço populacional, apresentamos uma solução semi-analítica em estado estacionário. Estudamos o escoamento de espuma considerando concentrações de nanopartículas de 0.1, 0.5 e 1.0 wt%, com e sem NaCl, usando parâmetros de retenção experimentais. Concentrações mais altas aumentam a viscosidade da espuma, reduzem a saturação de água e melhoram a eficiência de varredura, enquanto para 0.1 wt% é insignificante. Negligenciar a retenção de partículas geralmente subestima a queda de pressão, especialmente em cenários com retenção significativa. No entanto, enquanto as nanopartículas retidas aumentam a pressão ao reduzir a permeabilidade, a perda de nanopartículas suspensas diminui a pressão ao reduzir a viscosidade aparente da espuma. Consequentemente, ao considerar tanto a perda de nanopartículas quanto a permeabilidade reduzida, a queda de pressão é maior do que em modelos que ignoram a retenção. Em contraste, omitindo os efeitos da retenção na permeabilidade, a queda de pressão é menor.

Palavras-chave: Espuma estabilizada por nanopartículas. Escoamento em meios porosos. Retenção de partículas. Quantificação de incertezas. Análise de sensibilidade.

LIST OF FIGURES

LIST OF TABLES

LIST OF ABBREVIATIONS AND ACRONYMS

CDF	Cumulative distribution function
CFT	Colloid Filtration Theory
CI	Confidence interval
CFT	Colloid Filtration Theory
CV	Coefficient of variation
EOR	Enhanced oil recovery
FAWAG	Foam-assisted water-alternating-gas
IVP	Initial value problem
LHS	Latin hypercube sampling
LE	Local equilibrium
MC	Monte Carlo
MRF	Mobility reduction factor
NP	Nanoparticles
PDE	Partial differential equation
PI	Prediction interval
PB	Population Balance
QoI	Quantity of interest
RCD	Reaction–convection-diffusion equations solver
SA	Sensitivity analysis
SAG	Surfactant-alternating-gas
SDS	Sodium dodecyl sulfate surfactant
SBP	Stochastic bubble population model
UQ	Uncertainty quantification
WAG	Water-alternating-gas
WP	Cumulative water production

LIST OF SYMBOLS

Conservation laws

$\mathbb{R}^+$	Set of non-negative real numbers
$\mathbb{R}^m$	m-dimensional real space
$\frac{dF}{dv}$, $F'(v)$	Derivative of a function $F(v)$ with respect to v
$\frac{\partial}{\partial v}$, ∂_v	Partial derivative with respect to v
∂_{vv}	Second partial derivative with respect to v
∇	Gradient vector
λ_p	p-th eigenvalue
e_p	p-th eigenvector
$\mathcal{C}^n$	Differentiability class n
σ	Propagation velocity of a discontinuity
U^-, U^+	Left and right states of a single wave
U_L, U_R	Left and right states of the Riemann problem
$U_0(x)$	Initial condition of a IVP
U^I	Inflection point of the flux function
U^*	Convex-hull of the flux function

Two-phase flow in porous media

w, nw	Subscripts for wetting and non-wetting phases (general two-phase flow)
w, g	Subscripts for water and gas phases (water-gas flow)
φ	Porosity of the porous medium
S_j	Saturation of the phase j
k	Absolute permeability of the porous medium
k_{rj}	j-phase relative permeability
λ_j	Mobility of the phase j
μ_j	Viscosity of the phase j
f_j	Fractional flow of the phase j
p_j	Pressure in the j-phase
P_c	Capillary pressure
u	Darcy velocity (or superficial velocity)
u_j	Partial Darcy velocity of the phase j
ΔP	Pressure drop
S_{wc}, S_{gr}	Connate water and residual gas saturations
$c_{k_{rj}}$	Endpoint relative permeability of the phase j
n_w, n_g	Corey exponents
τ	Pore-size-distribution parameter
L	Core length
D	Core diameter
T_{bt}	Breakthrough time

NP-stabilized foam flow (LE models)

C_{np}	Nanoparticle concentration
$n_{max}(C_{np})$	Maximum foam texture at local equilibrium
β	Mobility parameter
b_1, b_2	Angular and linear coefficients of $n_{max}(C_{np})$
C	Dimensionless and normalized nanoparticle concentration
S	Normalized water saturation

NP-stabilized foam flow (PB models)

n	Foam texture
n_∞	Equilibrium foam texture
Φ	Foam balance source term
K_g, K_d	Bubble generation and destruction coefficients
C	Suspended nanoparticle concentration
σ	Retained nanoparticle concentration (mechanical entrapment)
$\mathcal{A}$	Adsorbed nanoparticle concentration
λ	Filtration coefficient
θ_w, θ_g	Relative permeability reduction factors (for water and gas)
α_0, α_1	Viscosity proportionality constants
d	Constant related to the fluid viscosity
C^I	Injected (suspended) nanoparticle concentration
k^0_{rw}, k^0_{rg}	Original relative permeability functions (before nanoparticle injection)

Analytical solution

S_L, S_R	Left and right water saturation values of the Riemann problem
C_L, C_R	Left and right nanoparticle values of the Riemann problem
U_M	Intermediate state
λ_C, λ_S	Eigenvalue associated with the C and S families
e_C, e_S	Eigenvector associated with the C and S families
$\mathcal{T}$	Transition curve
$\mathcal{L}, \mathcal{R}$	Sets located to the left and the right of $\mathcal{T}$
v^A_i, v^A_f	Initial and final velocities of an A-wave

Uncertainty quantification and sensitivity analysis

$\mathbb{E}$	Expected value
$\mathcal{Y}$	Quantity of interest (QoI)
$\mathbb{V}$	Variance
z_i	Uncertain input
$\mathcal{S}_i$	Main Sobol index of z_i
$\mathcal{S}_{T_i}$	Total Sobol index of z_i
μ	Mean
σ	Standard deviation
$\mathcal{U}$	Uniform distribution
$\mathcal{N}$	Normal distribution

CONTENTS

1 INTRODUCTION

The interest in modeling and solving foam flow in porous media has grown recently due to its relation to several applications. Examples of applications are soil remediation practices [1], decontamination and blocking of pollutants in aquifers and groundwater [2,3], degradation of solid waste in landfills [4], more effective fertilizer delivery in the agricultural industry [5], CO_2 storage [6], and improved oil recovery [7], which is the main application of this work. Conventional oil extraction techniques, such as water or gas injection to increase reservoir pressure, can only recover about 30% of the available oil [8]. Therefore, the upstream petroleum industry has increasingly used more advanced techniques. For Brazilian Pre-salt, the importance of technological advances in enhanced oil recovery (EOR) methods is even more evident. The challenges of its exploration include the heterogeneous nature of the carbonate reservoir, a thick salt layer, and the presence of CO_2 in the associated gas, in addition to the unique demands regarding sub-sea engineering [9]. For environmental and economic reasons, it is interesting to reinject the CO_2 produced back into the reservoir, so the technique of water-alternating-gas (WAG) injection started to be used [10]. However, the high mobility of CO_2, along with the heterogeneity and the thickness of the reservoirs, can favor phenomena that negatively affect their sweep efficiency. The main three phenomena are viscous fingering (unstable and irregular front due to the viscosity difference between the fluids), channeling (preferential paths for fluid flow through a high-permeable zone), and gravity override (accumulation of a less dense fluid in the upper layers of the porous medium) [11, 12]. A possible option to minimize these problems is the use of foam. Fig. 1 presents a scheme of the foam-assisted water-alternating-gas (FAWAG) injection, also called surfactant-alternating-gas (SAG) injection. In this technique, foam is generated in the reservoir by alternating injection of gas and a solution of water with surfactant. Foam presents higher viscosity and, consequently, lower mobility (in comparison with gas), yielding an improved sweep efficiency of the porous rock and a higher oil recovery factor [13, 14]. Fig. 2 shows a schematic comparison between gas and foam injection.

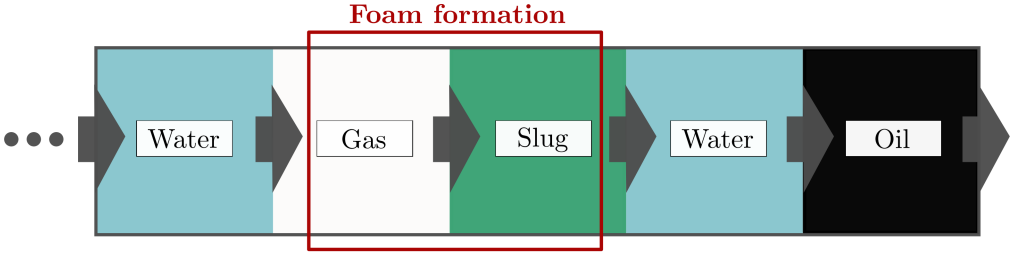

Figure 1 – Illustration of the FAWAG technique, which involves injecting water, a slug of surfactant, and gas in a cyclical process into an oil-filled reservoir.

One of the biggest challenges of using foam in EOR is maintaining long-term

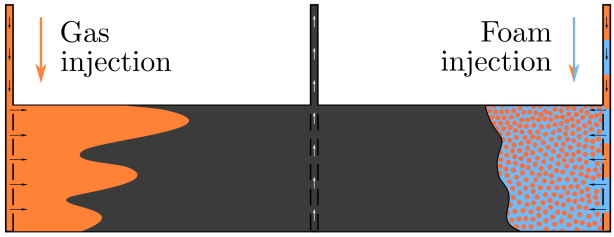

Figure 2 – Comparison between gas and foam injection. The foam formation helps prevent three phenomena that negatively affect oil production: viscous fingering, channeling, and gravity override. Source: [15].

foam stability due to high bubble surface tension. Surfactants are typically used to enhance bubble generation and resistance to coalescence, but they face limitations at reservoir conditions, where they tend to degrade faster in the presence of oil, brine, and high temperatures [16, 17]. Recently, some experimental studies [18–24] have reported that adding nanoparticles (NP) improved foam stability and resistance; see [25, 26] for a detailed review. Nanoparticles are particles with a diameter of approximately 1-100 nm, composed of a core and grafted or covalently linked surface molecules [27]. Since the properties depend on the core and the surface molecules combination, it is possible to produce nanoparticles with specific physical properties to suit the demands of different applications [27]. They can be produced from various inexpensive materials, such as fly ash, sand, limestone, and silica [25]. The foam stabilization by surfactants and nanoparticles is based on their accumulation at the gas-liquid interface and Plateau borders, which reduces the direct contact between the fluids; see Fig. 3. This slows down liquid drainage and gas diffusion, reducing the velocity of film rupture and bubble coalescence [28–30]. The main advantage of using solid particles as stabilizer agent lies in their high adhesion energy at the gas-liquid interface [18]. Unlike surfactant molecules, nanoparticles require high desorption energy to pull out from the interface, so the adsorption to the gas-liquid interface is almost irreversible [19]. In addition, the thermal and mechanical strength and rigidity properties enable them to be stable when other chemicals (including surfactants) start degrading. All these characteristics ensure long-term foam stability even under unfavorable conditions [18, 19, 31].

In general, for particles injection to be effective in subsurface applications, they must meet three key criteria [32]: (i) maintain stable dispersion in the injected water without forming aggregates; (ii) travel long distances with minimal retention; and (iii) attach themselves only at specific/desired locations. Particle retention is a concern as it can lead to reduced rock permeability and a decline in injectivity (i.e., increased pressure at a given flow rate) in injection wells [33]. In the specific case of foam flow with suspended nanoparticles, the consequences are more complex. A high retention rate reduces the number of particles available for foam stabilization, reducing foam flow efficiency [23]. The surface chemistry of nanoparticles plays a key role in influencing their filtration, adsorption,

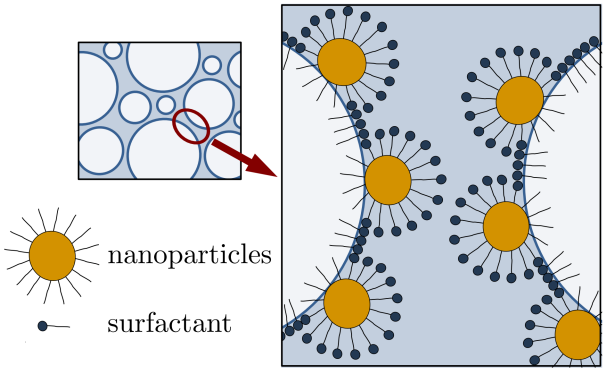

Figure 3 – Scheme of foam stabilization by an anionic surfactant and hydrophobic nanoparticles. The blockage of foam lamella and Plateau borders with nanoparticles, along with other surface phenomena, slows down liquid drainage and film rupture [28, 29].

and rheological behavior within porous media. Consequently, proper surface modifications can regulate particle characteristics, enabling improved emulsification, minimized particle retention, controlled wettability, and enhanced foam stability [34].

1.1 MATHEMATICAL MODELING AND ANALYTICAL INVESTIGATION

Foam usage for improving oil recovery was reviewed extensively [35, 36], and there are several approaches to modeling foam flow in porous media [13,14,37–39]. However, it is extremely challenging to incorporate nanoparticles. Two works [30,40] presented numerical solutions for foam models using calibrated parameters derived from experimental data of foam assisted by nanoparticles. That is, only the effect of nanoparticles is included in these models. In another study [41], the authors propose a model coupling foam and nanoparticles, which was later experimentally validated [42]. These two works investigate the remediation of contaminated sites, focusing on the foam action on nanoparticle transport. In the present study, we are interested in the action of nanoparticles on foam transport in porous media. Notice that the latter model [41,42] is too complex for analytical investigation, which is our purpose here.

In this thesis, we propose two mathematical models describing foam flow with nanoparticles (NP-stabilized foam flow) in porous media: a local equilibrium model and a population balance model. They are based on the Stochastic Bubble Population (SBP) model, proposed by [13] and validated experimentally [43,44]. In comparison to other foam models [37,38], it simplifies the number of fitting parameters while remaining robust enough to predict foam behavior in porous media [13]. The SBP model consists of a two-phase (water-gas) flow in the presence of foam. Additionally, we include a transport equation incorporating nanoparticles as a tracer in the water phase and consider the nanoparticle effect reducing foam mobility based on experimental data for silica nanoparticles [19, 30].

Our first NP-stabilized foam flow model is based on a simplified version of the SBP

model with foam in local equilibrium, which is a common hypothesis used in most commercial simulators [45]. We consider the aqueous solution of surfactant and nanoparticles to be a colloidally stable dispersion. That is, the particles are dispersed at a constant concentration without sedimentation, agglomeration, or retention over time. After the injection process, the particles migrate to the gas-liquid interface, which leads to the stabilization of the foam. This complex phenomenon is simply described by the equilibrium foam texture, proposed as a function of nanoparticle concentration. The local equilibrium model is a non-strictly hyperbolic system and, following the Conservation Laws Theory [46, 47], we prove the existence of a global solution for generic initial and injection conditions. Then, we use the obtained solution to investigate the effect of nanoparticle concentration on water production and the breakthrough time (the time it takes for the gas phase to reach the reservoir's end).

The second model considers the mechanistic SBP model, including a transport equation for suspended and retained nanoparticles based on the deep-bed filtration theory [48,49]. We also include permeability reduction due to particle retention. A semi-analytical solution under steady-state conditions is presented, which is a valid approach for describing the foam-particle flow with retention for limited times [50]. The semi-analytical solution allows for obtaining water saturation, foam apparent viscosity, and pressure drop profiles. We study different nanoparticle concentrations (in the presence and absence of salt) using retention parameters based on experimental data for silica nanoparticles.

1.2 UNCERTAINTY QUANTIFICATION AND SENSITIVITY ANALYSIS

Mathematical models are frequently calibrated using laboratory experiments. The reliability of the results depends on the accuracy of the data acquired, which is affected by inherent measurement errors and technical limitations in experiments [51]. Hence, performing uncertainty quantification (UQ) and sensitivity analysis (SA) is important to understand and quantify how these uncertainties in the input data impact the model's predictions [51, 52]; see Fig. 4. Since precise UQ and SA studies require a high number of calls to the model, the process can be very costly depending on the model's complexity [52]. In [53,54], the authors used analytical solutions combined with polynomial chaos expansion to overcome this problem. In [54], sensitivity indices were validated using results derived from the classical Monte Carlo (MC) framework. This is possible only because a benchmark analytical solution is available [54]. However, the MC simulations did not converge, highlighting the challenge of achieving convergence for this method.

Previous works explored UQ and SA studies in the context of modeling foam flow in porous media [56–60]. For instance, in [58], the authors investigated the performance of two foam models (CMG-STARS and the linear kinetic model) in capturing experimental data. Additionally, different objective functions were studied in [61], focusing on parameter

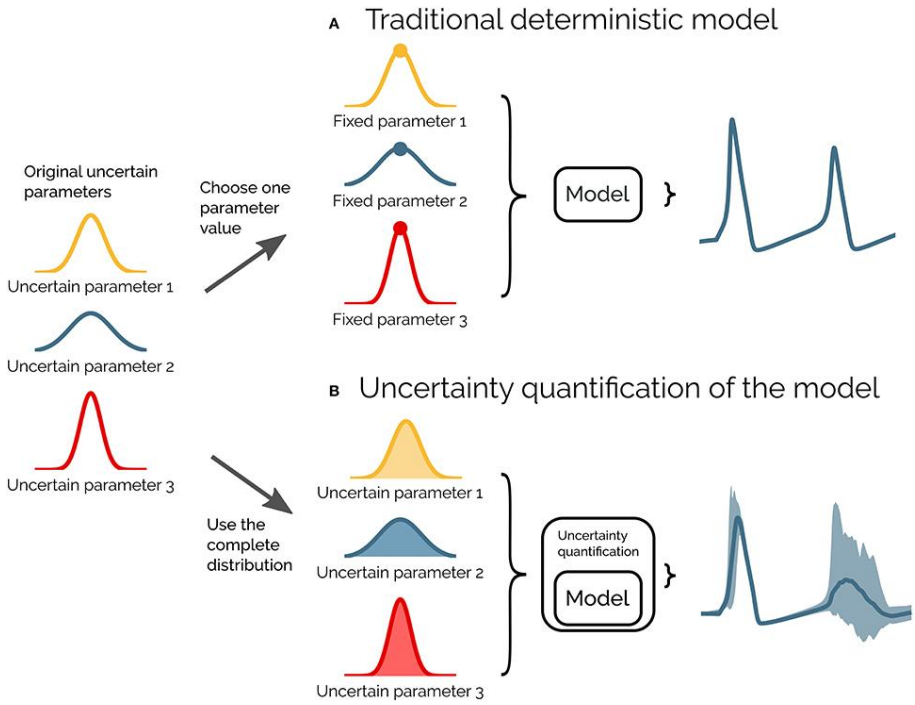

Figure 4 – In a traditional deterministic model, a fixed value is chosen for each input parameter, and the model produces a single output (gray line). However, when performing uncertainty quantification, the distributions of input parameters are considered, resulting in a range of possible output values for the model (shaded region). Source: [55].

estimation and uncertainties propagation through foam flow models. In [60], on the other hand, the authors utilized the measured variations from laboratory experiments as a weighting factor for the objective function. A recent study [62] evaluates parameter identifiability in foam flow models, showing that it is not feasible to calibrate relative permeability and foam parameters when only foam quality scan data is accessible. In [63], the authors conduct an uncertainty quantification and sensitivity analysis of a foam implicit-texture model to further understand the interactions between relative permeability and foam parameters.

In this thesis, we perform UQ and SA studies considering an NP-stabilized foam flow model in local equilibrium with quadratic relative permeability functions. The solution remains qualitatively the same as the more realistic (non-quadratic) model [64]. This simplification allows algebraic expressions to determine the solution type and construct the solution profiles, speeding up the calculations significantly. The forward propagation of uncertainties follows the MC method, and we use Sobol indices [65] as a sensitivity measure. We achieve fast convergence by using analytical solutions constructed with algebraic expressions.

1.3 THESIS ORGANIZATION

This work is structured as follows. Chapter 2 presents the theoretical foundation that will be used throughout this work. Chapter 3 proposes a local equilibrium model for NP-stabilized foam flow, neglecting particle retention. A global solution to this model is presented, enabling an analysis of the impact of nanoparticle concentration on foam flow. Chapter 4 presents a simplified model with quadratic relative permeability functions, simplifying the analytical solution. We perform an uncertainty quantification and sensitivity analysis. Chapter 5 proposes a population balance model for NP-stabilized foam flow that incorporates particle retention and permeability reduction. A semi-analytical solution is derived under steady-state conditions, enabling the investigation of retention effects on foam flow efficiency and pressure drop. We highlight that Chapters 3, 4, and 5 present the results of articles [64], [66], and [67], respectively. Finally, Chapter 6 presents conclusions and contributions.

2 THEORETICAL FOUNDATION

In this chapter, we introduce some concepts and notation that will be used throughout the work. Section 2.1 presents fundamental principles of the Conservation Laws Theory. Section 2.2 briefly describes the fractional flow theory in porous media, which will be used to review some foam flow models in Section 2.3. In Section 2.4, we provide a literature review about nanoparticle transport and retention in porous media. In Sections 2.5 and 2.6, we introduce the methods used for the uncertainty quantification and sensitivity analysis.

2.1 CONSERVATION LAWS

A conservation law is a partial differential equation (PDE) describing the behavior of a conserved quantity; that is, a variable that remains constant over time [46]. In this thesis, we study models that involve the conservation of mass. Let us consider the following system for $U = U(x,t)$, with $U : \Omega \times \mathbb{R}^+ \to \mathbb{R}^m$:

$$\frac{\partial}{\partial t}U(x,t) + \nabla \cdot F(U) = 0, \tag{2.1}$$

where $F : \mathbb{R}^m \to \mathbb{R}^m$ is called the *flux function*. For a given subdomain $\omega \subseteq \Omega$, we can rewrite this system in the integral form as [68]

$$\frac{\partial}{\partial t}\left(\int_\omega U(x,t)\, d\omega\right) + \int_{\partial\omega} F(U) \cdot \vec{n}(x)\, dx = 0, \tag{2.2}$$

where $\vec{n}(x)$ is the outward-pointing unit normal vector to $\partial\omega$ at point x on the boundary $\partial\omega$. Eq. (2.2) represents the balance between the quantity U and its flux at the boundary. The system (2.1) also can be rewritten in the quasilinear form

$$\partial_t U + A(U)\partial_x U = 0, \tag{2.3}$$

where $A(U)$ is the Jacobian matrix. We denote the p-th eigenvalue related to A as $\lambda_p(U)$, with $\lambda_1(U) \leq \lambda_2(U) \leq ... \leq \lambda_m(U)$. The corresponding eigenvector is $e_p(U)$. If matrix A is diagonalizable with real eigenvalues, the system is said to be *hyperbolic*. In particular, if all eigenvalues are distinct for all $U = U(x,t)$, then the system is *strictly hyperbolic*.

To solve a system of conservation laws, we associate it with an initial condition in the spatial domain and, sometimes, boundary conditions. In this work, we focus on pure initial value problems (IVP) with m one-dimensional equations ($\Omega \subseteq \mathbb{R}$):

$$\partial_t U + \partial_x(F(U)) = 0, \quad x \in \mathbb{R}, \quad t \in \mathbb{R}^+, \tag{2.4}$$

$$U(x,0) = U_0(x), \quad -\infty < x < \infty, \tag{2.5}$$

known as the *Cauchy problem*. A *classical solution* to this problem is a function $U : \mathbb{R} \times \mathbb{R}^+ \to \mathbb{R}^m$ continuous with continuous first partial derivatives ($\mathcal{C}^1$ class), satisfying the IVP (2.4)-(2.5) for all $(x,t) \in \mathbb{R} \times \mathbb{R}^+$.

Let us consider a particular Cauchy problem composed of Eqs. (2.4)-(2.5) with a piecewise constant initial condition and a single discontinuity as follows

$$U_0(x) = \begin{cases} U_L, & \text{if} \quad x < 0, \\ U_R, & \text{if} \quad x \geq 0. \end{cases} \tag{2.6}$$

This is called the *Riemann problem*, and U_L and U_R denote left and right states, respectively. A solution to the Riemann problem is invariant under a uniform scale transformation. That is, a change of coordinates $(x, t) \to (\kappa x, \kappa t)$, for a constant $\kappa > 0$, does not change the system or the initial conditions. Therefore, its solution only depends on the ratio x/t, being comprised of a superposition of independently propagated fundamental waves [46].

Discontinuous solutions do not satisfy Eq. (2.4) in the classical sense at all points, as derivatives are not defined at discontinuities. The integral form (defined as in Eq. (2.2)) remains valid, but it is more complex to work with. Therefore, we use a more convenient approach called the *weak form* of the PDE. In this method, the PDE is multiplied by a smooth test function $\phi : \mathbb{R} \times \mathbb{R}^+ \to \mathbb{R}^m$, which must be continuously differentiable with compact support ($\phi \in \mathcal{D}(\mathbb{R} \times \mathbb{R}^+)$); see [47] for details. Then, we use integration by parts to change the derivatives to ϕ as follows

$$\int_{-\infty}^{\infty} \int_{0}^{\infty} \left(U \frac{\partial \phi}{\partial t} + F(U) \frac{\partial \phi}{\partial x} \right) dt dx + \int_{-\infty}^{\infty} U_0(x) \phi(x, 0)\, dx = 0. \tag{2.7}$$

We say that a function $U(x, t)$ is a *weak solution* for system (2.4)-(2.5) if for all test functions $\phi \in \mathcal{D}(\mathbb{R} \times \mathbb{R}^+)$ holds (2.7). Note that every classical solution is a weak solution, but the converse is not always true.

In the following subsections, we first investigate scalar conservation laws to better understand the construction of solutions. Then, we extend the results to a system of m one-dimensional equations.

2.1.1 Scalar problems

Consider a scalar one-dimensional IVP defined by Eqs. (2.4)-(2.5), with $U : \mathbb{R} \times \mathbb{R}^+ \to \mathbb{R}$ and $F : \mathbb{R} \to \mathbb{R}$. For a classical solution $U \in \mathcal{C}^1$ of this system and $F \in \mathcal{C}^n$ ($n \geq 2$), we define the *characteristic curves* $t \mapsto (x(t), t)$ in the x-t plane as follows

$$\frac{d}{dt}(x(t)) = F'(U(x(t), t)). \tag{2.8}$$

Note that, by differentiating $U(x, t)$ along one of these curves, we obtain

$$\frac{d}{dt}(U(x(t), t)) = \frac{dx}{dt} \frac{\partial}{\partial x} U(x, t) + \frac{\partial}{\partial t} U(x, t) = \left(\frac{\partial U}{\partial t} + F'(U) \frac{\partial U}{\partial x} \right)(x, t) = 0. \tag{2.9}$$

Therefore, U is constant along the characteristics. As a result, the characteristics are straight lines on the x-t plane given by

$$x(t) = x_0 + t F'(U_0(x_0)), \tag{2.10}$$

where $x_0 = x(0)$ is the initial data (at $t = 0$) of the curve and $F'(U_0(x_0))$ is its slope. A schematic representation is presented in Fig. 5.

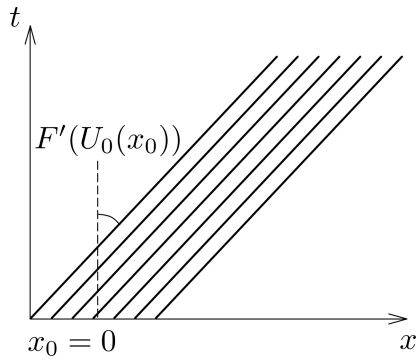

Figure 5 – Characteristics on the x-t plane.

We are interested in a particular type of weak solution to system (2.4)-(2.5) that is class $\mathcal{C}^1$ by parts. That is, there are a finite number of curves $\Gamma_1, ..., \Gamma_p$ defined by $x = \xi_i(t)$, where $\xi_i \in \mathcal{C}^1$ $(i = 1, ..., p)$. In this case, U is a weak solution if U is a classic solution in all the domain where it is $\mathcal{C}^1$ and U satisfies the following condition along the discontinuity curve Γ:

$$F(U^+) - F(U^-) = \xi'(t)(U^+ - U^-), \tag{2.11}$$

where U^- and U^+ are the states on the left and right of the discontinuity. This equation is known as the Rankine-Hugoniot condition and governs the behavior of *shock* and *contact* waves. For scalar problems, the shock propagation velocity $\sigma = \xi'(t)$ is given by

$$\sigma = \frac{F(U^+) - F(U^-)}{U^+ - U^-}. \tag{2.12}$$

The left panel in Fig. 6 shows a schematic representation of a shock wave on the x-t plane. Note that shock formation occurs when the characteristics first intersect. The discontinuous solution is a contact when the characteristics are parallel on both sides of the discontinuity; see the right panel in Fig. 6. In this case, the propagation velocity of the contact wave is equal to the characteristics slope $F'(U^-) = F'(U^+)$.

Hyperbolic systems of conservation laws usually possess more than one solution, leading to the development of various criteria based on mathematical and physical principles to identify a single admissible weak solution [69]. In continuum physics, admissibility criteria naturally arise from the Second Law of thermodynamics, which fundamentally represents a statement of stability. These criteria may be directly defined through entropy inequalities or indirectly introduced by incorporating vanishing diffusion into the system; see [47, 69] for details.

For system (2.4)-(2.5), a discontinuity with velocity propagation σ (2.12) must satisfy the entropy condition [46]

$$F'(U^-) > \sigma > F'(U^+). \tag{2.13}$$

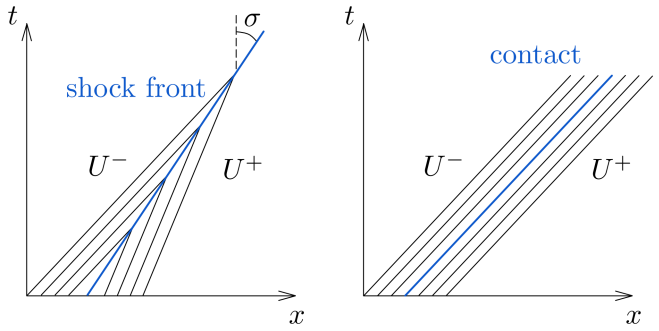

Figure 6 – Schematic representation of a shock (left panel) and a contact (right panel) on the x-t plane. The central blue lines represent the change between left (U^-) and right (U^+) states of each discontinuity.

We highlight that if F is convex ($F'' > 0$), σ must lie between $F'(U^-)$ and $F'(U^+)$, which are the characteristics slope for the shock left and right states; see Fig. 5 and 6. Thus, Eq. (2.13) reduces to $F'(U^-) > F'(U^+)$, yielding (by convexity) $U^- > U^+$. The Oleinik entropy condition [70] is a more general criterion that can be applied also to nonconvex scalar functions. It states that an entropic shock must satisfy

$$\frac{F(U) - F(U^-)}{U - U^-} \geq \sigma \geq \frac{F(U) - F(U^+)}{U - U^+}, \tag{2.14}$$

for all U between U^- and U^+. Geometrically, if $U^+ > U^-$, the line connecting $(U^+, F(U^+))$ to $(U^-, F(U^-))$ must be below the graph of F. Otherwise, if $U^- > U^+$, the line connecting $(U^-, F(U^-))$ to $(U^+, F(U^+))$ must be above the graph of F.

Even if the initial condition is discontinuous, it is possible for the conservation law to have a continuous solution (called *rarefaction wave*). This solution immediately smooths out the initial discontinuities and takes the form $U = U(x/t)$, being constant along any line x/t. In the x-t plane, the region where rarefaction occurs does not have any characteristics. The rarefaction is represented as straight lines starting from the origin with slopes varying from $F'(U^-)$ to $F'(U^+)$ [46], as shown in Fig. 7.

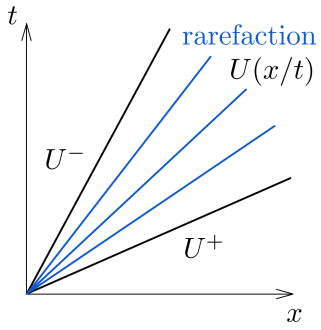

Figure 7 – Schematic representation of a rarefaction on the x-t plane.

Let us consider the scalar Riemann problem

$$\partial_t U + \partial_x(F(U)) = 0, \tag{2.15}$$

$$U_0(x) = \begin{cases} U_L, & \text{if} \quad x < 0, \\ U_R, & \text{if} \quad x \geq 0. \end{cases}, \tag{2.16}$$

For a convex function, the solution is always either a shock or a rarefaction, depending on the left and right states; see the entropy condition (2.13). If $U_L < U_R$, the solution is a rarefaction and takes the form [46]

$$U(x,t) = \begin{cases} U_L, & \text{if} \quad x \leq F'(U_L)t, \\ V(x/t), & \text{if} \quad F'(U_L)t < x < F'(U_R)t, \\ U_R, & \text{if} \quad x \geq F'(U_R)t, \end{cases} \tag{2.17}$$

where $V = (F')^{-1}(x/t)$. Otherwise, if $U_L > U_R$, the solution is a shock given by

$$U(x,t) = \begin{cases} U_L, & \text{if} \quad x \leq \sigma t, \\ U_R, & \text{if} \quad x \geq \sigma t, \end{cases} \tag{2.18}$$

where σ is the propagation velocity of the shock obtained by the Rankine-Hugoniot condition:

$$\sigma = \frac{F(U_R) - F(U_L)}{U_R - U_L}. \tag{2.19}$$

Analogous, for a concave function ($F'' < 0$), the solution is a shock wave if $U_L < U_R$ and a rarefaction wave if $U_L > U_R$.

Now, we will apply this theory to the Buckley-Leverett equations [71], which provide a simple model for two-phase flow in a porous medium. These equations can be used to study oil recovery applications, where water is injected to displace oil from a reservoir to a production well. We can describe a one-dimensional system of oil-water flow by Eqs. (2.15)-(2.16), where U represents the water saturation ($U \in [0,1]$) and F is the water fractional flow function. Usually, we assume that the Buckley–Leverett function is S-shaped, such as the following example

$$F(U) = \frac{U^2}{U^2 + \kappa(1-U)^2}, \tag{2.20}$$

where κ is a constant. We investigate the scenario of pure water injection ($U_L = 1$) into pure oil ($U_R = 0$).

Note that function (2.20) is neither convex nor concave, as it possesses an inflection point U^I, where $F''(U) = 0$. Thus, the entropy solution is a combination of shock and rarefaction waves. Following the Welge's method [72], to solve the Buckley-Leverett problem we use the the "convex-hull" U^*, which is obtained by

$$F(U^*) - F(U_R) = F'(U^*)(U^* - U_R). \tag{2.21}$$

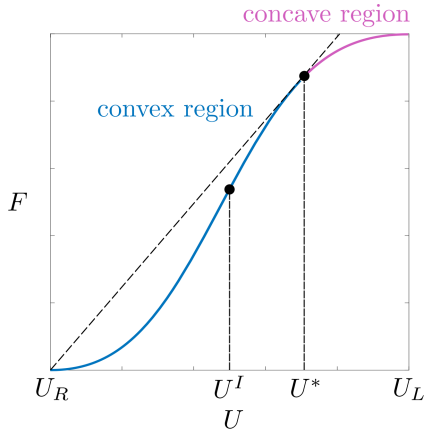

Figure 8 – Construction of the intermediate state to the Buckley-Leverett problem (U^*). The inflection point (U^I) is also indicated, where $F''(U) = 0$.

Figure 8 shows the construction of this intermediate state U^*, which divides f into convex and concave parts.

Since F is concave in the interval $[U^*, U_L]$ and $U_L > U^*$ (here, U^* is the wave's right state), the wave connecting U_L to U^* is a rarefaction. Conversely, F is convex in the interval $[U_R, U^*]$ and $U^* > U_R$ (here, U^* is the wave's left state), so the solution connecting U^* to U_R is a shock. Then, the complete solution is given by

$$U(x,t) = \begin{cases} U_L, & \text{if} \quad x \leq F'(U_L)t, \\ (F')^{-1}(x/t), & \text{if} \quad F'(U_L)t < x < F'(U^*)t, \\ U^*, & \text{if} \quad F'(U^*)t < x < \sigma t, \\ U_R, & \text{if} \quad x \geq \sigma t, \end{cases} \tag{2.22}$$

where $\sigma = ([F(U^*) - F(U_R)])/(U^* - U_R)$. Fig. 9 shows a scheme of this solution following the Wash-Lake diagram [73].

2.1.2 Systems of nonlinear conservation laws

Now, we will study nonlinear systems of conservation laws. In this case, the eigenvalues and eigenvectors are also functions of U. We are looking for weak solutions to the Riemann problem (2.4)-(2.6) as a sequence of shocks, rarefactions, and contacts. Firstly, we need to introduce some definitions.

Given a general conservation law (2.3), the p-th characteristic field (known as p-th family) is said to be *genuinely nonlinear* if

$$\nabla\lambda_p(U) \cdot e_p(U) \neq 0, \quad \forall U \in \mathbb{R}^m, \tag{2.23}$$

where $\nabla\lambda_p(U) = (\partial\lambda_p/\partial U_1, ..., \partial\lambda_p/\partial U_m))$ is the gradient of $\lambda_p(U)$. If there is some $U \in \mathbb{R}^m$ such that $\nabla\lambda_p(U) \cdot e_p(U) = 0$, we say that the p-th family possesses a *local linear degeneracy*. This family is said to be *linearly degenerate* if

$$\nabla\lambda_p(U) \cdot e_p(U) \equiv 0, \quad \forall U \in \mathbb{R}^m. \tag{2.24}$$

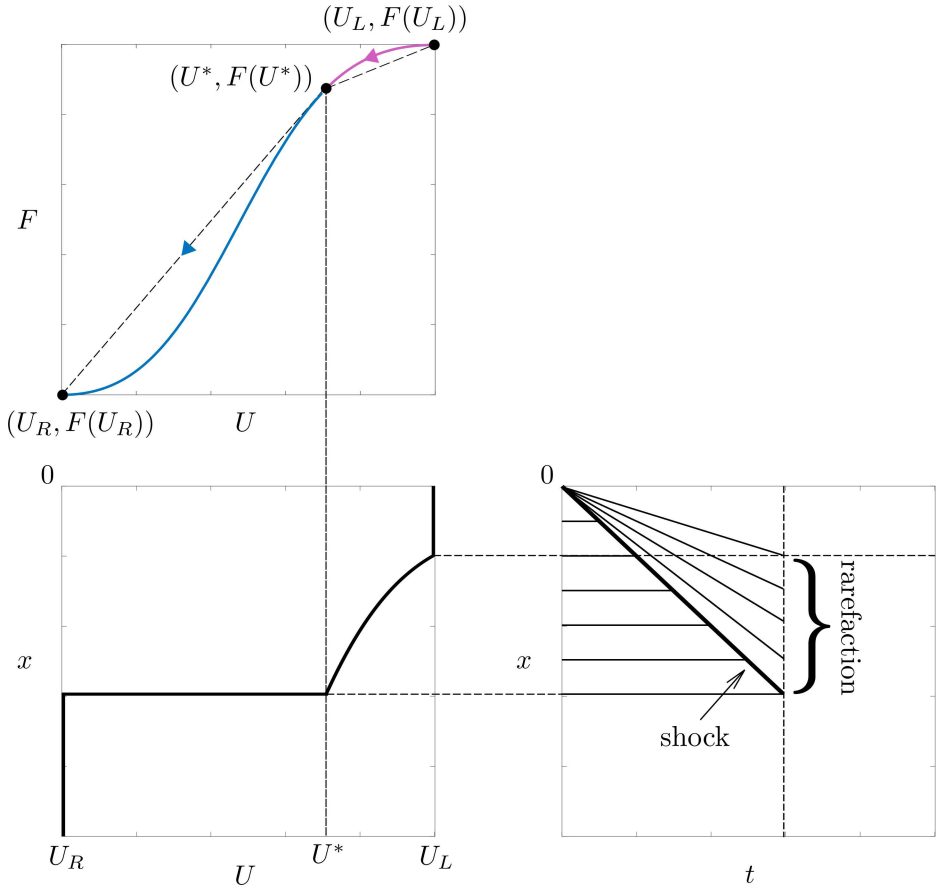

Figure 9 – Solution to the Buckley-Leverett problem. The upper panel shows the solution construction using the flux function. The lower panels show a scheme of the solution profile at a given time and the corresponding characteristic curves.

Genuinely nonlinear families are associated with shock and rarefaction waves, while a discontinuity in a linearly degenerate field is a contact wave [46].

The integral curve associated with the eigenvector field $e_p(U)$ possesses the property that the tangent vector to the curve at any point is in the direction of $e_p(U)$. That is, if U_p is a parameterization for $\xi \in \mathbb{R}$ of an integral curve in the p-th family, we obtain

$$U_p'(\xi) = \kappa(\xi) e_p(U_p(\xi)), \quad \forall \xi \in \mathbb{R}, \tag{2.25}$$

where $\kappa(\xi)$ is a scalar factor; see [46] for details. Continuous solutions lie along integral curves. Hence, considering a p-th family genuinely nonlinear, a left state U^- can be connected to a right state U^+ by a rarefaction wave if both states lie on the same integral curve and $\lambda_p(U(\xi))$ is monotonically increasing along this curve between U^- and U^+ [46].

Shocks are discontinuous solutions characterized by assuming constant values to the left (U^-) and to the right (U^+) of the discontinuity. As in the scalar case, the shock velocity must satisfy the Rankine-Hugoniot Condition (defined as in Eq. (2.11)). Let us consider $U^+ \in \mathbb{R}^m$ fixed and σ, U^- as variables. We are looking for all points $U \in \mathbb{R}^m$ that can be connected to U^+ by a discontinuity satisfying (2.11) for some velocity propagation

σ. Thus, we obtain a system of m equations in $m+1$ unknowns

$$F(U^+) - F(U) - \sigma(U^+ - U) = 0, \tag{2.26}$$

which defines m curves (called *Hugoniot curves*) through the point U^+, one for each characteristic family; see [46] for details. The set of points $U \in \mathbb{R}^m$ in these curves is known as *Hugoniot locus* of U^+, being represented by $\mathcal{H}(U^+, \sigma, U)$. Analogously, we can fixed U^- and consider σ, U^+ as variables, yielding

$$\mathcal{H}(U^-, \sigma, U) \equiv F(U) - F(U^-) - \sigma(U - U^-) = 0. \tag{2.27}$$

We say that U^+ and U^- can be connected by a shock wave if both states lie on the same Hugoniot curve and there is $\sigma \in \mathbb{R}$ such that $\mathcal{H}(U^-, \sigma, U^+) = 0$.

For a p-th field linearly degenerate, the eigenvalue $\lambda_p(U)$ is constant on the integral curves of $e_p(U)$ $\forall U \in \mathbb{R}^m$, so the eigenvector is also constant on these curves. Therefore, the integral curves are straight lines in phase space and form the Hugoniot locus for contact discontinuities [46]. That is, if a left state U^- is connected to a right state U^+ by a contact in the p-th family, these states lie on the same integral curve of $e_p(U)$, and the discontinuity propagates at a velocity $\lambda_p(U^-) = \lambda_p(U^+)$.

For a given $\hat{U}$, all points $U \in \mathcal{H}(\hat{U}, \sigma, U)$ can be connected to $\hat{U}$ by a discontinuity, but to finding the entropic solution we must verify an additional criterion. The Lax entropy condition [74] is a generalization of (2.13) (scalar case) to systems of equations. It establishes that, for a genuinely nonlinear p-th field, a discontinuity in this field connecting U^- to U^+ is admissible only if

$$\lambda_p(U^-) > \sigma > \lambda_p(U^+), \tag{2.28}$$

$$\lambda_{p-1}(U^-) < \sigma < \lambda_{p+1}(U^+). \tag{2.29}$$

To linearly degenerate fields, the Lax entropy condition to admissible contact waves is modified, allowing the equality in Eqs. (2.28)-(2.29).

Constructing the complete solution to the Riemann problem associated with a system of m nonlinear conservation laws is very challenging. If $U \in \mathbb{R}^2$, as the systems investigated in this work, the solution procedure is significantly simplified [46, 47].

2.2 FRACTIONAL FLOW THEORY

The fractional flow theory investigates the multi-phase flow dynamics in porous media. Although the foam flow involves more complex phenomena, this theory can still be useful in describing it [75].

2.2.1 Basic definitions

A *porous medium* refers to a spatial domain with interconnected voids (pores) occupied by one or more fluids [76]; see Fig. 10. The ratio between the total pore space ($\overline{V_p}$) and the total volume (V) is called absolute porosity. However, we use *porosity* (φ) in the sense of relative porosity, which considers only the volume of interconnected pores (V_p):

$$\varphi = \frac{V_p}{V}. \tag{2.30}$$

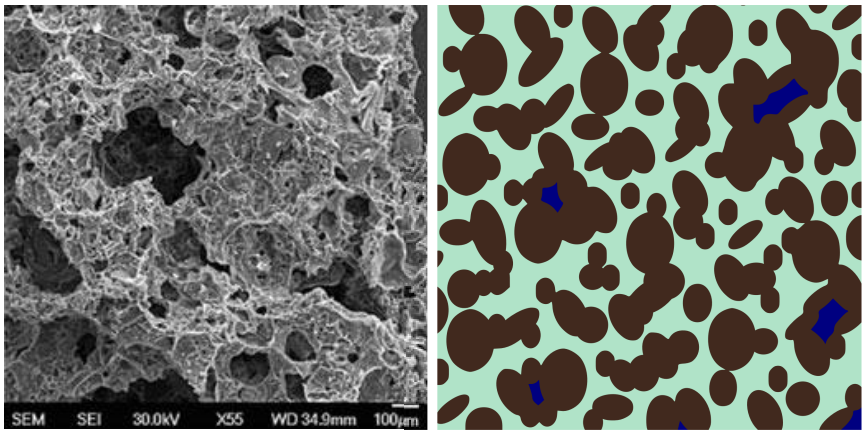

Figure 10 – The left panel shows a microscopic image of a ceramic (an example of a porous medium). Source: [76]. The right panel illustrates a porous medium in the two-dimensional space, where the solid matrix is represented in brown. Note that there are interconnected pores (light blue region) and isolated porous (blue regions).

The *saturation* of a phase j is the ratio between the total volume occupied by this phase (V_j) and the total pore space:

$$S_j = \frac{V_j}{V_p}. \tag{2.31}$$

The hypothesis of a saturated porous medium assumes that the pores are filled with the model's included phases, i.e., $\sum_j S_j = 1$. We define the *residual saturation* (S_{jr}) as the amount of the j-phase that remains irreducible in the medium.

Permeability (k) measures the medium's ability to allow fluid flow based on pore geometry. Multiple fluids in a pore space lead to lower permeability for each phase compared to single-phase flow due to partial occupancy and potential interaction with other phases. The concept used to describe this situation is called relative permeability and is defined as

$$k_{rj} = \frac{k_j}{k}, \tag{2.32}$$

where k_j represents the flow capacity of the j-phase in the presence of other phases, called *effective permeability*. Various mathematical models have been proposed to estimate relative permeabilities as functions of phase saturation [77–81].

The *mobility* of a phase j is written as

$$\lambda_j = \frac{k_j}{\mu_j}, \tag{2.33}$$

where μ_j is the *viscosity* and refers to the fluid's resistance to flow (regardless of the medium). Other correlated definitions are *total mobility* (λ_T) and *relative mobility* (λ_{rj}):

$$\lambda_T = \sum_j \lambda_j, \quad \lambda_{rj} = \frac{k_{rj}}{\mu_j}. \tag{2.34}$$

Using this definition, the *fractional flow* of a phase j (f_j) is the volumetric fraction of its displacement in a specific direction, being calculated by the ratio of the j-phase mobility and the total mobility [71]:

$$f_j = \frac{\lambda_j}{\lambda_T}. \tag{2.35}$$

Note that, for a saturated medium, $\sum_j f_j = 1$.

2.2.2 Darcy's law

Darcy's law is a mathematical equation describing the hydrodynamic behavior of a fluid flow through a porous medium. It was initially inferred by Henry Darcy [82] based on the outcomes of his experiments on the flow of water through sand beds. The formula is used to predict the velocity of a fluid in a porous medium, taking into account the pressure gradient (∇p), fluid viscosity, and the medium's permeability. Considering a homogeneous medium and neglecting gravitational effects, the *Darcy velocity* (or superficial velocity) is given by [83]

$$u = -\frac{k}{\mu}\nabla p. \tag{2.36}$$

This definition refers to the effective fluid flow velocity (on a macroscopic scale). The velocity at which the fluid travels through the pores, known as *interstitial velocity*, is inversely proportional to porosity as $v = u/\varphi$.

Although Darcy's law was originally proposed for a single-phase flow, its extension to multi-phase flows, proposed by [84], is widely utilized. For each phase j, we define the partial Darcy velocity as [83]

$$u_j = -k\lambda_{rj}\nabla p_j, \tag{2.37}$$

where ∇p_j is the partial pressure gradient. In this case, the partial interstitial velocity (v_j) is related to the volumetric fraction in the porous medium occupied by phase j:

$$v_j = \frac{u_j}{\varphi S_j}. \tag{2.38}$$

We highlight that the superficial velocity is the sum of all partial velocities, i.e., $\sum_j u_j = u$.

2.2.3 Relative permeability models

Making direct experimental measurements of relative permeability is quite challenging, so many methods have been proposed to estimate permeability curves using experimental *capillary pressure* data [85]. In the context of porous media, capillary pressure is the pressure differential between two immiscible fluids in contact (a wetting and non-wetting phase) caused by the interfacial tension between them. In this section, we consider two-phase flow, with the index $j = w, nw$ representing the wetting and non-wetting phases, respectively. Thus, the capillary pressure (P_c) is given by

$$P_c = p_{nw} - p_w, \tag{2.39}$$

where p_j is the pressure in the j-phase.

In [85], the authors use classical works of Purcell [86] and Burdine [87] to derive equations for calculating the relative permeabilities using the capillary pressure. From [86], the relative permeability of the wetting (k_{rw}) and non-wetting (k_{rg}) phases are

$$k_{rw} = \frac{\int_0^{S_w} dS_w/(P_c)^2}{\int_0^1 dS_w/(P_c)^2}, \quad k_{rnw} = \frac{\int_{S_w}^1 dS_w/(P_c)^2}{\int_0^1 dS_w/(P_c)^2}. \tag{2.40}$$

From [87], where a tortuosity factor (T_{rj}) is included, we obtain [85]

$$k_{rw} = (T_{rw})^2 \frac{\int_0^{S_w} dS_w/(P_c)^2}{\int_0^1 dS_w/(P_c)^2}, \quad k_{rnw} = (T_{rnw})^2 \frac{\int_{S_w}^1 dS_w/(P_c)^2}{\int_0^1 dS_w/(P_c)^2}. \tag{2.41}$$

The tortuosity ratio of the wetting and non-wetting phases is given by

$$T_{rw} = \frac{S_w - S_m}{1 - S_m}, \quad T_{rnw} = \frac{S_w - S_m - S_e}{1 - S_m - S_e}, \tag{2.42}$$

where S_m represents the minimum saturation of the wetting phase from the capillary pressure curve, while S_e represents the equilibrium saturation of the non-wetting phase.

These two models (Eqs. (2.40) and (2.41)) show that determining an analytical expression for relative permeability relies on representing capillary pressure as a simple mathematical function. Considering an oil-gas flow (in this case, oil is the wetting phase and gas is the non-wetting phase), Corey [77] found that the capillary pressure curves could be approximated by:

$$\frac{1}{P_c^2} = c^* S, \tag{2.43}$$

where c^* is a constant and S is the normalized wetting phase saturation. Since this relation was originally proposed for the drainage case (the wetting phase is displaced by the non-wetting phase), $S = (S_w - S_{wr})/(1 - S_{wr})$. However, it can be extended by the imbibition case (the wetting phase is the displacing fluid) defining

$$S = \frac{S_w - S_{wr}}{1 - S_{wr} - S_{nwr}}, \tag{2.44}$$

where S_{wr} and S_{nwr} are the residual saturation of wetting and non-wetting phases. After substituting Eq. (2.43) into Eq.(2.41) and assuming $S_e = 0$ and $S_m = S_{wr}$, the relative permeabilities can be calculated as [77]:

$$k_{rw} = S^4, \quad k_{rnw} = (1 - S)^2(1 - S^2). \tag{2.45}$$

The original Corey model was generalized by Brooks and Corey [78] by proposing another function to describe the capillary pressure:

$$P_c = p_e S^{1-\tau}, \tag{2.46}$$

where p_e is the entry pressure and τ is a parameter related to the pore size distribution. Then, Eq. (2.45) is rewritten as

$$k_{rw} = S^{\frac{2+3\tau}{\tau}}, \quad k_{rnw} = (1 - S)^2(1 - S^{\frac{2+\tau}{\tau}}). \tag{2.47}$$

From now on, we will refer to relative permeability models in the form

$$k_{rw} = c_{k_{rw}} S^{n_w}, \quad k_{rnw} = c_{k_{rnw}} S^{n_{nw}}, \tag{2.48}$$

as Corey type (or simply Corey). Here, $c_{k_{rw}}$ and $c_{k_{rnw}}$ are the endpoints relative permeability of wetting and non-wetting phases. These values, along with the model's exponents n_w, n_{nw}, are obtained experimentally.

2.2.4 Two-phase flow with a tracer

In flow dynamics, a tracer refers to a substance that is present in small quantities in a solvent fluid and is carried along with it [68]. Tracers can be categorized as passive if they do not affect the fluid properties or active if they do. Here, we are interested in active tracers that can be used to optimize a two-phase flow in porous media by changing the mobility of fluids. To model NP-stabilized foam flow with nanoparticles as tracers in the aqueous phase, we were inspired by various mathematical models found in the literature with other applications [88–91]. Below, we briefly present some of them, focusing on how the tracer is included in each model.

Polymers are traditionally used to modify the mobility of injected water in EOR applications. Isaacson [88] and Johansen and Winther [89] presented water-oil flow models where there is one equation describing the tracer (polymer) transport in the wetting (water) phase. The polymer acts on the same phase where it is diluted, increasing the water viscosity. Surfactants are also frequently used to optimize oil flow during alternating injections of water and gas. In this case, the tracer is used to modify the gas mobility by generating bubbles. Thorat and Bruining [90] and Fritis et al. [91] proposed water-gas flow models where there is one equation describing the tracer (surfactant) transport in the

wetting (water) phase. However, although the surfactant is a tracer in the aqueous phase, it affects the non-wetting (gas) phase mobility, where the foam formation occurs.

As will be detailed in the next section, there are different approaches to model foam flow. Several works do not consider the surfactant concentration as a variable, using the foam texture instead. In such cases, the foam itself can be considered as a tracer. Simjoo and Zitha [43] and Zavala et al. [92] presented water-gas flow models where there is one equation describing the tracer (foam) balance in the non-wetting (gas) phase. This implies that the tracer acts and is diluted in the gaseous phase. About NP-stabilized foam models, Li and Prigiobbe [41] proposed a model for water-gas flow with two tracers: foam (in the same sense as [92]) and nanoparticles. Nanoparticles are diluted in both phases, and the exchange rate between them is considered, while the foam is present in the non-wetting (gas) phase. The main aim of this study was to evaluate the influence of foam in the nanoparticle transport. Therefore, nanoparticles were considered a passive tracer and did not influence the flow characteristics.

In this thesis, we present a local equilibrium model and a population balance model describing NP-stabilized foam flow. We consider nanoparticles diluted in the wetting (water) phase, with a transport equation inspired by [88, 89]. For the first model, proposed in [64, 66], foam acts on the non-wetting (gas) phase by reducing the gaseous phase relative permeability (depending on the foam texture [13, 92]). In this case, foam texture is not a variable since we adopt the equilibrium hypothesis. Therefore, nanoparticle is the only tracer and acts indirectly on the gaseous phase through the influence of nanoparticle concentration in the equilibrium foam texture. The second model (population balance), proposed in [67], considers the foam texture as a variable, so both nanoparticles and foam are tracers. Foam and nanoparticles act by reducing the gaseous phase mobility through the foam's apparent viscosity, which depends on nanoparticle concentration.

A summary of these different approaches to include tracers in two-phase flow is presented in Tab. 1.

2.3 FOAM FLOW MODELS

Foam models can be classified as empiric and mechanistic, according to the foam-related variable [11]. Empiric models consider the foam's action implicitly through a change in the gas's mobility, with the foam always in local equilibrium. According to [14], models with foam in local equilibrium can describe their displacement adequately. These models are less complex and more numerically stable, being used in most commercial simulators [45]. Mechanistic models consider foam texture as an independent variable with a separate equation to describe it. The general form, physically more accurate, is called the population balance model. In this model, foam texture is obtained explicitly by solving a partial differential equation, and gas mobility is written as a function of foam texture [57].

Table 1 – Summary of the action of tracers on two-phase flow in previous studies.

References	Tracer		
	Type	Diluted in	Acts on
Isaacson [88], Johansen and Winther [89]	Polymer	w-phase	The w-phase mobility
Simjoo and Zitha [43], Zavala et al. [92]	Foam	nw-phase	The nw-phase mobility
Thorat and Bruining [90], Fritis et al. [91]	Surfactant	w-phase	The nw-phase mobility
Li and Priogiobbe [41]	Nanoparticle	Both phases	Do not influence the flow characteristics
	Foam	nw-phase	The nw-phase mobility
Danelon et al. [64, 66]	Nanoparticle	w-phase	The nw-phase mobility
Danelon et al. [67]	Nanoparticle	w-phase	The nw-phase mobility
	Foam	nw-phase	The nw-phase mobility

Due to the complexity of this approach, especially regarding bubble generation and coalescence rates, some researchers proposed local equilibrium or semi-empirical methods to calculate foam texture from algebraic equations [11].

Foam texture (n) can be defined as the number of bubbles per unit volume [93], being a way to quantify the strength of the foam. Considering a homogeneous medium and incompressible flow, the foam transport can be described as [13]:

$$\varphi \frac{\partial}{\partial t}(S_g n) + \frac{\partial}{\partial x}(u_g n) = \Phi, \tag{2.49}$$

where S_g is the gaseous (foam) phase saturation, u_g is the foam superficial velocity, and Φ is the source term. This term can be expressed as the difference between functions describing the bubble generation and the coalescence rates ($\Phi = r_g - r_c$).

The SBP model proposed by Zitha and Du [13] simplifies the number of parameters to be fitted compared to other foam models [37, 38]. It remains robust enough to predict foam behavior in porous media [13]. The authors model the source term as

$$\Phi = \varphi S_g [K_g(n_{max} - n) - K_d n], \tag{2.50}$$

where K_g and K_d are the bubble generation and coalescence rate coefficients, which can be obtained experimentally. This term can be rewritten as $\Phi = \varphi S_g (K_d + K_g)(n_\infty - n)$, where the equilibrium foam texture is $n_\infty = n_{max} K_g (K_d + K_g)^{-1}$. In [92], the authors prove that, mathematically, both cases $K_d = 0$ and $K_d \neq 0$ are equivalent. Thus, without loss of generality, considering $K_d = 0$ we obtain $n_\infty = n_{max}$ and

$$\Phi = \varphi S_g K_g (n_\infty - n). \tag{2.51}$$

Although the source term is simple, the modification of gas mobility is quite complex, being included in the gas's relative permeability and viscosity.

Often, we use the dimensionless foam texture $n_D = n/n_{max}$, where n_{max} is a maximum value (at equilibrium). Ashoori et al. [14] proposed a foam model with the source term similar to [13], but including the gas mobility reduction in the foam relative permeability (k_{rg}^f) as

$$k_{rg}^f = \frac{k_{rg}}{18500 n_D + 1}, \tag{2.52}$$

where k_{rg} is the foam-free gas relative permeability. Combining these two works [13, 14], Zavala et al. [92] presented the following foam model for a water-gas flow

$$\varphi \frac{\partial S_w}{\partial t} + \frac{\partial}{\partial x}\left(u f_w + \left(f_w \lambda_g \frac{dP_c}{dS_w} \right) \frac{\partial S_w}{\partial x} \right) = 0, \tag{2.53}$$

$$\varphi \frac{\partial}{\partial t}(S_g n_D) + \frac{\partial}{\partial x}(u_g n_D) = \Phi, \tag{2.54}$$

where $\Phi = \varphi S_g K_g (1 - n_D)$. The authors consider a saturated porous medium ($S_g + S_w = 1$), incompressible phases, and small capillary pressure gradients. Following the definitions presented in Subsection **2.2.1**, the fractional flow of water and the relative mobilities of water and gas are given by

$$f_w = \frac{\lambda_w}{\lambda_w + \lambda_g}, \quad \lambda_w = \frac{k k_{rw}}{\mu_w}, \quad \lambda_g = \frac{k k_{rg}}{\mu_g}. \tag{2.55}$$

As we consider the porous medium saturated, the fractional flow function of the gas phase can be written as $f_g = 1 - f_w$. The relative permeability of water and foam-free gas phases are Corey type:

$$k_{rw}(S_w) = \begin{cases} 0, & 0 \le S_w \le S_{wc}, \\ c_{k_{rw}} \left(\frac{S_w - S_{wc}}{1 - S_{wc} - S_{gr}} \right)^{n_w}, & S_{wc} \le S_w \le 1, \end{cases} \tag{2.56}$$

$$k_{rg}(S_w) = \begin{cases} c_{k_{rg}} \left(\frac{1 - S_w - S_{gr}}{1 - S_{wc} - S_{gr}} \right)^{n_g}, & S_{wc} \le S_w \le 1 - S_{gr}, \\ 0, & 1 - S_{gr} \le S_w \le 1, \end{cases} \tag{2.57}$$

where $c_{k_{rw}}$, $c_{k_{rg}}$ are the endpoints relative permeability of water and gas phases, S_{wc} is the connate water saturation, and S_{gr} is the residual gas saturation. The exponents are $n_w = \tau$ and $n_g = (3\tau + 2)/\tau$, with τ being the a pore size distribution parameter. Based on [14], the foam action is included in the gas relative permeability (but not water [12]) through a Mobility Reduction Factor (MRF):

$$k_{rg}^f(S_w, n_D) = \frac{k_{rg}(S_w)}{\mathrm{MRF}(n_D)}, \tag{2.58}$$

where $MRF = \beta n_{max} n_D + 1$ (β is a mobility parameter).

Including nanoparticles in foam flow models is a challenge, especially when considering their impact on bubble generation and coalescence process [94]. Therefore, researchers

often use an implicit approach to calibrate the foam parameters using experimental data of NP-stabilized foam flow [30, 40, 95]. In [41], the authors propose a mechanistic model describing the transport of nanoparticles with and by foam. This work focuses on nano-remediation, a technique that injects reactive nanoparticles into the subsurface to displace or degrade contaminants. Foam can be used to improve this method by inhibiting the attachment and aggregation of nanoparticles and controlling their mobility. In EOR applications, foam is used to control gas mobility while nanoparticles improve foam stability, so the way foam and nanoparticles are coupled is different. The model [41] accounts for nanoparticle aggregation and attachment processes, the effect of nanoparticles on bubble generation and coalescence, and considers nanoparticles in the liquid, gas, or even both phases. Hence, this model is too complex for analytical investigation, being solved only numerically in [41].

2.4 NANOPARTICLE TRANSPORT AND RETENTION

Mechanical entrapment and adsorption are important retention mechanisms affecting the transport of particles in porous media [33, 96, 97]; see Fig. 11. Mechanical entrapment (size exclusion) occurs when pore throats block the passage of particles during a suspension flow, playing a crucial role in maintaining particle concentration over long distances [33, 49]. Adsorption refers to the attachment of particles to the rock surface due to intermolecular forces, which may involve both physical and chemical interactions, affecting the propagation speed of the particle suspension in porous media [98]. Pore throats in reservoir rocks are typically much larger than nanoparticles, reducing the chance of retention by size exclusion. However, agglomeration is a significant phenomenon during nanoparticle transport and can completely alter the dominant retention mechanisms, as nanoparticle aggregates behave like larger particles [99].

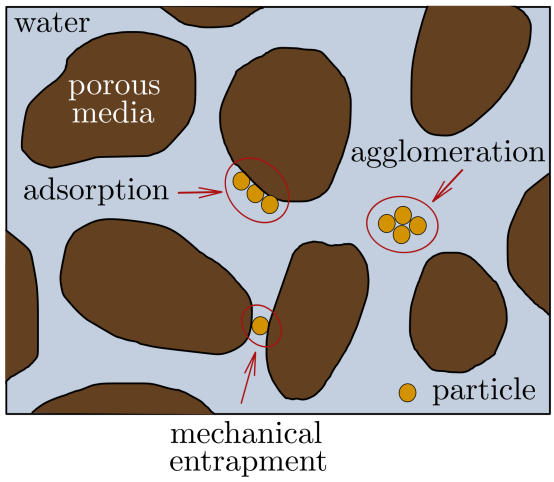

Figure 11 – Example of processes impacting particle transport through porous media: Mechanical entrapment (size exclusion), adsorption (related to physicochemical interactions), and agglomeration (particles aggregation).

Predicting and controlling the nanoparticle interaction with the porous medium is a huge challenge since many factors influence agglomeration and retention processes. In the context of EOR, the electrostatic interactions between nanoparticles and the porous medium are critical, as reservoir rock surfaces typically carry ionic charges [100]. Moreover, it is worth noting that nanoparticle concentrations used in EOR applications are significantly higher than those typically found in environmental impact studies [101].

Several experiments have investigated nanoparticle transport and retention in porous media [32, 97, 98, 100, 102–105]. The findings indicate that the main factors influencing nanoparticle retention include their type and size, the concentration and ionic strength of the injected solution, the flow rate, and the surface charges of both nanoparticles and rock [102, 106]. In [103], micromodel tests were conducted to examine the transport behavior of various types of nanoparticles (MgO, SiO_2, and Al_2O_3). The findings revealed that high concentrations led to a significant decrease in permeability for all nanoparticle types, primarily due to the pore-plugging process. In [97], single-phase core-flooding experiments were performed to examine the transport of silica nanoparticles through dolomite rocks. The authors found that higher nanoparticle concentrations and increased aqueous phase ionic strength decrease nanofluid stability (the average size of nanoparticles increased), leading to greater nanoparticle retention in the rock and significant permeability reduction.

There are divergent results regarding whether the nanoparticle attachment to the rock surface is reversible (recovery of nearly all the injected particles) or presents reversible and irreversible behaviors. Reversible retention impacts the propagation speed of nanoparticle suspension in porous media, while irreversible entrapment is crucial for maintaining a certain nanoparticle concentration over long distances [98]. In [32] and [100], core-flooding experiments with surface-treated nanoparticles indicated low retention (between 1 and 10 wt%) and some delay in the arrival of the injected nanoparticles. Based on these findings, the authors concluded that attractive interactions between particles and pore walls were the dominant retention mechanism, indicating reversible physicochemical adsorption. In [98], a comprehensive set of transport experiments for surface-coated silica were conducted in both core plugs and columns packed with crushed sedimentary rock. Their results and analysis suggest that both reversible and irreversible retention occur, and finite retention capacities exist for both cases. In [104], the authors investigated the adsorption of silica nanoparticles on carbonate surfaces under simulated reservoir conditions. They concluded that reversible adsorption was predominant, with the initial hydrophilicity of both the nanoparticles and the rock surface significantly affecting particle retention.

Based on previous experimental results, we conclude that mechanical entrapment is a significant factor in nanoparticle transport through porous media, although in certain

cases, it can be reasonably considered negligible. In addition to lower nanoparticle concentrations and reduced fluid ionic strength, an analysis of experiments reporting low retention highlights the importance of proper surface coatings (which keeps nanoparticles individually dispersed in water). In studies involving the co-injection of nanoparticle solutions (with or without surfactants) and gas, the focus is primarily on the potential of nanoparticles to stabilize foam. Notably, studies such as [17, 23, 107] included retention tests; however, these tests were conducted separately from the gas injection. It is assumed that retention is lower during foam flooding, as nanoparticles tend to migrate to the gas-liquid interface [17, 107].

In this thesis, we study nanoparticle retention in porous media associated with NP-stabilized foam injection. Nevertheless, studying the transport and retention of particles in porous media is highly relevant for another technique: polymer injection [33, 96, 108]. Moreover, it can also be significant in contexts where no particles are intentionally injected since even filtered injected water contains suspended particles [109] and particles from the porous medium itself may detach and subsequently redeposit during flow [110, 111].

2.5 UNCERTAINTY QUANTIFICATION

The uncertainty of the model's parameters is described in terms of probability distributions. For a random variable $Z \in \mathbb{R}$, we define the cumulative distribution function (CDF) as $H_Z(z) = P(Z \leq z)$ (the probability of this variable being less or equal to z). For continuous variables, we define the probability density function (PDF) as

$$h(z) = dH_Z/dz. \tag{2.59}$$

Then, we can rewrite the CDF as follows

$$H_Z(z) = \int_{-\infty}^{z} h(z')\, dz'. \tag{2.60}$$

We employ the classical Monte Carlo method to propagate the uncertainty of input parameters to the quantities of interest. This method involves generating samples from distributions and using them to derive information about the distributions [112]. Consider $Z \in \mathbb{R}^{N_p}$ an input vector defined on the sample space $\mathcal{D}$, where N_p is the number of uncertain parameters. For each input, the model returns a quantity of interest $\mathcal{Y} = \mathcal{M}(Z)$. We are interested in their expected value, defined by

$$\mathbb{E}[\mathcal{Y}] = \int_{\mathcal{D}} \mathcal{M}(\mathcal{Y}) h(z)\, dz, \tag{2.61}$$

where $h(z)$ is the PDF for the inputs. Using the MC estimator with N independent and identically distributed random samples, we approximate this integral as [112]

$$I_N \equiv \frac{1}{N} \sum_{n=1}^{N} \mathcal{Y}(Z). \tag{2.62}$$

To study the convergence of the method, we must determine the variance in I_N, which can be approximated by the variance in the samples. Consider the sample variance of the probability distribution of a QoI:

$$\sigma_N^2 = \frac{1}{N-1}\sum_{n=1}^{N}(\overline{\mathcal{Y}}_N - \mathcal{Y}(z_n))^2, \tag{2.63}$$

with $\overline{\mathcal{Y}}_N$ being the sample mean of the N samples. Then, as $N \to \infty$, the error in the estimate converge to a normal distribution with mean zero and variance given by

$$\mathbb{V}(I_N - \mathbb{E}[\mathcal{Y}]) = \sigma_N^2/N. \tag{2.64}$$

This result is based on the Central Limit Theorem and shows that the Monte Carlo estimator's error decreases as $\sqrt{N}$, with a constant that depends on the QoI sample variance [112].

2.6 SENSITIVITY ANALYSIS

The sensitivity analysis quantifies the contribution of each uncertain input to the output variability. This helps identify insignificant inputs and quantify the impact on the output uncertainty if an input is known exactly [113]. There are several methods to perform sensitivity studies. We conduct a variance-based SA using the main and total Sobol indices [65], which are defined below.

The main Sobol index, also known as the first-order Sobol index, quantifies the direct contribution of a particular uncertain input z_i to the variance of the output $\mathcal{Y}$. It is defined as [114]:

$$\mathcal{S}_i = \frac{\mathbb{V}[\mathbb{E}[\mathcal{Y}(z_i)]]}{\mathbb{V}[\mathcal{Y}]}. \tag{2.65}$$

The total Sobol index can be expressed as [114]

$$\mathcal{S}_{T_i} = 1 - \frac{\mathbb{V}[\mathbb{E}[\mathcal{Y}(z_{-i})]]}{\mathbb{V}[\mathcal{Y}]}, \tag{2.66}$$

where z_{-i} is the set of all input parameters except z_i. It is used to estimate changes in $\mathbb{V}[\mathcal{Y}]$ taking into account first- and high-order interactions between different uncertain inputs, which is neglected by the main Sobol index.

The variance of the model is decomposed into the sum of variances associated with each input variable and their interaction effects. We perform MC simulations to obtain these variances through the UQLab [115, 116]. In this package, the Janon estimator [117] is used to compute total indices; see [116] for details.

3 NP-STABILIZED FOAM FLOW MODEL WITHOUT PARTICLE RETENTION

In this chapter, we propose a model describing NP-stabilized foam flow in porous media, considering foam in local equilibrium and without nanoparticle retention. The proposed model is a non-strictly hyperbolic system and, following the Conservation Laws Theory [46,47], we search for solutions as a sequence of waves. Isaacson [88] and Johansen and Winther [89] solved similar models applied to water-oil flow, with polymers as a tracer. In [88], there are linearly degenerate and genuinely nonlinear families, while in [89], both families are not degenerate. In the present study, one family is linearly degenerate (related to shock and rarefaction waves), and the other possesses local linear degeneracies (related to contact discontinuities); the same classification appears in [118]. We construct the solutions through a sequence of proofs following a classical framework [88] and also [91]. Then, we use the obtained solution to investigate the effect of nanoparticle concentration on water production and the breakthrough time.

Section 3.1 introduces the model assumptions and formulates the governing equations. In Section 3.2, we obtain the analytical solution for this model. Section 3.3 presents the model setup based on experimental data. In Section 3.4, we compare the analytical solution with numerical simulations. Section 3.5 investigates practical applications for NP-stabilized foam flow using the analytical framework. In Section 3.7, we present discussions and partial conclusions based on the results presented in this chapter.

The results presented in this chapter are summarized in the paper [64].

3.1 GOVERNING EQUATIONS

Let us consider one-dimensional water-gas flow in a saturated porous medium in the presence of foam and with suspended nanoparticles in the aqueous phase. Both phases are assumed to flow simultaneously during the co-injection of gas and a solution containing surfactants and nanoparticles. As is usual in the literature [14,15,39,92,119], we consider the following model assumptions. The gas and liquid phases are treated as incompressible and immiscible, and the porous medium is considered homogeneous. Additionally, we adopt a large-scale approximation, i.e., the diffusion terms are neglected compared with the advective fluxes.

Considering foam in local equilibrium and following [13,88,89,92], this phenomenon is described by the system:

$$\varphi \frac{\partial S_w}{\partial \bar{t}} + \frac{\partial}{\partial \bar{x}}(u f_w) = 0, \tag{3.1}$$

$$\varphi \frac{\partial}{\partial \bar{t}}(S_w C_{np}) + \frac{\partial}{\partial \bar{x}}(u f_w C_{np}) = 0, \tag{3.2}$$

where S_w is the water saturation, φ is the porosity of the medium, u is the superficial velocity of the mixture (water and gas), C_{np} is the nanoparticle concentration, and $f_w = f_w(S_w, C_{np})$ is the fractional flow function of the water phase. The first equation models the water mass balance, and the second models the nanoparticle transport.

We define f_w and the relative permeability of water and foam-free gas phases as in Eqs. (2.55), (2.56), and (2.57). Since we assume the equilibrium between bubble generation and coalescence rates, we also include foam action through MRF (see Eq. (2.58)), but here it is a function of nanoparticle concentration:

$$k_{rg}^f(S_w, C_{np}) = \frac{k_{rg}(S_w)}{\mathrm{MRF}(C_{np})}. \tag{3.3}$$

Based on [14, 92], MRF is defined as follows

$$\mathrm{MRF}(C_{np}) = \beta n_{max}(C_{np}) + 1, \tag{3.4}$$

with the maximum foam texture n_{max} (mm^{-3}) depending on C_{np}. Note that foam is a non-Newtonian fluid with apparent viscosity given by [93]

$$\mu_{app} = \mu_g + \alpha n u_f^{-d}, \tag{3.5}$$

where the constants α and d are related to the viscosity of the fluids, μ_g is the foam-free gas viscosity, and n is the foam texture. Therefore, to estimate the mobility parameter β, following [92] we equate the mobilities from Eq. (3.5) (with foam texture $n = n_{max}$) and the one presented in Eq. (2.55):

$$k\frac{k_{rg}^f}{\mu_g + \alpha n_{max} v_f^{-d}} = k\frac{k_{rg}^f}{\mu_g(1 + \beta n_{max})} \Rightarrow \beta = \frac{\alpha}{v_f^d \mu_g}. \tag{3.6}$$

We consider $v_f = u_g/(S_g\varphi)$ as an estimate for foam velocity, using $S_g = 1$ for calculations.

In [30], experimental data of NP-stabilized foam [19] were used to calibrate the n_{max} parameter of the SBP model. For silica (SiO_2) nanoparticles and sodium dodecyl sulfate (SDS) surfactant, the authors obtained that when the nanoparticle concentration increases from 0.0 to 2.0 wt%, the n_{max} value increases from 500 mm^{-3} to 5500 mm^{-3}; see Fig. 12. In [25], several experimental studies of NP-stabilized foam were reviewed. They investigate an optimal nanoparticle concentration based on the experiments found in the literature using foam stability. We call attention to two works that also used SDS and presented similar results. Karakashev et al. [120] analyzed nanoparticle concentrations up to 4.0 wt%, and they observed that the influence of particles on the foam stability became insignificant above 1.0 wt%. In [22], the authors studied nanoparticle concentrations up to 5.0%, and they observed that above 1.0 wt% the foam stability decreased. Using these results, we propose the maximum foam texture as an increasing linear function of C_{np} until 1.0%; above this value, n_{max} is constant:

$$n_{max}(C_{np}) = \begin{cases} b_1 C_{np} + b_2, & 0.0 \leq C_{np} \leq 1.0\,\mathrm{wt\%}, \\ b_1 + b_2, & C_{np} > 1.0\,\mathrm{wt\%}. \end{cases} \tag{3.7}$$

Figure 12 shows the n_{max} values calibrated by [30] and the corresponding function proposed in Eq. (3.7), where we use the least squares method to derive the mean values $b_1 = 2531.80$ mm^{-3} and $b_2 = 802.58$ mm^{-3}. For simplicity, we adopt from now on $0.0\% \leq C_{np} \leq 1.0\%$, since we consider that the foam texture is constant for nanoparticle concentration above $C^*_{np} = 1.0\%$.

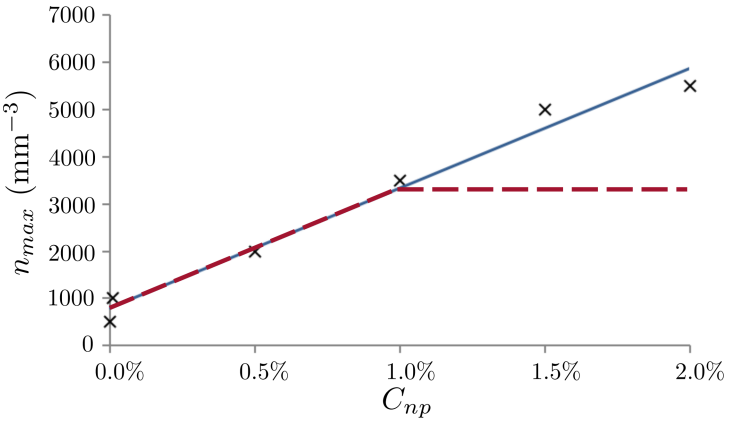

Figure 12 – Maximum foam texture under different nanoparticle concentrations. Approximation by least squares method (blue line) based on experimental data [19, 30] for concentrations 0.1%, 0.5%, 1.0%, 1.5%, and 2.0% (cross-mark). The function defined by Eq. (3.7) (red dashed line) is constant for nanoparticle concentration above 1.0% [22, 120].

Consider dimensionless time and length variables $t = \bar{t}/t^*$ and $x = \bar{x}/x^*$, where $t^* = L\varphi(1 - S_{wc} - S_{gr})u^{-1}$ and $x^* = L$, respectively (L is the length of the reservoir). Using t, x, and normalized water saturation and nanoparticle concentration:

$$S = \frac{S_w - S_{wc}}{1 - S_{wc} - S_{gr}}, \quad C = \frac{C_{np}}{C^*_{np}}, \tag{3.8}$$

the system (3.1)-(3.2) is rewritten as

$$\partial_t S + \partial_x f(S, C) = 0, \tag{3.9}$$

$$\partial_t \left[(S + a)C\right] + \partial_x \left[f(S, C)C\right] = 0, \tag{3.10}$$

where $(S, C) \in I \times I$, with $I = [0, 1]$ and $(x, t) \in \mathbb{R} \times \mathbb{R}^+$. The constant a is defined as $a = S_{wc}/(1 - S_{wc} - S_{gr})$. The dimensionless and normalized water fractional flow function $f : I \times I \to \mathbb{R}$ is given by

$$f(S, C) = \frac{k_{rw}(S)}{k_{rw}(S) + (\mu_w/\mu_g)k_{rg}(S, C)}, \tag{3.11}$$

with relative permeabilities

$$k_{rw}(S) = c_{k_{rw}} S^{n_w}, \quad k^f_{rg}(S, C) = \frac{c_{k_{rg}}(1 - S)^{n_g}}{\mathrm{MRF}(C)}. \tag{3.12}$$

In this work, we study the local equilibrium NP-stabilized foam flow model (3.9)-(3.10) using two relative permeability functions by changing the Corey exponents n_w, n_g (and

endpoints $c_{k_{rw}}$, $c_{k_{rg}}$) of Eq. (3.12). In the practical results of this chapter, we consider the same permeability functions used in [43, 92], where $n_w = \tau$ and $n_g = (3\tau + 2)/\tau$, with the pore-size-distribution parameter $\tau = 5.0$. Chapter 4 investigates a simpler case, where $n_w = n_g = 2$, to facilitate the uncertainty quantification and sensitivity analysis studies. We will refer to these two models as original and quadratic models.

Remark 3.1. *Notice that the non-dimensionalization results in system* (3.9)-(3.10) *with the accumulation term containing the constant a. The same term appears when modeling the foam flow with linear adsorption. Thus, the introduction of linear adsorption into the model depends only on changing the meaning of the constant a; see [91]. In that way, the analytical results presented in this work are valid for the model with linear adsorption.*

Let us define $U = (S, C)^T \in \Omega$; hereafter, we drop out the notation T for simplicity. The system (3.9)-(3.10) can be rewritten in the matrix form as

$$\partial_t U + A(U)\partial_x U = 0, \tag{3.13}$$

with $A(U)$ being the Jacobian matrix

$$A = \begin{bmatrix} \partial_S f & \partial_C f \\ 0 & f/(S+a) \end{bmatrix}. \tag{3.14}$$

The next chapter presents the construction of a weak solution to the Riemann problem given by system (3.13) with initial condition $U_0(x) = U(x, 0)$ as follows

$$U_0(x) = \begin{cases} U_L, & \text{if} \quad x < 0, \\ U_R, & \text{if} \quad x \geq 0. \end{cases} \tag{3.15}$$

The left state $U_L = (S_L, C_L)$ represents the injection condition, and the right state $U_R = (S_R, C_R)$ represents the initial reservoir condition.

3.2 ANALYTICAL SOLUTION

In this section, we construct the solution to the Riemann problem (3.13)-(3.15). The analytical framework developed here holds for any flux function $f : I \times I \to \mathbb{R}$, where $I = [0, 1]$, satisfying the following properties.

(i) The function f is continuous with all partial derivatives, up to the second order, continuous ($f \in \mathcal{C}^2$). Also, $f(0, C) = 0$ and $f(1, C) = 1$, $\forall C \in I$.

(ii) The derivative of f in relation to S satisfies $\partial_S f(S, C) > 0$ for $0 < S < 1$ and $\partial_S f(0, C) = \partial_S f(1, C) = 0$ $\forall C \in I$.

(iii) The derivative of f in relation to C satisfies $\partial_C f(S, C) > 0$ for $0 < S < 1$, $\forall C \in I$.

(iv) For each fixed $C \in I$, $f(S, C)$ possesses a single inflection point $0 < S^I(C) < 1$, such that $\partial_{SS} f(S, C) > 0$ for $0 \leq S < S^I$ and $\partial_{SS} f(S, C) < 0$ for $S^I < S \leq 1$.

Now, we will prove that the fractional flow function presented in Eq. (3.11) satisfies these properties for both relative permeability models considered in this work. For the more realistic case, the proof of property (iv) is partial, being verified only numerically. However, we present a complete proof for the quadratic case. In [88, 89], the properties used to obtain the solution are the same, except that f is an increasing function of C here, while it is a decreasing function in these works.

Proposition 3.1. *The function $f : I \times I \to \mathbb{R}$ presented in Eq.* (3.11) *satisfies the properties (i)-(iv) for both original ($n_w = 5$ and $n_g = 3.4$) and quadratic ($n_g = n_w = 2$) relative permeability models.*

Proof. Once the model constants are all strictly positives, the relative permeabilities are non-negative, and their derivatives satisfy $\partial_S k_{rg}(S, C) \leq 0$, $\partial_C k_{rg}(S, C) \leq 0$, and $k'_{rw}(S) \geq 0$.

(i) Due to the definition of the functions k_{rw}, k_{rg} and MRF, we conclude that $f \in \mathcal{C}^2$. Since $k_{rw}(0) = 0$ and $k_{rg}(0, C) > 0$, it follows that $f(0, C) = 0$ for all $C \in I$. In the same way, from $k_{rw}(1) = c_{k_{rw}}$ and $k_{rg}(1, C) = 0$ we conclude that $f(1, C) = 1$ for all $C \in I$.

(ii) The partial derivative of f in relation to S is given by

$$\partial_S f(S, C) = \frac{\mu_w}{\mu_g} \frac{k'_{rw}(S) k_{rg}(S, C) - k_{rw}(S) \partial_S k_{rg}(S, C)}{[k_{rw}(S) + (\mu_w/\mu_g) k_{rg}(S, C)]^2}. \tag{3.16}$$

For the case $S = 0$ we obtain $k_{rw}(0) = k'_{rw}(S) = 0$. While, for the case $S = 1$ we obtain $k_{rg}(1, C) = \partial_S k_{rg}(1, C) = 0$. Both cases result on $\partial_S f(S, C) = 0$ for all $C \in I$. In addition, for $0 < S < 1$ yields $\partial_S k_{rg}(S, C) < 0$. Once the other terms in (3.16) are strictly positive, we obtain $\partial_S f(S, C) > 0$ for all $C \in I$.

(iii) The partial derivative of f in relation to C is given by

$$\partial_C f(S, C) = -\frac{\mu_w}{\mu_g} \frac{k_{rw}(S) \partial_C k_{rg}(S, C)}{[k_{rw}(S) + (\mu_w/\mu_g) k_{rg}(S, C)]^2}. \tag{3.17}$$

If $0 < S < 1$, it follows that $\partial_C f(S, C) > 0$ for all $C \in I$, once $\partial_C k_{rg}(S, C) < 0$ and the other terms in (3.17) are strictly positives. Notice that $\partial_C k_{rg}(S, C) = 0$ only if $S = 1$ for all $C \in I$.

(iv) To determine the inflection points of f for each fixed C, we need to analyze the equation $\partial_{SS} f(S, C) = 0$. For the quadratic case, we can rewrite the fractional flow function (3.11) as $f(U) = S^2/(S^2 + p(C)(1 - S)^2)$, with $p(C) =$

$(\mu_w c_{k_{rg}})/[(\mu_g c_{k_{rw}})MRF(C)]$. Then, the second partial derivative of f in relation to S is given by

$$\partial_{SS} f(S,C) = \frac{(4S^3 - 6S^2 + 2)p(C)^2 + (4S^3 - 6S^2)p(C)}{[S^2 + p(C)(1-S)^2]^3}. \tag{3.18}$$

The inflection points $S^I(C)$ for each fixed C are the real roots (inside the interval I) of the equation $\partial_{SS} f(S,C) = 0$. After some simplifications, it can be rewritten as

$$4[p(C)+1]S^3 - 6[p(C)+1]S^2 + 2p(C) = 0. \tag{3.19}$$

Using the Cardano's Method [121, 122], the discriminant of Eq. (3.19) is

$$\Delta(C) = \frac{p(C)^2}{16(p(C)+1)^2} - \frac{p(C)}{16(p(C)+1)}. \tag{3.20}$$

For all $C \in I$, we obtain $0 < p(C)/[p(C)+1] < 1$ (as $p(C) > 0$) yielding $\Delta(C) < 0$. Then, we have three real and different roots:

$$S_j(C) = \frac{1}{2} + \cos\left(\frac{\theta(C) + 2j\pi}{3}\right), \quad j = 0, 1, 2, \tag{3.21}$$

where $\theta(C) = \arccos(1 - 2p(C)/[p(C)+1])$. Substituting the constants of the model (see Tab. 2 in Section 3.3), only $S_2(C) = 1/2 + \cos((\theta + 4\pi)/3)$ is in $(0,1)$. Note that, from Eq. (3.18), if $S = 0 < S^I(C)$ we obtain $\partial_{SS} f(S,C) = 2/p(C) > 0$ and if $S = 1 > S^I(C)$ we obtain $\partial_{SS} f(S,C) = -2p(C) < 0$, so the proof is complete.

We numerically verify this property for the fractional flow function with $n_w = 5$ and $n_g = 3.4$, due to its complexity. In [123], the authors proved that a flux function with convex permeability Corey models has an S-shape for the class of power-law permeabilities. The left panel in Fig. 13 shows the $f(S,C)$ graph for several values of C. Notice that all curves give the impression of an S-shape, indicating the existence of a single inflection point for each curve. This becomes clearer for $\partial_{SS} f(S,C)$ graph; see the right panel in Fig. 13. Besides the existence of a single $0 < S^I < 1$, such that the second derivative in S is null, for each fixed C the graphs also shows that $\partial_{SS} f(S,C) > 0$ for $0 \leq S < S^I$ and $\partial_{SS} f(S,C) < 0$ for $S^I < S \leq 1$.

□

3.2.1 Preliminary results

As seen in Chapter 2, the typical solution for a non-linear system of conservation laws is a sequence of fundamental waves: shocks, rarefactions, and contacts, each of them connecting left and right states [46, 47]. To construct the wave sequences, we first need to

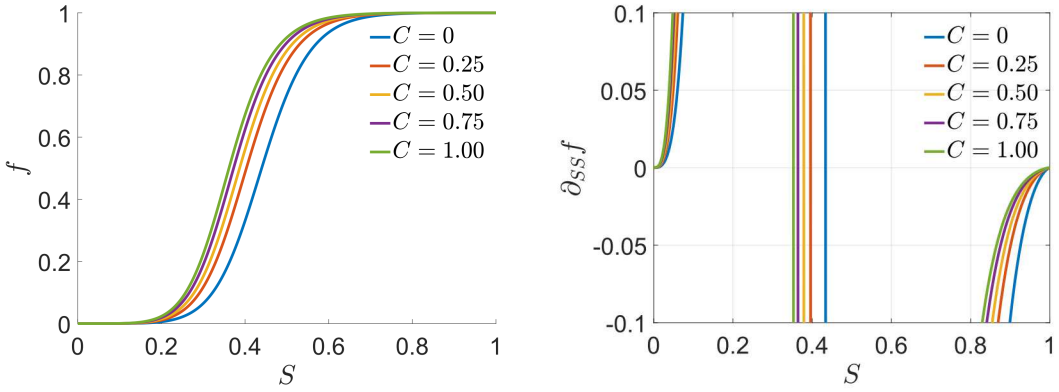

Figure 13 – Inflection points of the fractional flow function (original model) for several values of C. The left panel shows $f(S, C)$, and the right panel shows their second derivatives $\partial_{SS} f(S, C)$. There is only one inflection point for each C.

identify and classify the characteristic fields associated with S and C. From the eigenvalues (λ_C, λ_S) and eigenvectors (e_C, e_S) associated with system (3.13):

$$\begin{aligned} \lambda_C &= f/(S+a), \quad & e_C &= (\partial_C f, f/(S+a) - \partial_S f), \\ \lambda_S &= \partial_S f, & e_S &= (1, 0), \end{aligned} \tag{3.22}$$

we obtain that

$$\nabla \lambda_C \cdot e_C = \left(\frac{\partial_S f (S+a) - f}{(S+a)^2}, \frac{\partial_C f}{S+a} \right) \cdot \left(\partial_C f, \frac{f}{S+a} - \partial_S f \right) = 0, \tag{3.23}$$

for all $(S, C) \in I \times I$. Therefore, the C-family is linearly degenerate, and it follows that the elementary waves associated with this characteristic field are contact discontinuities; see Subsection **2.1.2**. Conversely, for the S-family, we obtain

$$\nabla \lambda_S \cdot e_S = (\partial_{SS} f, \partial_{CS} f) \cdot (1, 0) = \partial_{SS} f, \tag{3.24}$$

so this family presents a local linear degeneracy once f possesses an inflection point (as shown in Prop. 3.1). Thus, the solutions can be a shock, a rarefaction, or a combination of these waves [46]. The eigenvector of the S-family is $e_S = (1, 0)$ (3.22), then the integral curve is a straight line, and the value of C remains constant. Therefore, it follows the typical Buckley-Leverett type solution presented in Subsection **2.1.1**.

To analyze the fundamental waves, let us examine $U^- = (S^-, C^-)$ and $U^+ = (S^+, C^+)$, representing each wave's left and right states. Shock waves or contact discontinuities satisfy Rankine-Hugoniot condition (see Eq. (2.11) in Section 2.1), which, applied to system (3.13), is

$$\sigma(S^+ - S^-) = f(U^+) - f(U^-), \tag{3.25}$$

$$\sigma[C^+(S^+ + a) - C_L(S^- + a)] = C^+ f(U^+) - C^- f(U^-), \tag{3.26}$$

where σ is the propagation velocity of the discontinuity connecting U^- to U^+. From Eqs. (3.25) and (3.26), we obtain

$$\sigma = \frac{f(U^+) - f(U^-)}{S^+ - S^-}, \tag{3.27}$$

$$(C^+ - C^-)(f(U^-)(S^+ + a) - f(U^+)(S^- + a)) = 0. \tag{3.28}$$

There are two possibilities for Eq. (3.28). If $C^+ = C^-$, the states U^- and U^+ are on the same fractional flow curve, and the solution is a shock with propagation velocity $\sigma_S = \sigma$ given by Eq. (3.27). Another option is $C^+ \neq C^-$, yielding

$$\lambda_C(U^+) = \frac{f(U^+)}{S^+ + a} = \frac{f(U^-)}{S^- + a} = \lambda_C(U^-), \tag{3.29}$$

that is, the solution is a contact wave with velocity [46]

$$\sigma_C = \lambda_C(U^-) = \lambda_C(U^+). \tag{3.30}$$

For rarefaction waves, the velocity is given by [46, 47]

$$\sigma_S(U) = \lambda_S(U), \quad \text{with } U^- \leq U \leq U^+. \tag{3.31}$$

Since shock and rarefaction waves are in the same family, following [88], we use the notation S-wave for shock, rarefaction, or rarefaction followed by shock (from left to right or from upstream to downstream). Contact discontinuities will be called C-waves. To represent that an S-wave connects a left state U^- to a right state U^+, we write $U^- \xrightarrow{S} U^+$ [88]. The initial velocity v_i^S and final velocity v_f^S represent the velocities of the tail (U^-) and the head (U^+) of the S-wave. For rarefaction or rarefaction followed by shock, $v_i^S \neq v_f^S$, as presented in Eq. (3.31). Analogously, $U^- \xrightarrow{C} U^+$ means that a C-wave connects U^- to U^+ with initial velocity v_i^C and final velocity v_f^C. However, in this case, $v_i^C = v_i^S$; see Eq. (3.30). Note that when both left and right states are on the same fractional flow curve (the concentration of nanoparticles is constant), the solution is an S-wave. The C-wave appears just when we move from one fractional flow curve to another (the concentration of nanoparticles changes).

The following proposition proves that there exists a curve where the characteristic velocities coincide, and system (3.13) is non-strictly hyperbolic. This curve divides the parameter space into three regions, leading to different solution sequences, as presented in the next chapter.

Proposition 3.2. *For each fixed $C \in I$, there exists a unique $\hat{S} = \hat{S}(C)$ in the interior of the interval I, such that $\lambda_C(\hat{S}, C) = \lambda_S(\hat{S}, C)$.*

Proof. Let us consider $\phi : I \to \mathbb{R}$ given by

$$\phi(S) = f(S, C) - \partial_S f(S, C)(S + a). \tag{3.32}$$

It follows that $\phi(S) = 0 \Leftrightarrow f(S,C)/(S+a) = \partial_S f(S,C)$, that is, $\lambda_C(S,C) = \lambda_S(S,C)$. We will show that ϕ possesses only one root in the open interval $(0,1)$. From $\phi'(S) = -\partial_{SS} f(S,C)(S+a)$ and the condition *(v)* of Prop. 3.1, yields

$$\phi'(S) < 0, \text{ if } S < S^I, \quad \phi'(S) = 0, \text{ if } S = S^I, \quad \phi'(S) > 0, \text{ if } S > S^I. \tag{3.33}$$

Since $\phi(0) = f(0,C) - \partial_S f(0,C)a = 0$ and $\phi(1) = f(1,C) - \partial_S f(1,C)(1+a) = 1$, by the Intermediate Value Theorem [124] for all q in the interval $0 = \phi(0) \leq q \leq \phi(1) = 1$ there is some p such that $\phi(p) = q$. In particular, this also holds for $q = 0$. As for uniqueness, once $\phi'(S) < 0$ and S^I is the minimum of ϕ, if $S < S^I$, it follows that ϕ is a decreasing function. This concludes that $\phi(S^I) < 0$. On the other hand, $\phi'(S) > 0$ if $S > S^I$, so ϕ is strictly increasing in this interval and $\phi(S^I) < 0 \leq \phi(1) = 1$. Thus, there exists a unique $\hat{S}$ such that $\phi(\hat{S}) = 0$.

□

The set $(\hat{S}, C)$ for each C defines a curve in the phase plane S-C called the transition curve and is denoted by $\mathcal{T}$. As in [89], we divide the phase plane into sets $\mathcal{L}$ and $\mathcal{R}$, located to the left and the right of $\mathcal{T}$, respectively; see the left panel in Fig. 14. These sets are defined as

$$\begin{aligned} \mathcal{T} &= \{(S,C) \in I \times I \mid \lambda_C(U) = \lambda_S(U)\}, \\ \mathcal{L} &= \{(S,C) \in I \times I \mid \lambda_C(U) < \lambda_S(U)\}, \\ \mathcal{R} &= \{(S,C) \in I \times I \mid \lambda_C(U) > \lambda_S(U)\}. \end{aligned} \tag{3.34}$$

Now, let us study the behavior of the curve

$$\lambda_C(S,C) = \frac{f(S,C)}{S+a} = \kappa, \tag{3.35}$$

in the phase plane S-C, where κ is a constant. Using the Implicit Function Theorem [124], Eq. (3.35) defines the function $C_\kappa(S)$. Differentiating Eq. (3.35) with respect to S along the curve $\lambda_C = \kappa$, we obtain

$$C'_\kappa(S) = \frac{\lambda_C - \lambda_S}{\partial_C f}. \tag{3.36}$$

Using the phase plane S-C definition (17), yields

$$C'_\kappa(S) < 0 \text{ in } \mathcal{L}, \quad C'_\kappa(S) > 0 \text{ in } \mathcal{R}. \tag{3.37}$$

Thus, the function λ_C in the phase plane S-C is concave up, as shown in the right panel in Fig. 14.

Hyperbolic systems of conservation laws usually possess more than one solution, so it is necessary to impose some constraints on the discontinuities to find the physically correct solution to the Riemann problem. Following [88, 118], we require that C-waves do

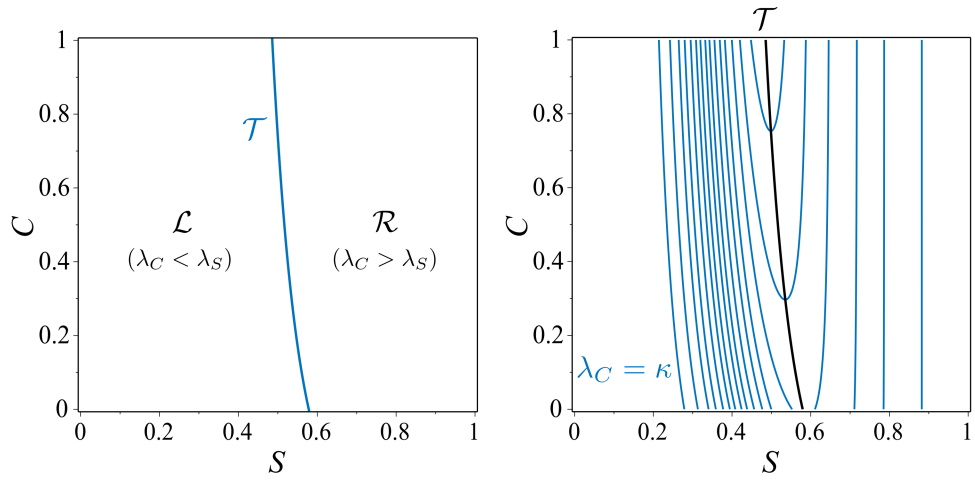

Figure 14 – Phase plane S-C division. The left panel shows sets $\mathcal{L}$ and $\mathcal{R}$, located to the left and the right of the transition curve $\mathcal{T}$, respectively. The right panel shows $\lambda_C = \kappa$ curves (blue lines) for several values of κ, where the outer curves λ_C are for smaller κ. As κ increases, the parabolas start to reach their minimum point inside the domain $I \times I$.

not cross the transition curve $\mathcal{T}$ in the phase plane S-C. That is, C-waves can connect two states only if both states are in $\mathcal{L}$ or both are in $\mathcal{R}$. For S-waves, it is necessary to satisfy the Oleinik entropy condition [70]:

$$\frac{f(U) - f(U^-)}{S - S^-} \geq \sigma \geq \frac{f(U^+) - f(U)}{S^+ - S}, \tag{3.38}$$

for all U between U^- and U^+. This criterion can be applied because the S-waves keep C constant. When S tends to S^- or S^+ in Eq. (3.38), we obtain that the classic Lax's entropy condition (see Section 2.1) is also satisfied

$$\lambda_S(U^+) \leq \sigma \leq \lambda_S(U^-). \tag{3.39}$$

According to [125–127], this entropy criterion is equivalent to the generalized Lax entropy condition proposed by Keyfitz and Kranzer [128].

When the solution is composed of two or more waves, we need to verify an additional condition. We say that the wave sequence $U^- \xrightarrow{S} U_M \xrightarrow{C} U^+$ is compatible (that is, can be combined to solve the Riemann problem with left state U^- and right state U^+) if and only if $v_f^S \leq v_i^C$ [88]. In the same way, $U^- \xrightarrow{C} U_M \xrightarrow{S} U^+$ is compatible if and only if $v_f^C \leq v_i^S$.

3.2.2 Riemann problem solution

From now on, the states U_L and U_R represent the injection and initial reservoir conditions of the Riemann problem, respectively. A wave sequence $U_L \xrightarrow{S} U_M \xrightarrow{C} U_R$ is compatible if and only if $v_f^S \leq v_i^C$ [88]. That is, $U_L \xrightarrow{S} U_M$ and $U_M \xrightarrow{C} U_R$ (U_M is the right state of the S-wave and the left state of the C-wave) can be combined to solve

the Riemann problem. In the same way, $U_L \xrightarrow{C} U_M \xrightarrow{S} U_R$ is compatible if and only if $v_f^C \leq v_i^S$.

For a given state $U = (S, C)$, we define $S^k = S^k(U)$ satisfying $\lambda_C(U) = \lambda_C(S^k, C)$. Geometrically, $(S^k, f(S^k, C))$ is the intersection between the secant line connecting points $(-a, 0)$ to $(S, f(U))$ and the fractional flow function for fixed C; see the left panel in Fig. 15. The right panel in Fig. 15 shows two special cases when this secant line doesn't cross f in another point: (i) $U \in \mathcal{T}$, then $S^k(U) = \hat{S}$ (as defined in Prop. 3.2), and (ii) S^k does not exist and we define $S^k = +\infty$.

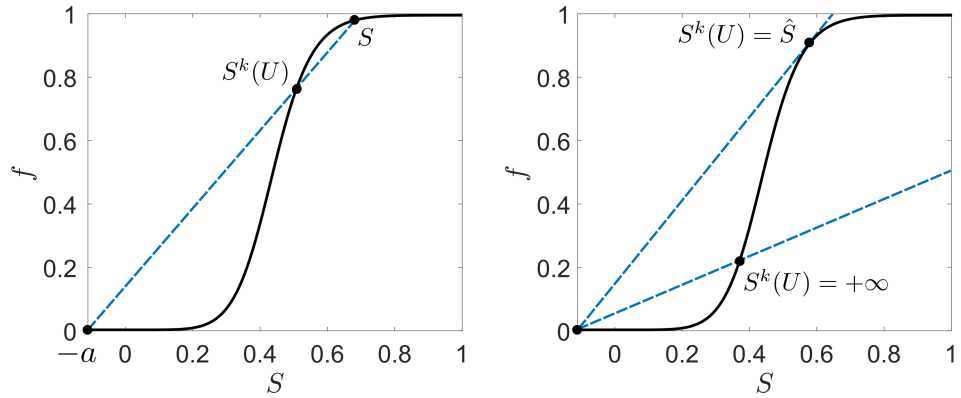

Figure 15 – Geometric representation of $S^k(U)$ for any $U = (S, C)$, where the blue dashed lines represent the secant line connecting points $(-a, 0)$ to $(S, f(U))$. The left panel shows the general case, and the right panel shows the special cases $S^k(U) = \hat{S}$ and $S^k(U) = +\infty$.

The following theorem proves the existence of the Riemann problem solution, presenting necessary and sufficient conditions for a wave sequence connecting the left U_L to the right state U_R to be compatible. A system similar to (3.9)-(3.10) is studied in [88]. Since this work models another application, there is a difference in the properties of the fractional flow function f (similar to [91]); see Proposition 3.1. Using the change of variable $\overline{C} = 1 - C$, we obtain the same properties of [88], as $f(S, \overline{C})$ is a decreasing function of $\overline{C}$. Therefore, the results proved in [88] and Theorem 3.3 are equivalents. However, there are some differences in the geometric analysis due to the presence of constant a in our model and the introduction of the notation $S^k(U)$. For clarity, we present the proof here.

Theorem 3.3. *For arbitrary states $U_L, U_R \in I \times I$, with $U_L \neq U_R$:*

(i) The wave sequence

$$U_L \xrightarrow{C} U_M \xrightarrow{S} U_R, \tag{3.40}$$

is compatible, if and only if, $U_M \in \mathcal{L} \cup \mathcal{T}$ and $0 \leq S_R \leq S^k(U_M)$.

(ii) The wave sequence

$$U_L \xrightarrow{S} U_M \xrightarrow{C} U_R, \tag{3.41}$$

is compatible, if and only if, $U_M \in \mathcal{R} \cup \mathcal{T}$ and $S^k(U_M) \leq S_L \leq 1$.

(iii) If $C_L < C_R$, the wave sequence

$$U_L \xrightarrow{S_1} U_1 \xrightarrow{C} U_2 \xrightarrow{S_2} U_R, \tag{3.42}$$

is compatible, if and only if the following conditions are satisfied: $U_L \in \mathcal{R}$, $U_1 \in \mathcal{T}$, $U_2 \in \mathcal{L}$ and $0 \leq S_R \leq S^k(U_2)$.

(iv) If $C_L > C_R$, the wave sequence

$$U_L \xrightarrow{S_1} U_1 \xrightarrow{C} U_2 \xrightarrow{S_2} U_R, \tag{3.43}$$

is compatible, if and only if the following conditions are satisfied: $U_1 \in \mathcal{R}$, $U_2 \in \mathcal{T}$, $U_R \in \mathcal{L}$ and $S^k(U_1) \leq S_L \leq 1$.

Therefore, there is a sequence of one, two, or three compatible S-waves and C-waves that give a solution to the Riemann Problem (3.9)-(3.10) *and* (3.15) *with left state U_L and right state U_R.*

Proof. In this proof, we use that contact waves only connect points of the same side of the transition curve $\mathcal{T}$. Thus, if two states are connected by a contact wave, the value of C changes along the wave. Note that along the wave means along the corresponding curve in the phase plane S-C.

(i) Since the states U_L and U_M are connected by a contact wave, the intermediate state is given by $U_M = (S_M, C_R)$. Let us assume that the sequence is compatible. By definition, $v_f^C \leq v_i^S$, so applying the Lax's entropy condition (3.39) we obtain

$$\lambda_C(U_M) = v_f^C \leq v_i^S \leq \lambda_S(U_M), \tag{3.44}$$

yielding $U_M \in \mathcal{L} \cup \mathcal{T}$. Assuming that, by contradiction, $S_R > S^k(U_M)$, we analyze two cases.

- If the S-wave starts with shock, v_i^S is a shock wave velocity given by $v_i^S = [f(U_R) - f(U_M)]/(S_R - S_M)$. By hypothesis, $S^k(U_M)$ is finite, then $\lambda_C(U_M) = \lambda_C(S^k(U_M), C_R)$. Applying Oleinik's entropy condition (3.38) for $(S^k(U_M), C_R)$:

$$\lambda_C(U_M) = \frac{f(S^k(U_M), C_R) - f(U_M)}{S^k(U_M) - S_M} \geq \frac{f(U_R) - f(U_M)}{S_R - S_M}, \tag{3.45}$$

  which contradicts the wave sequence compatibility $v_f^C \leq v_i^S$; see Fig. 16. Note that $S_R < S^k(U_M)$ is always true if $S^k(U_M) = +\infty$.

- If the S-wave starts with rarefaction, v_i^S is a rarefaction wave velocity. Once $U_M \in \mathcal{L} \cup \mathcal{T}$, $S_M < \hat{S}(C_R)$. If $S_M > S^I$, where S^I is the inflection point of $f(S, C_R)$, the secant line connecting $(S_M, f(U_M))$ to $(S_R, f(U_R))$ is below

$f(S, C_R)$ graph starting at $(S_M, f(U_M))$ and ending at $(S_R, f(U_R))$. By Oleinik's entropy condition (3.38), this is a shock wave, which contradicts the initial hypothesis. If $S_M < S^I$, then $S^k(U_M) = +\infty$ and, therefore, $S_R < S^k(U_M)$ is always valid.

Conversely, let us suppose $U_M \in \mathcal{L} \cup \mathcal{T}$ and $0 \leq S_R \leq S^k(U_M)$. The first one yields $\lambda_S(U_M) \geq \lambda_C(U_M)$. If the S-wave starts with rarefaction, then $v_i^S = \lambda_S(U_M)$. Once C-waves keep same velocity for all intermediary states, $v_f^C = \lambda_C(U_M)$ and we obtain

$$v_i^S = \lambda_S(U_M) \geq \lambda_C(U_M) = v_f^C, \tag{3.46}$$

that is, the wave sequence is compatible. If the S-wave starts with shock, $0 \leq S_R \leq S^k(U_M)$ implies that if $S^k(U_M)$ exists and

$$v_f^C = \frac{f(S^k(U_M), C_R) - f(U_M)}{S^k(U_M) - S_M} \leq \frac{f(U_R) - f(U_M)}{S_R - S_M} = v_i^S, \tag{3.47}$$

then the wave sequence is compatible. The remainder case $S^k(U_M) = +\infty$ also provides compatible wave sequences.

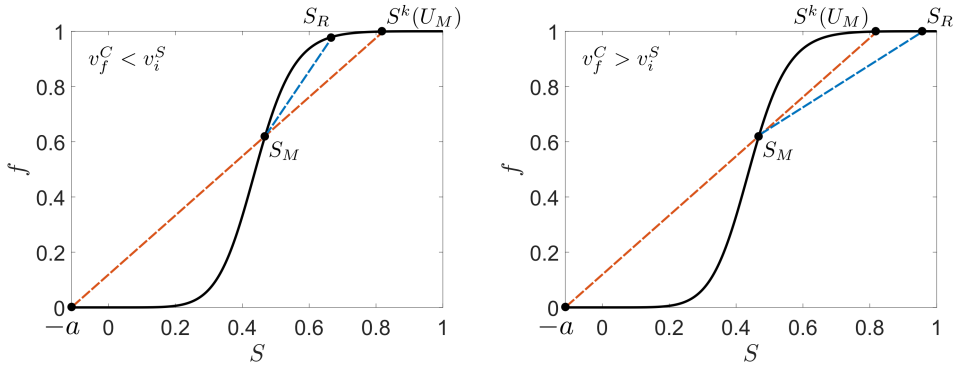

Figure 16 – Geometric representation of v_f^C (slope of the red dashed line) and v_i^S (slope of the blue dashed line). On the left panel, $0 \leq S_R \leq S^k(U_M)$. On the right panel $S_R > S^k(U_M)$; this case implies $v_f^C > v_i^S$, then the wave sequence is incompatible.

(ii) This case is analogous to the previous one. The states U_M and U_R are connected by a contact wave, so the intermediate state is $U_M = (S_M, C_L)$. If v_f^S is a shock wave velocity, by a similar analysis to the item *(i)*, the inequality

$$v_f^S = \frac{f(U_M) - f(U_L)}{S_M - S_L} \leq \frac{f(U_M) - f(S^k(U_M), C_L)}{S_M - S^k(U_M)} = v_i^C, \tag{3.48}$$

is satisfied if and only if $U_M \in \mathcal{R} \cup \mathcal{T}$, and $S^k(U_M) \leq S_L \leq 1$. Note that $S^k(U_M)$ always exists, since $U_M \in \mathcal{R} \cup \mathcal{T}$.

If v_f^S is a rarefaction wave velocity, $v_f^S = \lambda_S(U_M)$. Once $v_i^C = \lambda_C(U_M)$, $v_f^S \leq v_i^C$ is satisfied if and only if $\lambda_S(U_M) \leq \lambda_C(U_M)$; that is, $U_M \in \mathcal{R} \cup \mathcal{T}$. The condition $0 \leq S_R \leq S^k(U_M)$ is satisfied by Oleinik's entropy condition (3.38).

(iii) From item *(i)*, for $U_1 \xrightarrow{C} U_2 \xrightarrow{S_2} U_R$ to be compatible, it is necessary and sufficient that $U_2 \in \mathcal{L} \cup \mathcal{T}$ and $0 \leq S_R \leq S^k(U_2)$. From item *(ii)*, for $U_L \xrightarrow{S_1} U_1 \xrightarrow{C} U_2$ to be compatible, it is necessary and sufficient that $U_1 \in \mathcal{R} \cup \mathcal{T}$ and $S^k(U_1) \leq S_L \leq 1$. Furthermore, the intermediate states are $U_1 = (S_1, C_L)$ and $U_2 = (S_2, C_R)$.

Geometrically, as $v_i^C = v_f^C$, the same secant line contains $(-a, 0)$, $(S_1, f(U_1))$, and $(S_2, f(U_2))$; see the left panel in Fig. 17. Assuming $U_2 \in \mathcal{T}$, the line connecting $(-a, 0)$ to $(S_2, f(U_2))$ does not cross $f(S, C_L)$, and there is no U_1 such that $\lambda_C(U_1) = \lambda_C(U_2)$; see the right panel in Fig. 17. Therefore, for the sequence to be compatible, it is necessary that $U_2 \in \mathcal{L}$. Since it is only possible to connect two states through a contact wave when they are on the same side of the transition curve, $U_1 \in \mathcal{T}$. As a result, $S^k(U_1) = \hat{S}(C_L) \leq S_L$ and $U_L \in \mathcal{R} \cup \mathcal{T}$. Nevertheless, if $U_L \in \mathcal{T}$ then $S^k(U_1) = S_L$. This case was treated in item *(i)*, so we suppose that $S_1 \neq S_L$. Therefore, $U_L \in \mathcal{R}$.

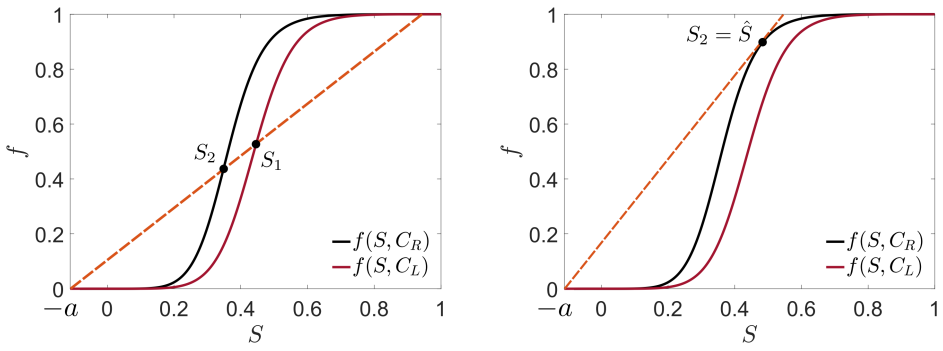

Figure 17 – Geometric representation of $v_i^C = v_f^C$ (slope of the red dashed lines). The left panel shows the general case, and the right panel shows the case $U_2 \in \mathcal{T}$.

(iv) Analogously to the previous one, items *(i)* and *(ii)* provides that for $U_1 \xrightarrow{C} U_2 \xrightarrow{S_2} U_R$ and $U_L \xrightarrow{S_1} U_1 \xrightarrow{C} U_2$ to be compatible, it is necessary and sufficient that $U_2 \in \mathcal{L} \cup \mathcal{T}$, $U_1 \in \mathcal{R} \cup \mathcal{T}$, $0 \leq S_R \leq S^k(U_2)$, and $S^k(U_1) \leq S_L \leq 1$.

If $U_1 \in \mathcal{T}$ there is no exist a secant line connecting both fractional flow functions. Thus, $U_1 \in \mathcal{R}$ and $U_2 \in \mathcal{T}$, because it is the only point that satisfies $\lambda_C U_1 = \lambda_C U_2$. Moreover, it should be noticed that $0 < S_R < S^K(U_2) < \hat{S}(C_R)$; therefore, $U_R \in \mathcal{L}$.

□

3.2.3 Classification of the phase plane S-C

Based on Theorem 3.3, we classify the phase plane S-C according to the Riemann problem solution. Given a state $V \in I \times I$, we define the set of all states $U \in I \times I$ with the same λ_C as V:

$$\Gamma(V) = \{U \in I \times I \mid \lambda_C(U) = \lambda_C(V)\}. \tag{3.49}$$

Once $\lambda_C = f(S,C)/(S+a)$ is a smooth function, $\Gamma(V)$ defines a curve. Thus, for any point $U_{\mathcal{T}} \in \mathcal{T}$ the phase plane can be divided into three regions:

$$R_1 = \{U \in I \times I \mid \lambda_C(U) \geq \lambda_C(U_{\mathcal{T}})\} \cup \{U \in \mathcal{L} \mid C \geq C_{\mathcal{T}}\}, \tag{3.50}$$

$$R_2 = \{U \in \mathcal{L} \cup \mathcal{T} \mid C \leq C_{\mathcal{T}}\}, \tag{3.51}$$

$$R_3 = \{U \in \mathcal{R} \cup \mathcal{T} \mid \lambda_C(U) \leq \lambda_C(U_{\mathcal{T}})\}, \tag{3.52}$$

as shown in Fig. 18. Note that the regions share internal boundaries, so there are intersections between R_1, R_2, and R_3.

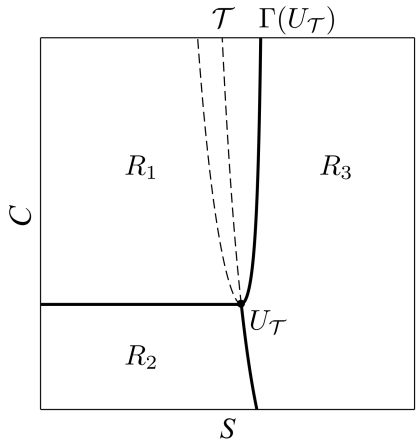

Figure 18 – Phase plane S-C division into regions R_1, R_2, and R_3 for some $U_{\mathcal{T}}$.

For a fixed left state $U_L = (S_L, C_L)$, we define the state $U_{\mathcal{T}}$ as $U_{\mathcal{T}_1}$, $U_{\mathcal{T}_2}$ or $U_{\mathcal{T}_3}$, according to U_L location:

- If $U_L \in \mathcal{L}$, we define
$$U_{\mathcal{T}_1} = \mathcal{T} \cap \Gamma(U_L), \tag{3.53}$$
which exists and is unique if $\Gamma(U_L)$ reaches the minimum point inside $I \times I$. Otherwise, we take $U_{\mathcal{T}_1} = \{U \in \Gamma(U_L) \cap \mathcal{R} \mid C = 0\}$.
- If $U_L \in \mathcal{T}$, it is not necessary to define a new point, and $U_{\mathcal{T}_2} = U_L$.
- If $U_L \in \mathcal{R}$, we define
$$U_{\mathcal{T}_3} = \mathcal{T} \cap \{U \in \Omega \mid C = C_L\}, \tag{3.54}$$
which always exists and is unique.

Remark 3.2. *The points $U_{\mathcal{T}_1}$, $U_{\mathcal{T}_2}$, and $U_{\mathcal{T}_3}$ may not define three regions but two or just a single region. This section considers the general case (see Fig. 18), as the solution of particular cases can be easily obtained by simplifying the general solution.*

Figure 19 summarizes the solution in the phase plane S-C for a fixed left state U_L. In Fig. 19(a), $U_L \in \mathcal{L}$, and the colors represent the solution type in that region (or

curve) if the right state U_R is located there. Cases $U_L \in \mathcal{T}$ and $U_L \in \mathcal{R}$ are shown in Fig. 19(b) and Fig. 19(c), respectively. Fig. 19(d) presents these types of solutions; note that we introduce the notation CS-wave sequence, SC-wave sequence, and SCS-wave sequence for solutions composed of two or more C-waves and S-waves. Our next step is to describe each solution type and determine the intermediate states to obtain compatible wave sequences, following the conditions presented in Theorem 3.3.

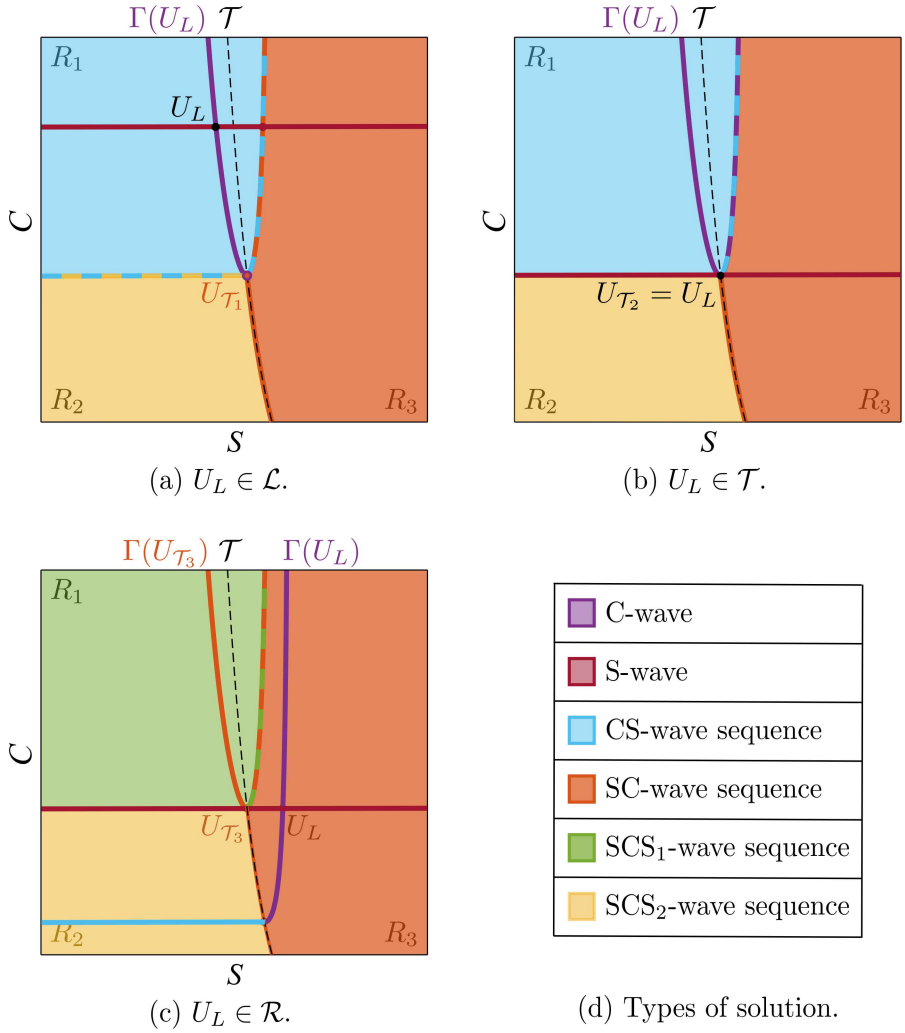

(a) $U_L \in \mathcal{L}$. (b) $U_L \in \mathcal{T}$.

(c) $U_L \in \mathcal{R}$. (d) Types of solution.

Figure 19 – Schematic representation of the solution in the phase plane S-C. The left state U_L is fixed, and the colors represent the solution type in that region (or curve) if the right state U_R is located there. The two-color dashed lines represent the intersection between two types of solutions.

1. <u>C-wave:</u> $U_L \xrightarrow{C} U_R$

   This type of solution is a contact connecting U_L to U_R and is valid when

   - $U_L \in \mathcal{L}$ and $U_R \in \Gamma(U_L) \cap (\mathcal{L} \cup \mathcal{T})$;
   - $U_L \in \mathcal{T}$ and $U_R \in \Gamma(U_L)$;

- $U_L \in \mathcal{R}$ and $U_R \in \Gamma(U_L) \cap (\mathcal{R} \cup \mathcal{T})$.

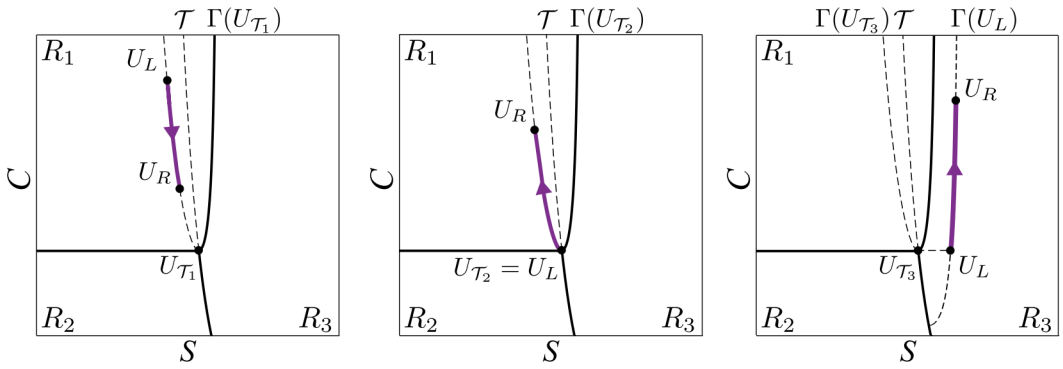

Figure 20 – Schematic representation of a C-wave sequence in the phase plane S-C if $U_L \in \mathcal{L}$ (left panel), $U_L \in \mathcal{T}$ (central panel), and $U_L \in \mathcal{R}$ (right panel).

2. S-wave: $U_L \xrightarrow{S} U_R$

   This type of solution is a shock, a rarefaction, or a combination of these waves connecting U_L to U_R. It is valid when $C_L = C_R$.

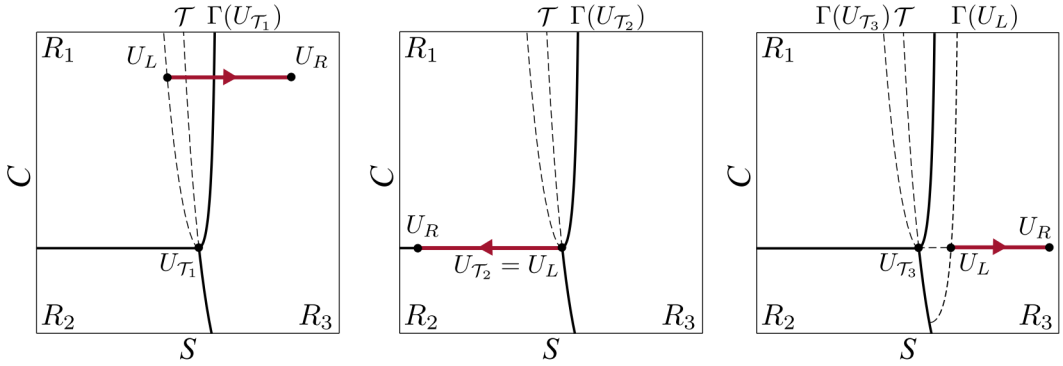

Figure 21 – Schematic representation of an S-wave sequence in the phase plane S-C if $U_L \in \mathcal{L}$ (left panel), $U_L \in \mathcal{T}$ (central panel), and $U_L \in \mathcal{R}$ (right panel).

3. CS-wave sequence: $U_L \xrightarrow{C} U_M \xrightarrow{S} U_R$

   This type of solution is composed of a C-wave connecting U_L to an intermediate state U_M and an S-wave connecting U_M to U_R. From item *(i)* of Theorem 3.3, U_M is given by

$$U_M = \Gamma(U_L) \cap \{U \in \mathcal{L} \cup \mathcal{T} \mid C = C_R\}, \tag{3.55}$$

   as shown in Fig. 22.

   The solution type is a CS-wave sequence when

   - $U_L \in \mathcal{L} \cup \mathcal{T}$ and $U_R \in R_1$, except in particular cases when the solution type is a C-wave or an S-wave.
   - $U_L \in \mathcal{R}$ and $U_M = \Gamma(U_L) \cap \mathcal{T}$. That is, U_R is such that U_M defined by Eq. (3.55) is on the transition curve $\mathcal{T}$.

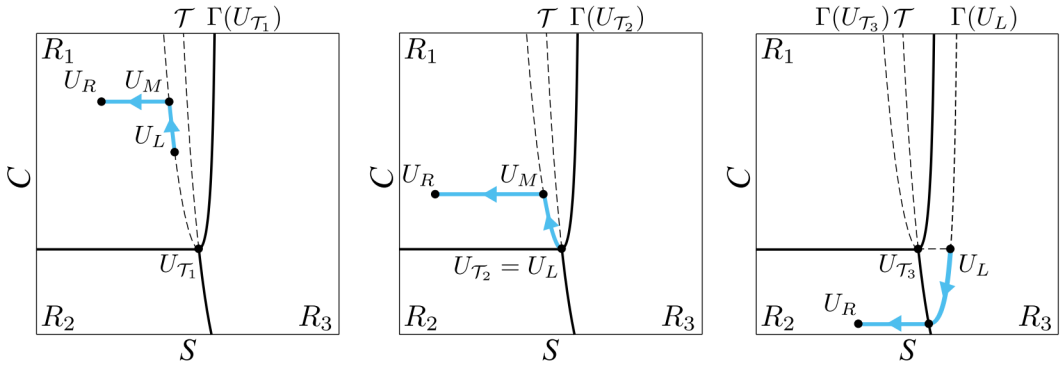

Figure 22 – Schematic representation of a CS-wave sequence in the phase plane S-C if $U_L \in \mathcal{L}$ (left panel), $U_L \in \mathcal{T}$ (central panel), and $U_L \in \mathcal{R}$ (right panel).

4. SC-wave sequence: $U_L \xrightarrow{S} U_M \xrightarrow{C} U_R$

   This type of solution is composed of an S-wave connecting U_L to an intermediate state U_M and a C-wave connecting U_M to U_R. From item *(ii)* of Theorem 3.3, U_M is given by

   $$U_M = \Gamma(U_R) \cap \{U \in \mathcal{R} \mid C = C_L\}\,, \tag{3.56}$$

   as shown in Fig. 23. The solution type is an SC-wave sequence when

   - $U_L \in \mathcal{L}$ and $U_R \in R_3$, except in particular cases when the solution type is an S-wave.
   - $U_L \in \mathcal{R} \cup \mathcal{T}$ and $U_R \in R_3$, except in particular cases when the solution type is a C-wave or an S-wave.

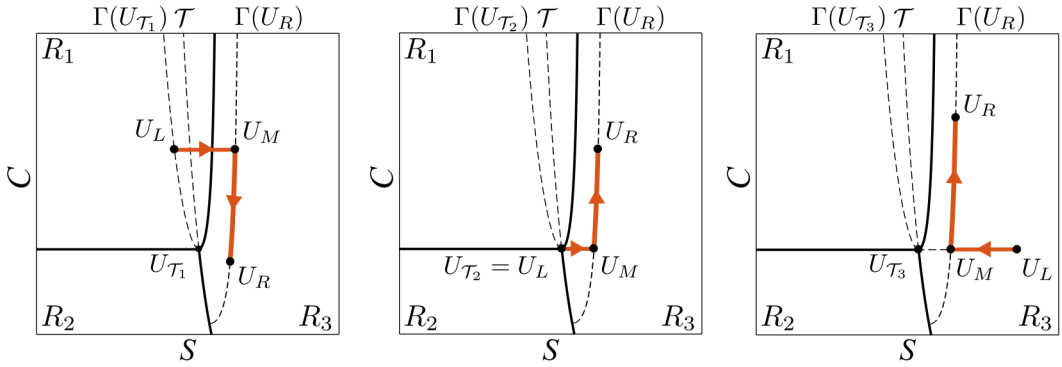

Figure 23 – Schematic representation of an SC-wave sequence in the phase plane S-C if $U_L \in \mathcal{L}$ (left panel), $U_L \in \mathcal{T}$ (central panel), and $U_L \in \mathcal{R}$ (right panel).

5. SCS_1-wave sequence: $U_L \xrightarrow{S_1} U_1 \xrightarrow{C} U_2 \xrightarrow{S_2} U_R$, with $C_L < C_R$

   This type of solution is composed of an S-wave connecting U_L to an intermediate state U_1, a C-wave connecting U_1 to another intermediate state U_2, and an S-wave connecting U_2 to U_R. It is valid when $C_L < C_R$; from item *(iii)* of Theorem 3.3, U_1

and U_2 are given by

$$U_1 = U_{\mathcal{T}_2}, \tag{3.57}$$
$$U_2 = \Gamma(U_1) \cap \{U \in \mathcal{L} \mid C = C_R\}, \tag{3.58}$$

as shown in Fig. 24. The solution type is an SCS_1-wave sequence when $U_L \in \mathcal{R}$ and $U_R \in R_1$, except in particular cases when the solution type is an S-wave or an SC-wave sequence.

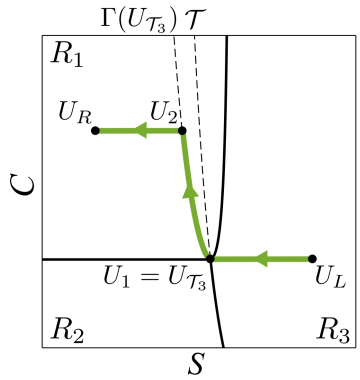

Figure 24 – Schematic representation of an SCS_1-wave sequence in the phase plane S-C.

6. SCS_2-wave sequence: $U_L \xrightarrow{S_1} U_1 \xrightarrow{C} U_2 \xrightarrow{S_2} U_R$, with $C_L > C_R$

   This type of solution is similar to SCS_1-wave sequence, but $C_L > C_R$ in this case. It is valid when $C_L > C_R$; from item *(iv)* of Theorem 3.3, U_1 and U_2 are given by

$$U_2 = \mathcal{T} \cap \{U \in I \times I \mid C = C_R\}, \tag{3.59}$$
$$U_1 = \Gamma(U_2) \cap \{U \in \mathcal{R} \mid C = C_L\}, \tag{3.60}$$

   as shown in Fig. 25. The solution type is an SCS_2-wave sequence when

   - $U_L \in \mathcal{L}$ and $U_R \in R_2 \cap \mathcal{L}$.
   - $U_L \in \mathcal{T}$ and $U_R \in R_2 \cap \mathcal{L}$, except in particular cases when the solution type is an S-wave.
   - $U_L \in \mathcal{R}$ and $U_R \in R_2 \cap \mathcal{L}$, except in particular cases when the solution type is an S-wave or a CS-wave sequence.

Remark 3.3. *There are cases with two solutions at the boundaries between R_1, R_2, or R_3 (represented by the two-color dashed lines in Figs. 19). According to [91, 129, 130], the Riemann problem solution is structurally unstable in these cases, as perturbations in the initial data or the flux function change the structure of the solution. More details about this loss of structural stability are presented in Section 3.6.*

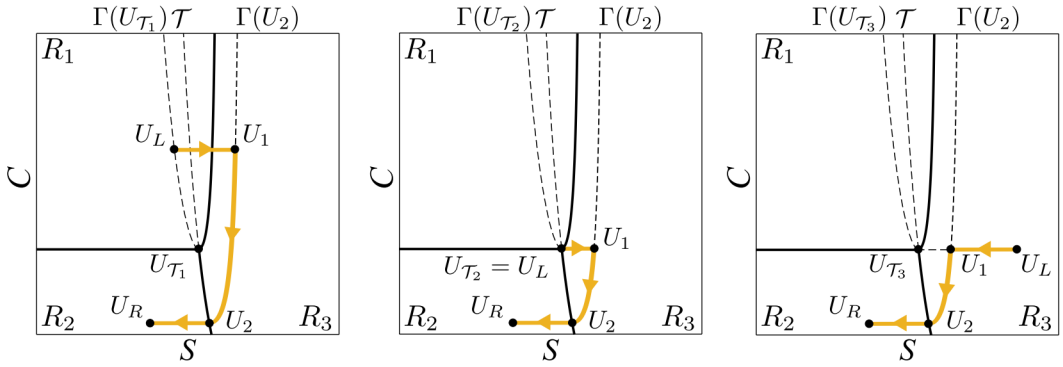

Figure 25 – Schematic representation of an SCS_2-wave sequence in the phase plane S-C if $U_L \in \mathcal{L}$ (left panel), $U_L \in \mathcal{T}$ (central panel), and $U_L \in \mathcal{R}$ (right panel).

3.3 MODEL SETUP AND QUANTITIES OF INTEREST

For practical examples, we follow the core-flood experiment reported in [44], where a surfactant solution and gas are co-injected into Bentheimer sandstone cores with porosity and permeability of about $20 \pm 1\%$ and $2.0 \pm 2\%$, respectively. The core length and diameter are 0.17 m and 0.038 m. The physical parameters used in this work are summarized in Table 2. The results presented in this chapter consider the Riemann problem (3.13)-(3.15) with the original relative permeability model; see Table 3.

Table 2 – Physical parameters used in this work. Source: [44, 92]

Symbol	Parameter	Value
α (Pa·s$^{2/3}$m$^{10/3}$)	Viscosity proportionality const.	$5.8 \cdot 10^{-16}$
φ (−)	Porosity	0.21
k (m^2)	Absolute permeability	$2.5 \cdot 10^{-12}$
μ_g (Pa·s)	Gas viscosity	$1.8 \cdot 10^{-5}$
μ_w (Pa·s)	Water viscosity	$1.0 \cdot 10^{-3}$
d (−)	Power law viscosity exponent	1/3
u_g (m/s)	Gas velocity	$1.471 \cdot 10^{-5}$
u_w (m/s)	Water velocity	$1.446 \cdot 10^{-6}$
S_{wc} (−)	Connate water saturation	0.10
S_{gr} (−)	Residual gas saturation	0
β (m^3)	Mobility parameter	$7.817 \cdot 10^{-10}$
L (m)	Core length	0.17
D (m)	Core diameter	0.038

To quantify the sweep efficiency of the porous medium, we focus on the breakthrough time and cumulative water production, as these are the key parameters for industrial applications [131]. The breakthrough time can be directly obtained by dividing the reservoir length by the corresponding wave velocity. We use the analytical solution and, when necessary, numerical integration to obtain the production over time, as detailed below.

Table 3 – Parameters of the original relative permeability model. Source: [44, 92]

Symbol	Parameter	Value
n_w $(-)$	Corey exponent for water relative perm.	5
n_g $(-)$	Corey exponent for gas relative perm.	3.4
$c_{k_{rg}}$ $(-)$	Gas endpoint relative perm.	1.0
$c_{k_{rw}}$ $(-)$	Water endpoint relative perm.	0.75

It is equivalent to calculating water production over time for the model (3.9)-(3.10) by the inflow rate and integration of water saturation profiles

$$\mathrm{WP}(t) = \int_0^t f(U(0,\tau))d\tau + \int_0^1 S(x,0)dx - \int_0^1 S(x,t)dx, \tag{3.61}$$

or by the outflow rate

$$\mathrm{WP}(t) = \int_0^t f(U(1,\tau))d\tau, \tag{3.62}$$

see [46] for details. Using the second one, we present a scheme of the WP calculations for a CS-wave sequence type solution; the other cases are similar. If the S-wave is a shock:

$$\mathrm{WP}(t) = \begin{cases} f(U_R)t, & \text{if} \quad t \le T_1, \\ f(U_R)T_1 + f(U_M)(t - T_1), & \text{if} \quad T_1 < t \le T_2, \\ f(U_R)T_1 + f(U_M)(T_2 - T_1) & \text{if} \quad t > T_2, \\ \qquad\qquad + f(U_L)(t - T_2), & \end{cases} \tag{3.63}$$

where the intermediate state is $U_M = (S_M, C_R)$, T_1 is the breakthrough time, and T_2 is the time when the contact wave reaches the reservoir's end. If the S-wave is a rarefaction followed by a shock:

$$\mathrm{WP}(t) = \begin{cases} f(U_R)t, & \text{if} \quad t \le T_1, \\ f(U_R)T_1 + \int_{T_1}^t f(S(t), C_R)\, dt, & \text{if} \quad T_1 < t \le T_2, \\ f(U_R)T_1 + \int_{T_1}^{T_2} f(S(t), C_R)\, dt + f(U_M)(t - T_2), & \text{if} \quad T_2 < t \le T_3, \\ f(U_R)T_1 + \int_{T_1}^{T_2} f(S(t), C_R)\, dt + f(U_M)(T_3 - T_2) & \text{if} \quad t > T_3, \\ \qquad\qquad + f(U_L)(t - T_3), & \end{cases} \tag{3.64}$$

where T_1 is the breakthrough time, T_2 is when the rarefaction wave passes through the entire reservoir, and T_3 is the time when the contact wave reaches the reservoir's end. Since the water saturation is a function of x/t for rarefaction waves, we numerically solve the differential equation $\partial_S f(S(t), C_R) = 1/t$ to find S at the end of the reservoir for each t. Then, we use numerical integration to calculate WP.

3.4 NUMERICAL VALIDATION

We assume that the solution is a sequence of waves to solve the Riemann problem. Now, we compare the analytical solution with direct numerical simulations to validate this

assumption. We use the *reaction–convection–diffusion equations solver* (RCD) [132], which is a C++ structured package of routines based on the Crank-Nicolson finite difference scheme and Newton's method. For the spatial discretization, were used 10^4 points. The time step adopted was 10^{-5}.

We present two examples. The first is an imbibition case (water saturation in the reservoir is increasing) for injection condition $U_L = (0.8, 0.8)$ and initial reservoir condition $U_R = (0.2, 0.2)$. The solution is an SCS_2-wave sequence; see the left panel in Fig. 26. The right panel shows good agreement between the analytical and numerical solutions. The second example is a drainage case (water saturation in the reservoir is decreasing) for injection condition $U_L = (0.2, 0.2)$ and initial reservoir condition $U_R = (0.8, 0.8)$. The solution is a CS-wave sequence; see the left panel in Fig. 27. The right panel shows good agreement between the analytical and numerical solutions.

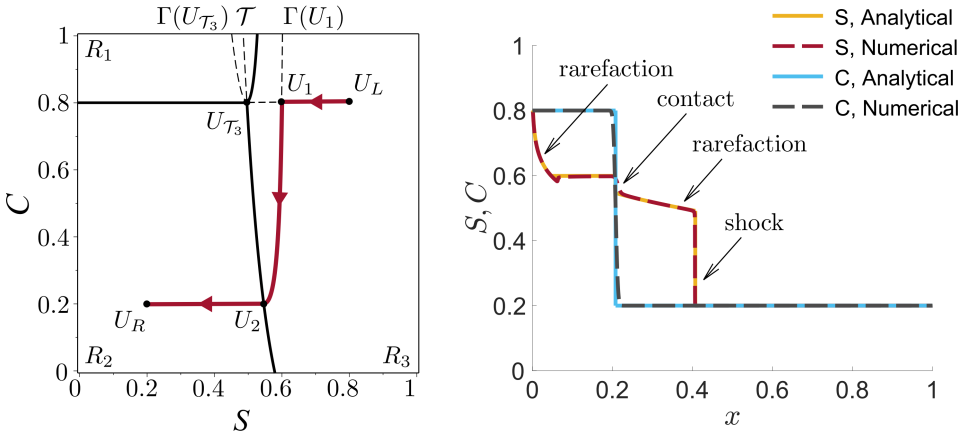

Figure 26 – The solution (SCS_2-wave sequence) composed of a rarefaction connecting U_L to U_1, a contact connecting U_1 to U_2, and a rarefaction followed by a shock connecting U_2 to U_R for $U_L = (0.8, 0.8)$ and $U_R = (0.2, 0.2)$. The left panel shows the phase plane S-C, and the right panel compares the analytical and numerical solution profiles at dimensionless time $T = 0.15$.

To verify the convergence of the numerical simulations we calculate the relative error between the numerical solutions $\mathcal{U}$ obtained for meshes of $N/2$ and N points (with their corresponding time steps) using l_2 Euclidean norm as $\sqrt{\sum (\mathcal{U}_{N/2} - \mathcal{U}_N)^2 / \sum (\mathcal{U}_{N/2})^2}$.

Table 4 summarizes the adopted discretizations and their respective relative errors considering the drainage example (injection and initial conditions $U_L = (0.2, 0.2)$ and $U_R = (0.8, 0.8)$) at time $T = 0.15$ (before the breakthrough). Figure 28 presents the relative error for each mesh size. Note that, when machine precision is reached for each difference $\mathcal{U}_{N/2} - \mathcal{U}_N$, the relative error calculated by Euclidean norm above stabilizes close to 10^{-5}.

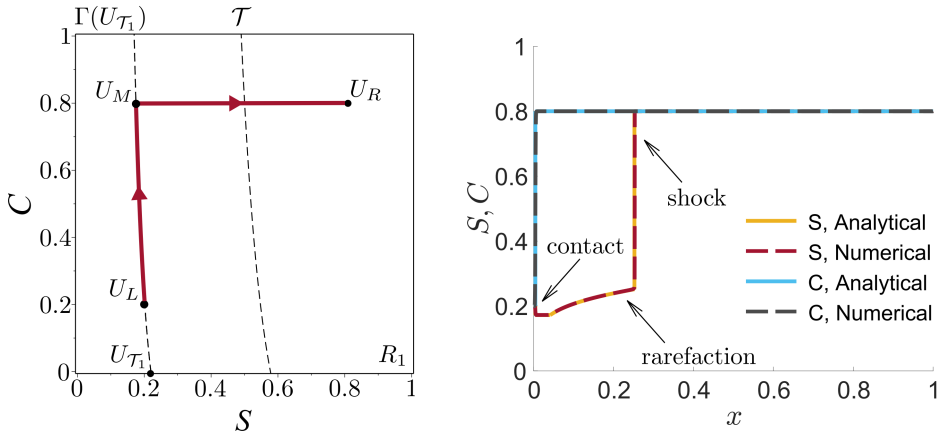

Figure 27 – The solution (CS-wave sequence) composed of a C-wave connecting U_L to U_M and a rarefaction followed by a shock connecting U_M to U_R for $U_L = (0.2, 0.2)$ and $U_R = (0.8, 0.8)$. The left panel shows the phase plane S-C, and the right panel compares the analytical and numerical solution profiles at dimensionless time $T = 0.15$.

Table 4 – Relative errors for different mesh refinement.

Mesh points	Time step	Relative error (%)
$2.5 \cdot 10^3$	$4.0 \cdot 10^{-5}$	$1.4 \cdot 10^{-4}$
$5.0 \cdot 10^3$	$2.0 \cdot 10^{-5}$	$6.4 \cdot 10^{-5}$
$1.0 \cdot 10^4$	$1.0 \cdot 10^{-5}$	$9.3 \cdot 10^{-6}$
$2.0 \cdot 10^4$	$5.0 \cdot 10^{-6}$	$8.0 \cdot 10^{-6}$

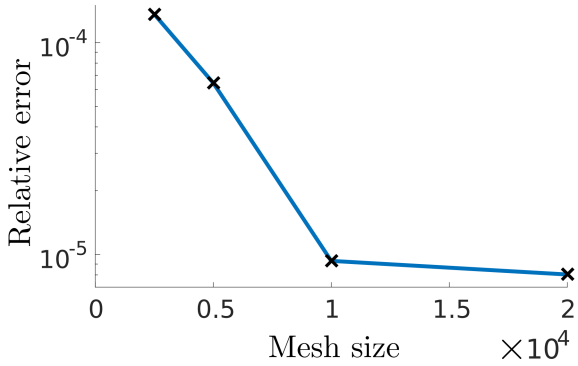

Figure 28 – Numerical simulations convergence (order 0.95, calculated before the machine precision is reached) for spatial and temporal discretizations shown in Table 4.

3.5 EFFECT OF NANOPARTICLES ON FOAM FLOW

We aim to investigate the effect of nanoparticles on foam flow in porous media using the proposed model and its respective analytical solution. Inspired by the FAWAG technique, we consider the cyclical injection of water, chemical slug (water with surfactant and nanoparticles), and gas into the reservoir originally filled with oil. Foam is formed when the gas is mixed with the previously injected surfactant. The idea is that the nanoparticles added to the chemical slug improve foam stability, enhancing sweep efficiency. In this

scenario, we study the drainage procedure (mainly gas injection) after a slug of water with surfactant and nanoparticles, as shown in Fig. 29. Thus, this section focuses on the region where the gas bank (low S_L, $C_L = 0$) meets the slug (high S_R, $C_R \geq 0$).

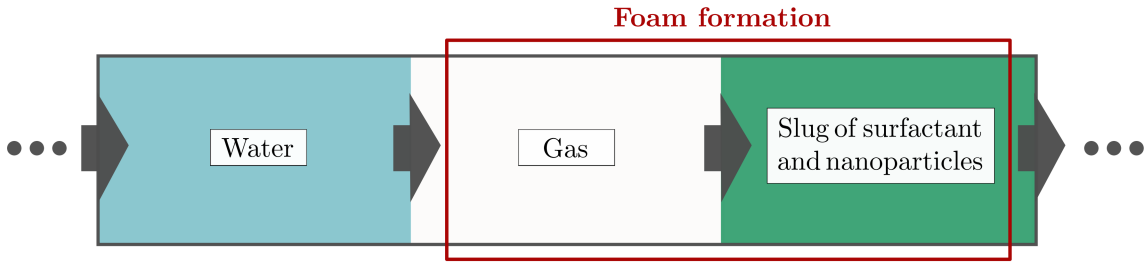

Figure 29 – llustration of the drainage procedure (mainly gas injection) after a slug of water with surfactant and nanoparticles, inspired by the cyclical injections of the FAWAG technique. This work focuses on the region where the foam formation occurs (between the gas bank and the slug).

Remark 3.4. *To compare the cases without and with nanoparticles, the injection conditions for both cases are* $(S_L^1, 0)$ *and* (S_L^2, C_L)*. Matching the injection water saturations yields* $S_L^1 = S_L^2$ *and equating the injection rates* ($Q_{inj}^1 = uf(S_L^1, 0)$ *and* $Q_{inj}^2 = uf(S_L^2, C_L)$) *results in* $f(S_L^2, C_L) = f(S_L^1, 0)$*, thus this comparison needs to consider* $C_L = 0$*. We study the impact of nanoparticle concentration in solutions by studying various initial reservoir conditions below.*

Next, we present two cases: the first one is more related to an industrial application, showing how nanoparticles improve WP. The second one investigated the effect of nanoparticles in the water-gas co-injection (which is a widely used laboratory experiment technique [22, 24, 94]). The latter includes the counterintuitive example when adding nanoparticles does not improve WP. Presented cases follow core-flood experiments [44] with parameters given in Tables 2 and 3.

3.5.1 Sweep efficiency during pure gas injection

We study Riemann problem (3.1)-(3.2) with injection condition $U_L = (0, 0)$ varying the initial condition $U_R = (1, C_R)$. The solution is a CS-wave sequence, where the S-wave is a rarefaction followed by a shock. Note that the contact velocity is 0 since $S_L = 0$ (see Eq.(2.11)). The case $C_R = 0$ represents the foam flow without nanoparticles, and MRF > 1 is constant; see Eq. (3.4).

The left panel in Fig. 30 presents the WP curve for nanoparticle concentrations 0.0%, 0.2%, 0.4%, 0.6%, 0.8%, and 1.0%. To show the good agreement between the analytical and numerical results, we plotted the production curves corresponding to the saturation profiles obtained numerically for $C_{np} = 0.0\%$ and $C_{np} = 1.0\%$. Comparing these two concentrations, the time for producing approximately 32 mL of water decreases

from 61 to 26 min with the addition of nanoparticles. Notice that the chosen control amount of water (32 mL) is consistent with the core-flood experiment reported in [44]. The breakthrough time (min), as a function of the nanoparticle concentration, can be approximated by a quadratic polynomial:

$$T_{bt}(C) = -1.64C^2 + 3.68C + 24.85. \tag{3.65}$$

In the same way, for the production curve (mL) at $t = 60$ min, we obtain

$$\mathrm{WP}_{\mathrm{t=60}}(C) = -1.62C^2 + 3.67C + 32.03, \tag{3.66}$$

as shown in the right panel in Fig. 30. Therefore, the effect of nanoparticles on water production and breakthrough time is less pronounced for high nanoparticle concentration. These results corroborate with the model in Eq. (3.7), see Fig. 12.

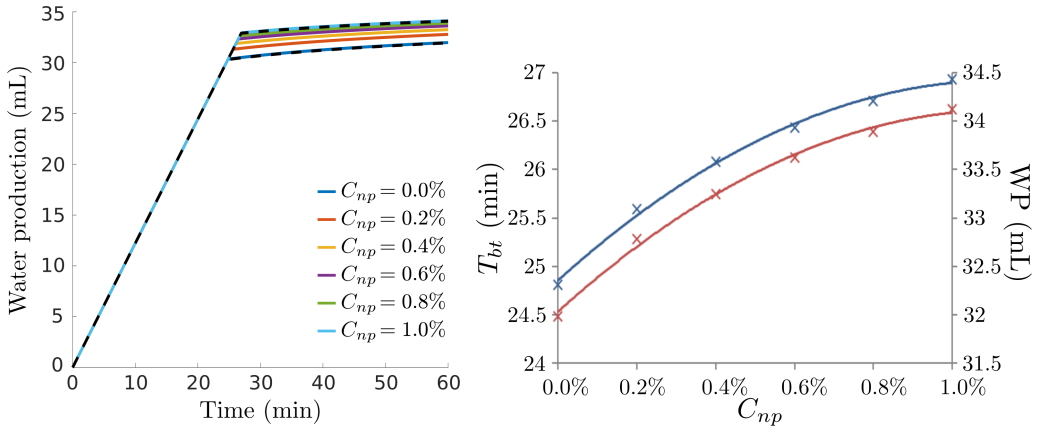

Figure 30 – Effect of nanoparticle concentration on foam flow during gas injection. The left panel shows the production curve over time (continuous lines correspond to analytical solutions and black dashed lines correspond to numerical simulations). The right panel shows the breakthrough time (blue line) and the production at $t = 60$ min (red line). Crossmarks represent the analytical solution and solid lines correspond to Eqs. (3.65) and (3.66).

3.5.2 Sweep efficiency during water-gas co-injection

We study Riemann problem (3.1)-(3.2) with the injection condition $U_L = (S_L, 0)$ and the initial condition $U_R = (S_R, C_R)$, where $S_L \in [0, 0.5]$ and $S_R \in [0.5, 1]$. When $C_R > 0$, the solution can be a CS-wave sequence or an SC-wave sequence. When $C_R = 0$, the solution is always an S-wave.

For the SC-wave sequence, the addition of nanoparticles reduces the breakthrough time and its effect on the sweep efficiency is negligible regardless of the considered concentration. Figure 31 presents an example where the WP curve for $U_L = (0.49, 0)$ and $U_R = (0.85, 1)$ is similar when compared to the one corresponding to the foam flow without nanoparticles ($U_R = (0.85, 0)$). Note that the water saturation of the intermediate

state is very close to the initial water saturation of the reservoir, then the water saturation profile practically does not change with the nanoparticle concentration; see the left panel in Fig. 32. Furthermore, as the contact velocity is greater than the shock velocity, the nanoparticles are present only in the region with high water saturation (i.e., low gas/foam fraction); see the right panel Fig. 32.

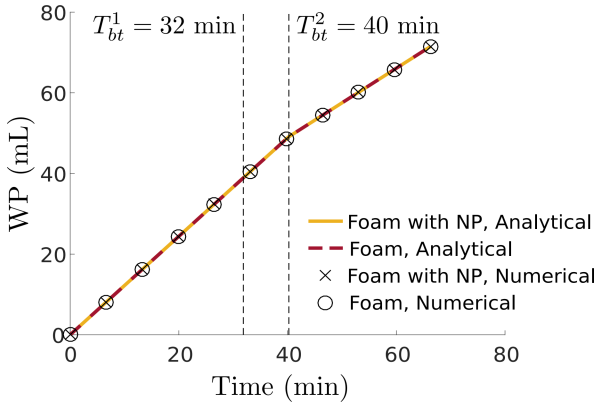

Figure 31 – The water production over time with ($U_R = (0.85, 1)$) and without ($U_R = (0.85, 0)$) nanoparticles (NP) for the same injection condition $U_L = (0.49, 0)$. The addition of nanoparticles decreases the breakthrough time ($T_{bt}^1 < T_{bt}^2$), but there is no significant slope change for the WP curve at T_{bt}^1.

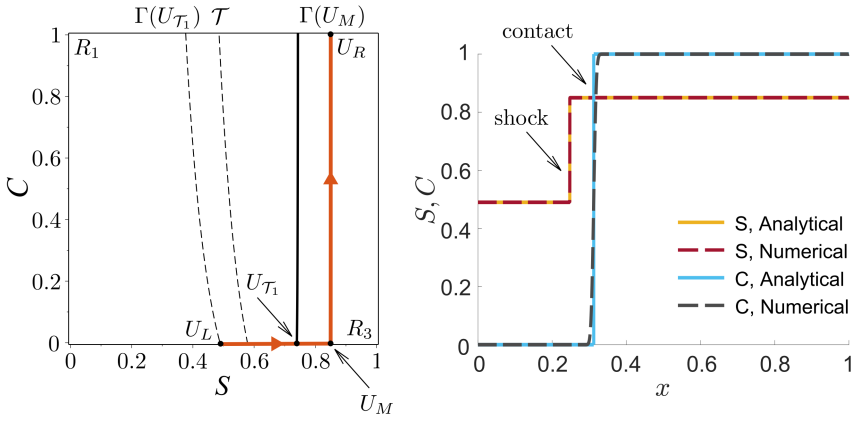

Figure 32 – The solution (SC-wave sequence) composed of a shock connecting U_L to U_M and a contact connecting U_M to U_R for $U_L = (0.49, 0)$ and $U_R = (0.85, 1)$. The left panel shows the phase plane S-C, and the right panel compares the analytical and numerical solution profiles at dimensionless time $T = 0.3$. For this example, $U_M = (0.8497, 0)$.

For the CS-wave sequence, we observe the sweep efficiency improvement when in the presence of nanoparticles for short times. Figure 33 presents an example of water production with ($U_R = (0.5, 1)$) and without ($U_R = (0.5, 0)$) nanoparticles for the same injection condition $U_L = (0.2, 0)$. This effect can be better observed by analyzing the water outflow (see Fig. 34). After the breakthrough, the rate of outflow with nanoparticles is lower than without nanoparticles as the total WP tends to be equal for large times, see Fig. 33.

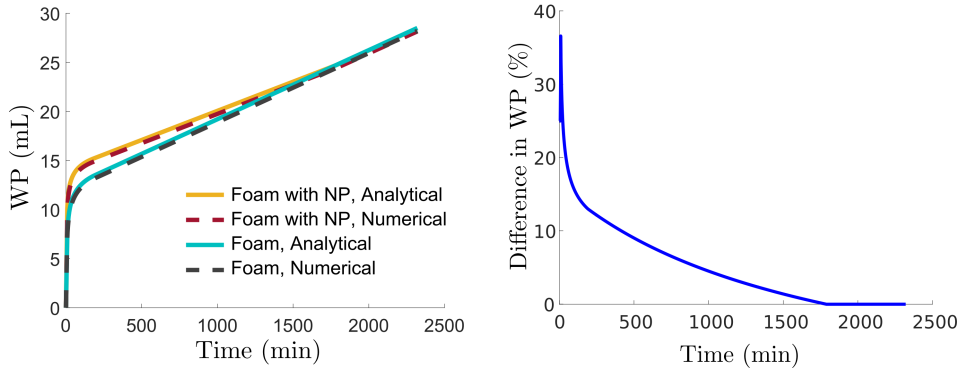

Figure 33 – The water production over time with ($U_R = (0.5, 1)$) and without ($U_R = (0.5, 0)$) nanoparticles for the same injection condition $U_L = (0.2, 0)$. The left panel shows WP and the right panel shows the difference in WP due to the addition of nanoparticles.

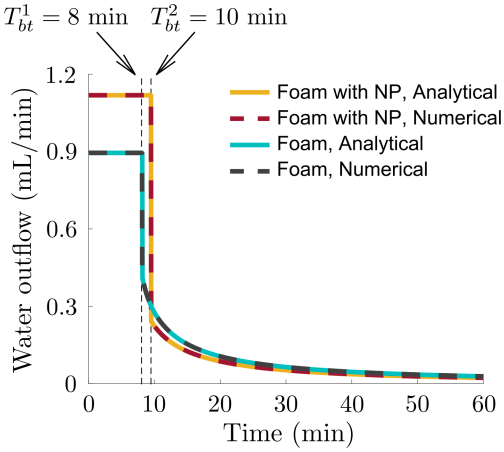

Figure 34 – Water outflow rate over time with ($U_R = (0.5, 1)$) and without ($U_R = (0.5, 0)$) nanoparticles for the same injection condition $U_L = (0.2, 0)$. The addition of nanoparticles increases the breakthrough time and, after T_{bt}^2, the outflow rate is lower than without nanoparticles.

Note that for both CS- and SC-wave sequences, the total WP tends to the same values for large times because when the reservoir reaches its minimum water content, the total amount of produced water must be the same. For the particular case plotted in Fig. 30, the last wave of the solution is a rarefaction and, since $U_L = (0, 0)$, the water production curves meet at $T = \lambda_S(U_L)^{-1} = \infty$. The following theorem generalizes this discussion, proving that the difference in WP between two cases with different initial nanoparticle concentrations always tends to zero over time.

Theorem 3.4. *Consider the Riemann problem* (3.1)-(3.2) *with the injection condition* $U_L = (S_L, 0)$ *and initial conditions* $U_R^1 = (S_R, C_R^1)$ *(case 1) and* $U_R^2 = (S_R, C_R^2)$ *(case 2). At long times, the difference in WP between cases 1 and 2 tends to zero.*

Proof. The Riemann problem solution is a sequence of waves: shock, rarefactions, and contacts. Consider t_j as the time when the slowest wave composing the solution of case j

reaches the reservoir's end and WP_j the water production curve for this case ($j = 1, 2$). For $t^* = \max(t_1, t_2)$, the reservoir reached its minimum water content, i.e., the water saturation profile is constant and equal to S_L. Calculating the WP by using the inflow rate and integrating the water saturation profiles (see Eq. (3.61)), we obtain

$$\mathrm{WP}_1(t^*) = \mathrm{WP}_2(t^*) = f(S_L, 0)t^* + S_R - S_L, \tag{3.67}$$

yielding $\Delta\mathrm{WP}(t^*) = |\mathrm{WP}_2(t^*) - \mathrm{WP}_1(t^*)| = 0$. After t^* the WP curves increase linearly over time since the outflow rate is constant ($f(S_L, 0)$; see Eq. (3.62)). Then, $\Delta\mathrm{WP}(t) = 0$ for all $t \geq t^*$.

Note that t^* can be infinity since the velocity of the slowest wave can be zero. In this case, $\lim_{t\to\infty} \Delta\mathrm{WP}(t) = 0$ by Eq. (3.67).

□

3.6 STRUCTURAL INSTABILITY OF THE SOLUTION

Given a left state U_L and a right state U_R located in only one of the regions R_1, R_2, or R_3 defined by Eqs. (3.51)-(3.52), there is a single compatible wave sequence connecting U_L to U_R determined by Theorem 3.3. However, at the boundary of these regions, more than one wave sequence can be compatible, as represented by the two-color dashed lines in Fig. 19; see Section 3.2. Following [129], the Riemann problem solution is structurally stable if perturbations in the initial data or the flux function do not change the number and types of its component waves. For system (3.9)-(3.10) the structural stability of the solution is lost if when

- U_R is on the curve $\Gamma(U_\mathcal{T}) \cap \mathcal{R}$, for any U_L fixed (Case 1);
- U_R is on the curve $\{U \in \mathcal{L} \mid C = C_\mathcal{T}\}$ and $U_L \in \mathcal{L}$ (Case 2);
- $U_R = U_\mathcal{T}$ and $U_L \in \mathcal{L}$ (Case 3).

Each of these three cases is analyzed below.

Case 1: $U_R \in \Gamma(U_L) \cap \mathcal{R}$

We study separately the cases: $U_L \in \mathcal{L}$, $U_L \in \mathcal{T}$, and $U_L \in \mathcal{R}$. If $U_L \in \mathcal{L}$, both CS- and SC-wave sequences are valid solution types; Fig. 35 presents an example. In this example, the CS-wave sequence is a contact connecting U_L to the intermediate state U_{M_1} and a shock connecting U_{M_1} to U_R, while the SC-wave sequence is a shock connecting U_L to the intermediate state U_{M_2} and a contact connecting U_{M_2} to U_R.

If $U_L \in \mathcal{T}$, both C-wave and CS-wave sequence are valid solution types; Fig. 36 presents an example. In this example, the CS-wave sequence is a contact connecting U_L

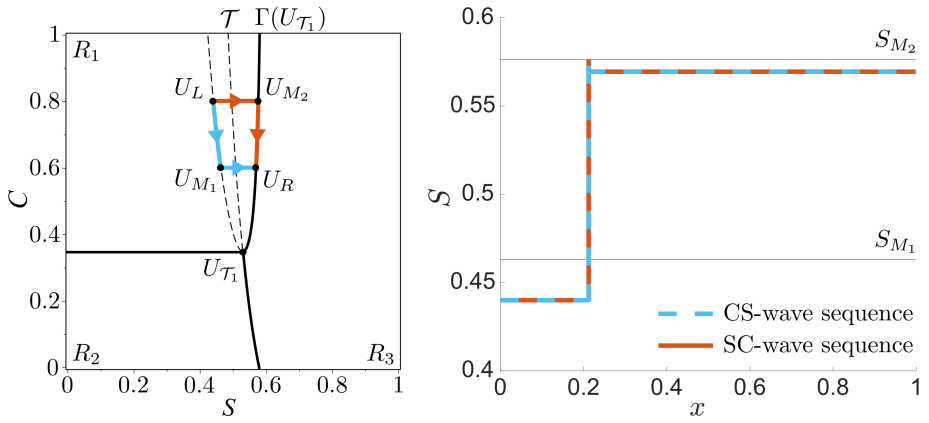

Figure 35 – Example of Case 1 when $U_L \in \mathcal{L}$ for initial states $U_L = (0.44, 0.8)$ and $U_R = (0.5694657531, 0.6)$. The left panel shows the solution in the phase plane, and the right panel shows the water saturation profiles for a dimensionless time $T = 0.15$. The valid solution types are CS- (blue lines) and SC-wave sequences (orange lines).

to the intermediate state U_M and a shock connecting U_M to U_R. If $U_L \in \mathcal{R}$, SC-wave sequence and SCS_1-wave sequence are valid solution types; Fig. 37 presents an example. In this example, the SC-wave sequence is a rarefaction connecting U_L to the intermediate state U_1 and a contact connecting U_1 to U_R. The SCS_1-wave sequence is also composed of the rarefaction connecting U_L to U_1, but U_1 is connected to another intermediate state U_2, followed by a shock connecting U_2 to U_R.

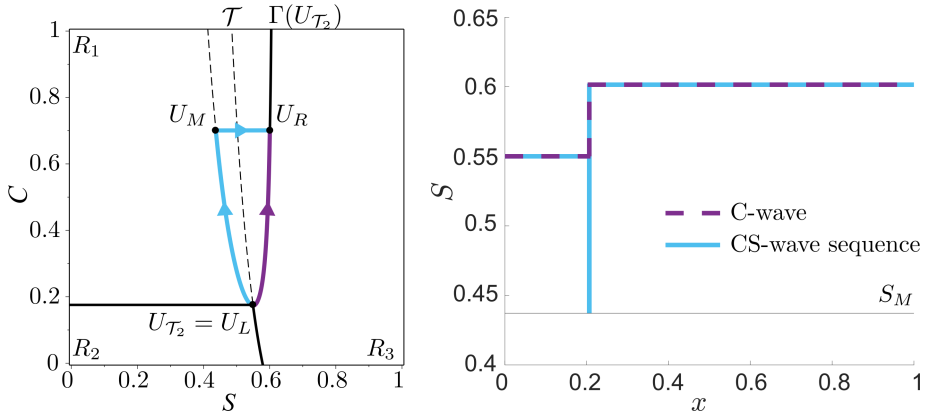

Figure 36 – Example of Case 1 when $U_L \in \mathcal{T}$ for initial states $U_L = (0.55, 0.1751524842)$ and $U_R = (0.6014939685, 0.7)$. The left panel shows the solution in the phase plane, and the right panel shows the water saturation profiles for a dimensionless time $T = 0.15$. The valid solution types are C-wave (purple lines) and CS-wave sequence (blue lines).

Case 2: $U_R \in \{U \in \mathcal{L} \mid C = C_{\mathcal{T}_1}\}$ and $U_L \in \mathcal{L}$

For this case, both CS-wave sequence and SCS_2-wave sequence are valid solution types; Fig. 38 presents an example. In this example, the CS-wave sequence is a contact connecting U_L to the intermediate state U_2 and a rarefaction followed by a shock connecting U_2 to U_R. The SCS_2-wave sequence is a shock connecting U_L to U_1, a contact connecting U_1 to U_2, and a rarefaction followed by a shock connecting U_2 to U_R.

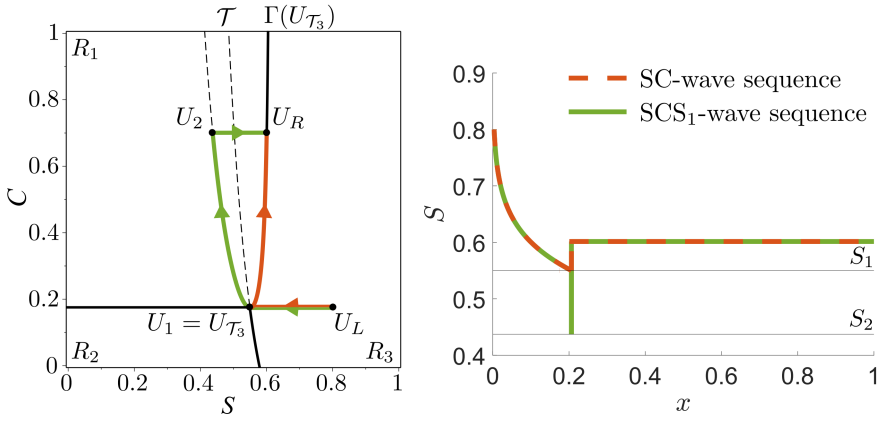

Figure 37 – Example of Case 1 when $U_L \in \mathcal{R}$ for initial states $U_L = (0.8, 0.1751524842)$ and $U_R = (0.6014939685, 0.7)$. The left panel shows the solution in the phase plane, and the right panel shows the water saturation profiles for a dimensionless time $T = 0.15$. The valid solution types are SC-(orange lines) and SCS_1-wave sequences (green lines).

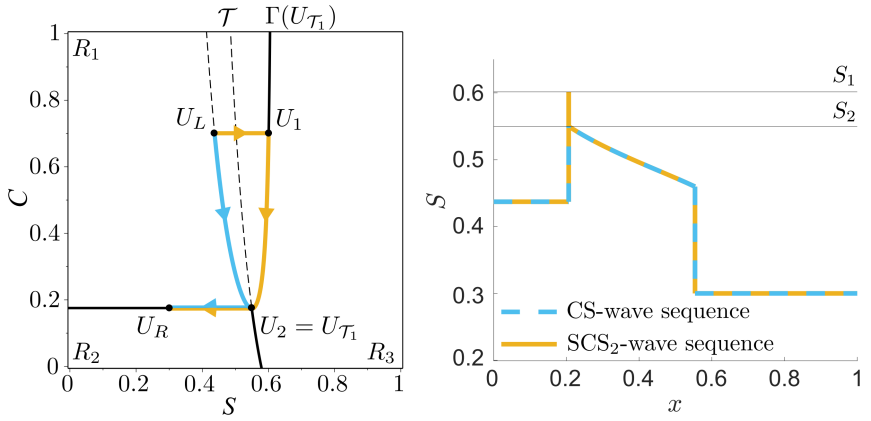

Figure 38 – Example of Case 2 for initial states $U_L = (0.4371890714, 0.7)$ and $U_R = (0.3, 0.1751524842)$. The left panel shows the solution in the phase plane, and the right panel shows the water saturation profiles for a dimensionless time $T = 0.15$. The valid solution types are CS- (blue lines) and SCS_2-wave sequences (yellow lines).

Case 3: $U_R = U_{\mathcal{T}_1}$ and $U_L \in \mathcal{L}$

For this case, both C-wave and SC-wave sequences are valid solution types; Fig. 39 presents an example. In this example, the SC-wave sequence is a shock connecting U_L to the intermediate state U_M and a contact connecting U_M to U_R.

Numerically, it is impossible to pick a point exactly on a curve, so to obtain the two types of compatible solutions, we choose points in the neighborhood of the curve. To perform this test, we use RCD with 10^4 mesh points and 10^{-5} time step; see Section 3.4. Consider $U_L = (0.8, 0.1751524842) \in \mathcal{R}$ and $U_R = (0.6014939685, 0.7) \in \Gamma(U_{\mathcal{T}}) \cap \mathcal{R}$. Both SC-wave sequence and SCS_1-wave sequence are valid solution types; see Fig 37. To numerically obtain the two types of solutions, we consider small variations in S_R: $S_R^+ = 0.602823036$ and $S_R^- = 0.593951052$. Then, U_R^+ and U_R^- are inside regions R_3 and R_1, respectively. The saturation profiles obtained for this example are shown in Fig. 40.

A similar investigation was performed in [91].

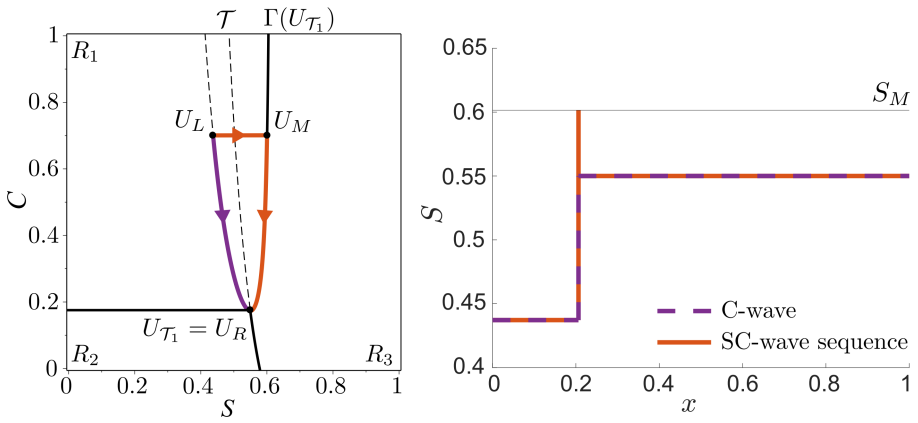

Figure 39 – Example for Case 3 for initial states $U_L = (0.4371890714, 0.7)$ and $U_R = (0.55, 0.1751524842)$. The left panel shows the solution in the phase plane, and the right panel shows the water saturation profiles for a dimensionless time $T = 0.15$. The valid solution types are C-wave (purple lines) and SC-wave sequence (orange lines).

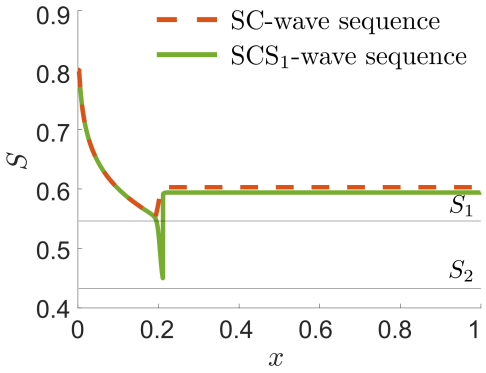

Figure 40 – Water saturation profiles numerically obtained for a dimensionless time $T = 0.15$, and left state $U_L = (0.8, 0.1751524842)$. For $U_R^+ = (0.602823036, 0.7)$ the solution is an SC-wave sequence (dashed orange line), and for $U_R^- = (0.593951052, 0.7)$ the solution is an SCS_1-wave sequence (green line).

3.7 DISCUSSION AND PARTIAL CONCLUSIONS

In this chapter, we proposed a new model for NP-stabilized foam flow in porous media, with the flow dependence on nanoparticle concentration formulated from the literature's experimental data. Our model consists of a non-strictly hyperbolic system of conservation laws, which is solved for a generic Riemann problem initial conditions. The mathematical solution changes qualitatively compared to the same model without nanoparticles. This is due to a contact discontinuity that appears when we move from one fractional flow curve to another (the concentration of nanoparticles changes). We proved the existence of a global solution, presenting the necessary and sufficient conditions to guarantee the compatibility of the wave sequences. We classified the phase plane S-C

according to these compatible wave sequences. All analytical results are in good agreement with direct numerical simulations.

The breakthrough time and water production are the most interesting parameters for industrial applications. The presented analytical framework allows for obtaining both. When only gas is injected, the breakthrough time and the production increase with the nanoparticle concentration. For example, when the concentration increased from 0.0% to 1.0%, the time for producing 32 mL of water decreased from 61 to 26 min. We also observe that the effect of nanoparticles is less pronounced for high nanoparticle concentration, which agrees with the literature and corroborates the proposed model.

Literature [19–24] suggests that adding nanoparticles increases the foam stability improving the reservoir's sweep efficiency during the drainage procedure (mainly gas injection): increasing the breakthrough time and increasing water production. The model presented in Section 3.1 considers that the Mobility Reduction Factor (MRF), in agreement with the literature, increases in the presence of nanoparticles. Counterintuitively, considering the water-gas co-injection for a certain parameter range, adding nanoparticles changes the mathematical solution qualitatively, yielding lower breakthrough time. In this case, the effect of nanoparticles on water production is negligible regardless of the concentration considered.

To better understand the presented results, we map all initial and injection conditions corresponding to relative values of the WP for the cases with and without nanoparticles in Fig. 41. For this map, we consider the breakthrough time for NP-stabilized foam flow, with $C_R = 1$. Notice that nanoparticles do not affect WP in the region corresponding to the SC-wave sequence, while it modifies WP in the CS-wave sequence region by changing the corresponding solution qualitatively. On the other hand, the major impact on WP happens for low values of the initial water saturations, where it reaches approximately 37%.

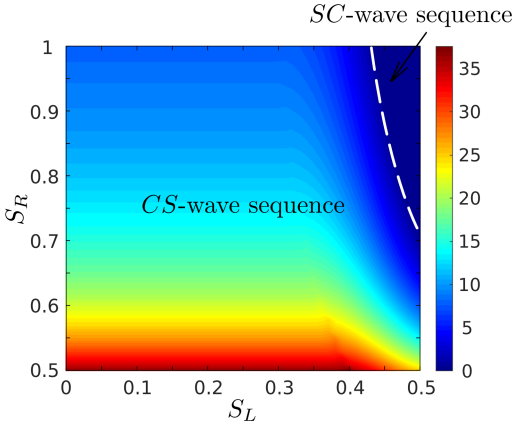

Figure 41 – Mapping the difference in WP (%) due to the addition of nanoparticles for $S_L \in [0, 0.5]$ and $S_R \in [0.5, 1]$ ($C_L = 0$, $C_R = 1$) at the moment of breakthrough.

Our results indicate that it is possible to observe the effect of nanoparticles in laboratory experiments during water-gas co-injection core-flooding, which is a widely used laboratory experiment technique [22, 24, 94]. The difference in production can be most effectively observed by measuring the time to produce a fixed amount of water and choosing a parameter range more favorable to the deployment of nanoparticles. Mapping several initial and injection conditions (Fig. 41) we observed that the smaller S_R, the higher the increase in water production. High values of S_L, especially if S_R is also high, lead to a region where the solution changes qualitatively and the effect of nanoparticles is negligible. Based on our analysis (see Fig. 41), we believe that the best conditions to observe the increase in production occur for the reservoir partially saturated ($S_R \in [0.5, 0.6]$) and a co-injection water/gas ratio of up to 40/60% ($S_L \in [0, 0.4]$).

4 UNCERTAINTY QUANTIFICATION AND SENSITIVITY ANALYSIS FOR NP-STABILIZED FOAM FLOW

In this chapter, we perform uncertainty quantification and sensitivity analysis studies for NP-stabilized foam flow. We consider the Riemann problem (3.13)-(3.15) (foam in local equilibrium and negligible retention) with quadratic relative permeabilities. The solution remains qualitatively the same as the more realistic (non-quadratic) case, including the solution structure. This simplification is generally used to facilitate mathematical investigations [133,134] and can be obtained from the classical Corey relative permeabilities [77] with the tortuosity factor equal to zero; see [85] for details. The flow models with foam and nanoparticles presented in [20, 41] also used quadratic Corey and showed good agreement with experiments [42]. Note that numerical tools are still required for constructing the analytical solution in Chapter 3 due to the complexity of the fractional flow function. The model proposed here allows algebraic expressions to determine the solution type and construct the solution profiles, speeding up the calculations significantly.

As in Chapter 3, we follow the core-flood experiment reported in [44] for practical examples, with the physical parameters of Table 2; see Section 3.3. Table 5 presents the parameters of the quadratic relative permeability model. We calculated $c_{k_{rg}}$ and $c_{k_{rw}}$ using the least squares method to fit the fractional flow function with quadratic relative permeabilities to the original fractional flow function [92].

Table 5 – Parameters of the quadratic relative permeability model.

Symbol	Parameter	Value
n_w $(-)$	Corey exponent for water relative perm.	2.0
n_g $(-)$	Corey exponent for gas relative perm.	2.0
$c_{k_{rg}}$ $(-)$	Gas endpoint relative perm.	3.95
$c_{k_{rw}}$ $(-)$	Water endpoint relative perm.	0.25

Section 4.1 compares the analytical solution of the quadratic model with numerical simulations. In Section 4.2, we use the simpler model to derive algebraic expressions to construct the solution profiles, presented in Section 4.3. Section 4.4 presents the model setup for UQ and SA studies. Finally, Section 4.5 and Section 4.6 investigates the uncertainty propagation and model's sensitivity using the analytical framework. In Section 4.7, we present discussions and partial conclusions based on the results presented in this chapter.

The results presented in this chapter are summarized in the paper [66]. In [135], we perform UQ and SA studies considering a particular case of the global solution for the NP-stabilized foam flow model presented here.

4.1 NUMERICAL VALIDATION

The analytical solution of the quadratic model is validated by performing direct numerical simulations with RCD (10^4 mesh points and 10^{-5} time step), analogous to what was done for the original model in Section 3.4. We use the parameters of Tables 2 and 5.

We provide examples of two types of solutions: CS- and SC-wave sequences. When the injection condition is $U_L = (0.2, 0.2)$, and the initial reservoir condition is $U_R = (0.8, 0.8)$, the solution is a CS-wave sequence, as shown in the left panel of Fig. 42. On the other hand, when $U_L = (0.5, 0.4)$ and $U_R = (0.9, 0.9)$, the solution is an SC-wave sequence, as shown in the left panel of Fig. 43. In both Figs. 42 and 43, the right panel demonstrates good agreement between the analytical and numerical solutions.

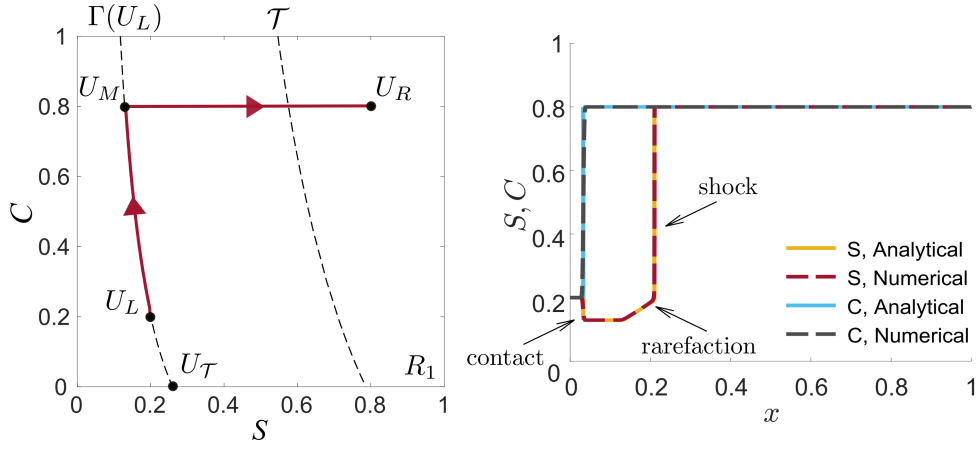

Figure 42 – The solution (CS-wave sequence) composed of a contact connecting U_L to U_M and a rarefaction followed by a shock connecting U_M to U_R, for $U_L = (0.2, 0.2)$ and $U_R = (0.8, 0.8)$. The left panel shows the phase plane S-C, and the right panel compares the analytical and numerical solution profiles at dimensionless time $T = 0.15$.

The convergence of numerical simulations is verified by comparing the numerical solutions $\mathcal{U}$ for meshes of $N/2$ and N points with their corresponding time steps. The relative errors (calculated by the l_2 Euclidean norm) for each discretization are presented in Table 6, considering an example with $U_L = (0.2, 0.2)$ and $U_R = (0.8, 0.8)$) at time $T = 0.15$ (before the breakthrough). Linear convergence is shown in Figure 44, with the relative error decreasing as the mesh size increases. As in Section 3.4, the relative error stabilizes close to 10^{-5} when machine precision is reached for each difference $\mathcal{U}_{N/2} - \mathcal{U}_N$.

Table 6 – Relative errors for different mesh refinement.

Mesh points	Time step	Relative error (%)
$4.0 \cdot 10^3$	$8.0 \cdot 10^{-5}$	$2.618 \cdot 10^{-4}$
$8.0 \cdot 10^3$	$4.0 \cdot 10^{-5}$	$1.568 \cdot 10^{-4}$
$1.6 \cdot 10^4$	$2.0 \cdot 10^{-5}$	$2.803 \cdot 10^{-5}$
$3.2 \cdot 10^4$	$1.0 \cdot 10^{-5}$	$1.144 \cdot 10^{-5}$

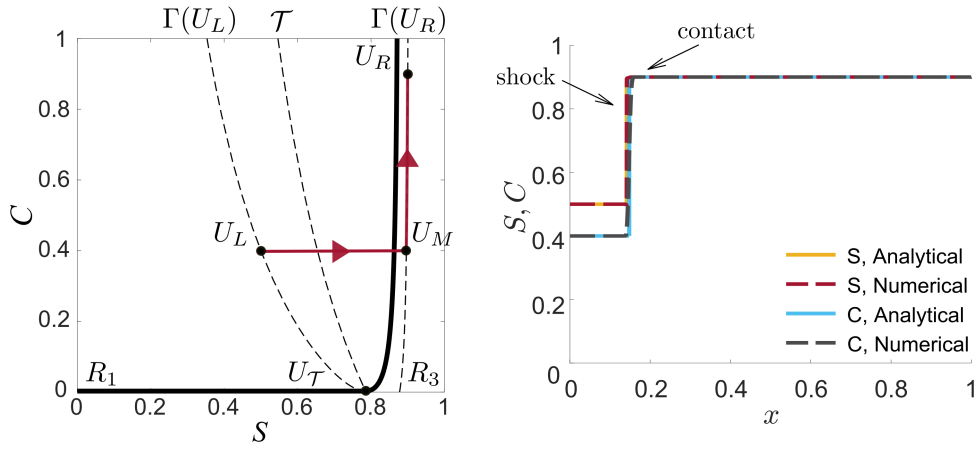

Figure 43 – The solution (SC-wave sequence) composed of a shock connecting U_L to U_M and a contact connecting U_M to U_R, for $U_L = (0.5, 0.4)$ and $U_R = (0.9, 0.9)$. The left panel shows the phase plane S-C, and the right panel compares the analytical and numerical solution profiles at dimensionless time $T = 0.15$. Note that the water saturation values of U_M and U_R are almost the same, then the water saturation profile practically does not change with the nanoparticle concentration.

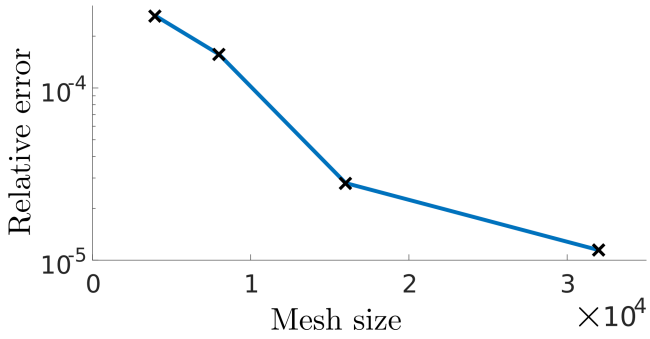

Figure 44 – The convergence of numerical simulations (order 2.8) for the spatial and temporal discretizations is presented in Table 6.

We also compare WP obtained using analytical and numerical water saturation profiles for the examples presented in Figs. 42 and 43; see Subsection **4.2.3** for details of WP calculations. We found a good agreement between them, as shown in Fig 45.

4.2 ALGEBRAIC EXPRESSIONS FOR THE ANALYTICAL SOLUTION

Using the quadratic model, we can derive algebraic expressions to determine the solution type and construct the solution profiles without solving any equation numerically. This is a significant advantage of using a simpler model, as it drastically reduces the time required to obtain solutions, allowing us to perform a UQ and SA study (described in the next chapter) in a feasible time.

This section is divided into two parts. First, we describe how to find (algebraically) the solution type when we have a sequence of C- and S-waves. Then, we detail how to

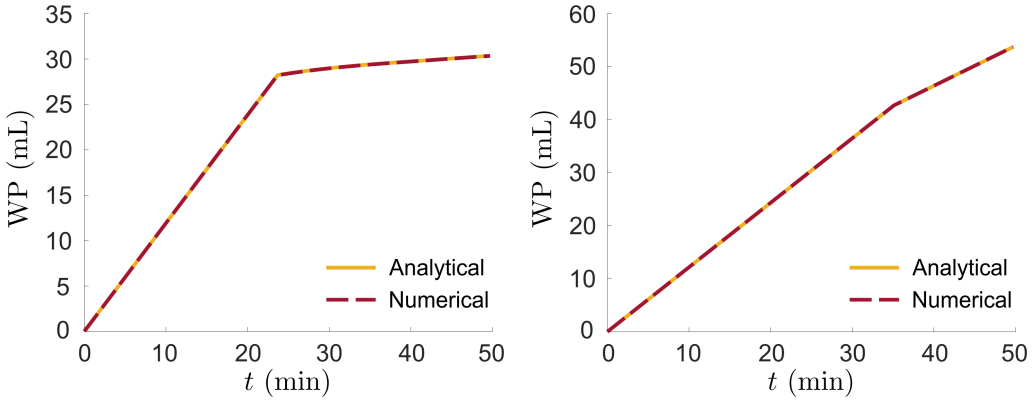

Figure 45 – Comparison between analytical and numerical water production over time. The left panel shows WP for $U_L = (0.2, 0.2)$ and $U_R = (0.8, 0.8)$, where the solution is a CS-wave sequence; see Fig. 42. The right panel shows WP for $U_L = (0.5, 0.4)$ and $U_R = (0.9, 0.9)$, where the solution is an SC-wave sequence; see Fig. 43.

construct this solution since we need to determine all the intermediate states. We must solve a third-order polynomial equation in both parts to find saturation values. We use the polynomial coefficients vector $A = (a_1, a_2, a_3, a_4)$ to describe an equation

$$a_1 S^3 + a_2 S^2 + a_3 S + a_4 = 0. \tag{4.1}$$

The physically correct saturation solution among the three roots must be a real parameter within the interval $I = [0, 1]$. We will indicate if the solution is the root S_1, S_2, or S_3, which are defined below.

In some cases, $a_1 = 0$ in Eq. (4.1), and we obtain a quadratic equation with roots

$$S_1 = \frac{-a_3 - \sqrt{\Delta}}{2a_2}, \quad S_2 = \frac{-a_3 + \sqrt{\Delta}}{2a_2}, \tag{4.2}$$

where $\Delta = a_3^2 - 4a_2a_4$ is the discriminant. We apply the Cardano's Method [121, 122] for the general case. First of all, we rewrite the equations for $h = S + a_2/(3a_1)$ as

$$h^3 + A_1 h + A_2 = 0, \tag{4.3}$$

where

$$A_1 = \frac{a_3}{a_1} - \frac{a_2^2}{3a_1^2}, \quad A_2 = \frac{a_4}{a_1} + \frac{2a_2^3}{27a_1^3} - \frac{a_2a_3}{3a_1^3}. \tag{4.4}$$

Then, the roots are determinate according to the discriminant $\Delta = (A_1/2)^2 + (A_2/3)^3$ as follows.

1. If $\Delta = 0$:

$$h_1 = -(4A_2)^{1/3}, \quad h_2 = h_3 = (A_2/2)^{1/3}. \tag{4.5}$$

2. If $\Delta > 0$:

$$h_1 = (-A_2/2 + \sqrt{\Delta})^{1/3} + (-A_2/2 - \sqrt{\Delta})^{1/3} \tag{4.6}$$

$$h_2 = \frac{-h_1 - \sqrt{-3h_1^2 + 4A_1}}{2}, \quad h_3 = \frac{-h_1 + \sqrt{-3h_1^2 + 4A_1}}{2}. \tag{4.7}$$

3. If $\Delta < 0$:

$$h_1 = 2\rho^{1/3}\cos(\theta/3), \tag{4.8}$$

$$h_2 = 2\rho^{1/3}\cos\left(\frac{\theta+2\pi}{3}\right), \quad h_3 = 2\rho^{1/3}\cos\left(\frac{\theta+4\pi}{3}\right), \tag{4.9}$$

where $\rho = \sqrt{A_2^2/4 + |\Delta|}$ and $\theta = \arccos(-A_2/(2\rho))$.

Finally, the saturation solution is one of the three roots $S_j = h_j - a_2/(3a_1)$ $(j = 1, 2, 3)$. For each point of interest, the physically correct solution (real and inside the interval $[0, 1]$) was found by substituting the model's parameters (Table 2).

4.2.1 Analysis of the solution type

To simplify the calculations, let us rewrite the fractional flow function (3.11) as

$$f(U) = \frac{S^2}{S^2 + p(C)(1-S)^2}, \tag{4.10}$$

where

$$p(C) = \frac{\mu_w c_{k_{rg}}}{\mu_g c_{k_{rw}}}[MRF(C)]^{-1}. \tag{4.11}$$

Then, the partial derivate in relation to S is given by

$$\partial_S f(S, C) = \frac{2p(C)S(1-S)}{[S^2 + p(C)(1-S)^2]^2}. \tag{4.12}$$

Given injection and initial states U_L and U_R, the first step to find the solution using the framework developed in Section 3.2 is to determine whether U_L is located in $\mathcal{L} \cup \mathcal{T}$ or $\mathcal{R}$. Note that, for a fixed C_L, the transition between these regions is the point of the fractional flow curve where $\lambda_C = f/(S+a) = \partial_S f = \lambda_S$; see Fig. 46. After substituting Eq. (4.10) in $f/(S+a) = \partial_S f$, and performing some algebraic transformations, we can describe the transition curve (3.34) using $p(C(S))$:

$$p(S) = -\frac{S^3}{(S-1)(S^2+S+2a)}. \tag{4.13}$$

To obtain an expression for $C(S)$, we use the definition of the function $p(C)$ (4.11).

The next step is to determine the point $U_{\mathcal{T}}$ dividing the phase plane S-C into regions R_1, R_2, or R_3; see Eqs. (3.51)-(3.52). We use the curve $\Gamma(V)$ composed of all states with the same eigenvalue as $V \in \Omega$ (3.49). For each V, analogous to the transition curve, we describe $\Gamma(V)$ using $p(C(S))$. Defining $\kappa = \lambda_C(V)$ and substituting Eq. (4.10) in the other term of Eq. (3.49), after some algebraic transformations we obtain

$$p_\kappa(S) = -\frac{S^2(k(S+a)-1)}{k(S-1)^2(S+a)}. \tag{4.14}$$

The $U_{\mathcal{T}}$ definition depends on the U_L location (see Eqs. (3.53) and (3.54)) as follows

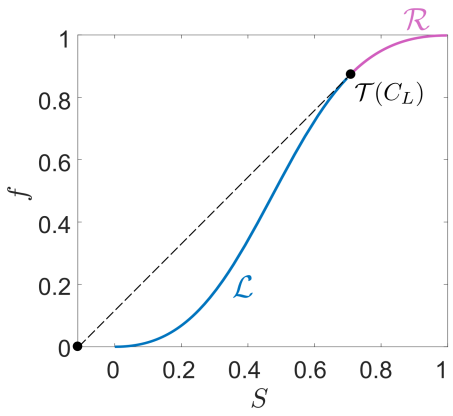

Figure 46 – The fractional flow function (for C_L fixed) and the point $\mathcal{T}(C_L)$, dividing the curve in $\mathcal{L}$ and $\mathcal{R}$.

- If $U_L \in \mathcal{T}$, by definition $U_\mathcal{T} = (S_L, C_L)$.
- If $U_L \in \mathcal{L}$, $U_\mathcal{T}$ is the intersection between $\mathcal{T}$ and $\Gamma(U_L)$. Equating expressions (4.13) and (4.14) (with $V = U_L$), we obtain that the saturation $S_\mathcal{T}$ is the root S_1 of the equation with polynomial coefficients vector

$$A = (0,\ 1 - 2\lambda_C(U_L),\ 1 - 4a\lambda_C(U_L),\ 2a - 2a^2\lambda_C(U_L)). \tag{4.15}$$

  Note that the third-order equation is reduced to a quadratic equation. The concentration $C_\mathcal{T}$ is the intersection between $\mathcal{T}$ and the line $S = S_\mathcal{T}$, so it can be determine by evaluating Eq. (4.13) in $S_\mathcal{T}$. If $\Gamma(U_L)$ does not reach the minimum in Ω, $S_\mathcal{T}$ is the intersection between $\Gamma(U_L) \cap \mathcal{R}$ and the line $C = 0$, so it can be determine by equating Eq. (4.14) (with $V = U_L$) to zero. After some simplifications, $S_\mathcal{T}$ is the root S_3 of the equation with polynomial coefficients vector

$$A = (\lambda_C(U_L)(p(0) + 1),\ \lambda_C(U_L)(p(0)a - 2p(0) + a) - 1, \tag{4.16}$$
$$p(0)\lambda_C(U_L)(1 - 2a),\ p(0)\lambda_C(U_L)a). \tag{4.17}$$

  In this case, $C_\mathcal{T} = 0$.

- If $U_L \in \mathcal{R}$, $U_\mathcal{T}$ is the intersection between $\mathcal{T}$ and the line $C = C_L$. Therefore, $C_\mathcal{T} = C_L$ and $S_\mathcal{T}$ can be determine by equating Eq. (4.13) to C_L. The saturation $S_\mathcal{T}$ is the root S_1 of the equation with polynomial coefficients vector

$$A = (p(C_L) + 1,\ 0,\ p(C_L)(2a - 1),\ -2ap(C_L)). \tag{4.18}$$

4.2.2 Construction of the water saturation profiles

We focus on two solution types to construct the water saturation profiles: SC- and CS-wave sequences. The results can be simplified to C- and S-wave cases or combined to SCS_1- and SCS_2-wave sequence cases.

Since the states connected by a C-wave and the point $(-a, 0)$ are on the same line, for a CS-wave sequence we can determine S_M (3.55) by solving the equation

$$\frac{f(S_M, C_R)}{S_M + a} = \frac{f(S_L, C_L)}{S_L + a}. \tag{4.19}$$

Similarly, for an SC-wave sequence, we can determine S_M (3.56) by solving

$$\frac{f(S_M, C_L)}{S_M + a} = \frac{f(S_R, C_R)}{S_R + a}. \tag{4.20}$$

To construct the solution, we must also analyze if the S-wave is a rarefaction, a shock, or a rarefaction followed by a shock. To solve this typical Buckley-Leverett problem, we use the inflection point $S^I(C)$ and the "convex-hull" S^*, which is obtained with the Welge's method ($\partial_S f(S^*, C)(S - S^*) = f(S, C) - f(S^*, C)$); see Subsection **2.1.1** for details. Fig. 47 illustrates the water saturation profile construction.

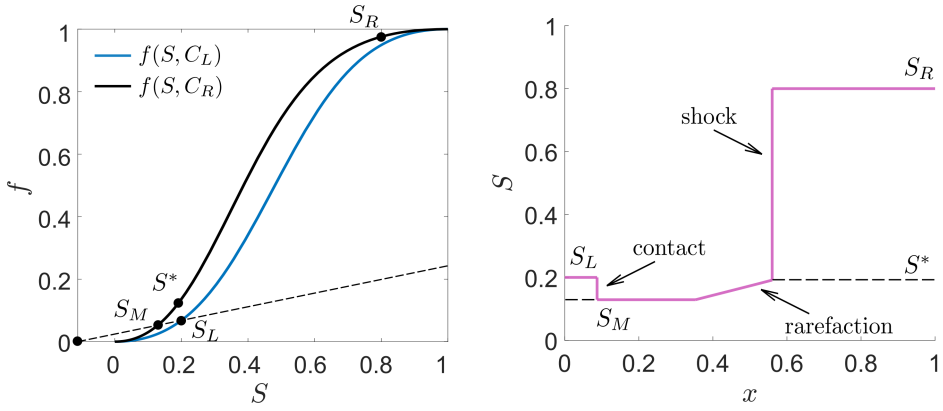

Figure 47 – Construction of the solution for $U_L = (0.2, 0.2)$ and $U_R = (0.8, 0.8)$. The solution (CS-wave sequence) is composed of a contact connecting U_L to U_M, a rarefaction connecting U_M to $U^* = (S^*, C_R)$ and a shock connecting U^* to U_R. The left panel shows the fractional flow functions, where we move from one fractional flow curve to another through the contact wave. The right panel details the water saturation profile.

Now, we will present algebraic expressions for the saturation of the intermediate states. After some calculations, we obtain that S_M is one of the three roots of the equation with polynomial coefficients vector

$$A = (1 + p(C_1),\ a + p(C_1)(a - 2) - 1/\lambda_C(U_2), \tag{4.21}$$

$$p(C_1)(1 - 2a),\ p(C_1)a), \tag{4.22}$$

where $U_1 = (S_1, C_1)$ and $U_2 = (S_2, C_2)$ can take the values of U_L or U_R depending on the solution type. In the case of a CS-wave sequence, $U_1 = U_R$, $U_2 = U_L$, and the root is S_3. In the case of an SC-wave sequence, $U_1 = U_L$, $U_2 = U_R$, and the root is S_1. When the S-wave is a rarefaction followed by shock, the other intermediate state S^* is the root S_2 of the equation with polynomial coefficients vector

$$A = ((2S_1 - 1)(p(U_1) + 1),\ (-2S_1^2 - S_1)(p(U_1) + 1), \tag{4.23}$$

$$2S_1^2(p(U_1) + 1) + p(U_1),\ -S_1 p(U_1)). \tag{4.24}$$

For a CS-wave sequence, U_1 takes the value of U_R, and for an SC-wave sequence, U_1 takes the value of U_M.

The solution construction is completed with the expression for the inflection point in Eq. (3.21); see Proposition 3.1.

4.2.3 On the water production and pressure calculations

The water production for the quadratic model is calculated analogous to the original model, but the algebraic expressions introduced in this section reduce the use of numerical tools. Again, we focus on the CS-wave sequence type solution, where WP is calculated by Eqs. (3.63) or (3.64), as presented in Section 3.3.

If the S-wave is a shock, the time that contact and shock waves reach the end of the reservoir can be directly obtained using f and $\partial_S f$; see Eqs. (4.10) and (4.12). Therefore, with Eq. (3.63) and the expression to S_M developed in Subsection **4.2.2**, water production can be calculated algebraically.

If the S-wave is a rarefaction followed by a shock, there are two intermediate states (S_M and S^*). They are calculated by using the expressions developed in Subsection **4.2.2**. Note that S^* is not explicit on WP calculations (3.64), but it is necessary to calculate the breakthrough time. In this case, the saturation at the reservoir's end varies with time during the rarefaction wave, being described by the differential equation $\partial_S f(S(t), C_R) = 1/t$. For the original model, this value was found numerically. Here, we significantly reduce costs by developing an expression to find $S(t)$. This value is determinate by the fourth-order polynomial equation $a_1 S^4 + a_2 S^3 + a_3 S^2 + a_4 S + a_5$, with coefficients

$$a_1 = (p(C_R) + 1)^2, \tag{4.25}$$
$$a_2 = -4p(C_R)[p(C_R) + 1], \tag{4.26}$$
$$a_3 = 6p(C_R)^2 + 2p(C_R)(t + 1), \tag{4.27}$$
$$a_4 = -2p(C_R)[2p(C_R) + t], \tag{4.28}$$
$$a_5 = p(C_R)^2. \tag{4.29}$$

We apply the Ferrari's Method [122, 136], first rewriting the equations as

$$h^4 + A_1 h^2 + A_2 h + A_3 = 0, \tag{4.30}$$

where

$$A_1 = \frac{a_3}{a_1} - \frac{3a_2^2}{8a_1^2}, \quad A_2 = \frac{a_2^3}{8a_1^3} - \frac{a_2 a_3}{2a_1^2} + \frac{a_4}{a_1}, \tag{4.31}$$
$$A_3 = \frac{-3a_2^4}{256a_1^4} + \frac{a_5}{a_1} - \frac{a_2 a_4}{4a_1^2} + \frac{a_2^2 a_3}{16a_1^3}. \tag{4.32}$$

We will use an auxiliary equation $g^3 + 2A_1 g^2 + (A_1^2 - 4A_3)g - A_2^2 = 0$. The three roots can be found through the framework for third-order polynomial equations developed previously,

using $a_1 = 1$, $a_2 = 2A_1$, $a_3 = (A_1^2 - 4A_3)$, and $a_4 = -A_2^2$. After substituting the model's parameters (Table 2), the real root is the first one, which we call g_1. Finally, we calculated the roots of Eq. (4.30) as follows

$$h_1 = 0.5\left(\sqrt{g_1} + \sqrt{-g_1 - 2A_1 - 2A_2 g_1^{-\frac{1}{2}}}\right), \tag{4.33}$$

$$h_2 = 0.5\left(\sqrt{g_1} - \sqrt{-g_1 - 2A_1 - 2A_2 g_1^{-\frac{1}{2}}}\right), \tag{4.34}$$

$$h_3 = 0.5\left(-\sqrt{g_1} + \sqrt{-g_1 - 2A_1 + 2A_2 g_1^{-\frac{1}{2}}}\right), \tag{4.35}$$

$$h_4 = 0.5\left(-\sqrt{g_1} - \sqrt{-g_1 - 2A_1 + 2A_2 g_1^{-\frac{1}{2}}}\right). \tag{4.36}$$

The saturation is one of the four roots $S_j = h_j - a_2/(4a_1)$ $(j = 1, 2, 3)$. With the model's parameters, the physically correct solution is S_2. Finding this expression simplifies the calculations, but numerical integration is still needed to obtain WP during the rarefaction wave.

From the extension of Darcy's law to multi-phase flow, the partial velocity of a j-phase is $u_j = -\lambda_j \nabla p_j$; see Subsection **2.2.2**. For water-gas flow, $j = w, g$ representing aqueous and gaseous phases, and $P_c = p_g - p_w$ is the capillary pressure. In our model, we neglect the effects of capillary pressure, so $p_w = p_g = P$. By using that $u_w = uf$, $u_g = uf_g = u(1 - f)$, and $f = \lambda_w/\lambda_T$, we obtain

$$p_w = p_g = -u \int \frac{1}{\lambda_T}\, dx. \tag{4.37}$$

Then, assuming that the pressure at the core outlet is constant ($P(1, t) = P_{out}$), we can estimate the pressure at each point $\tilde{x} \in [0, 1]$ for a fixed t as

$$P(\tilde{x}, t) = u \int_{\tilde{x}}^{1} \frac{1}{\lambda_T(S(x, t), C(x, t))}\, dx + P_{out}, \tag{4.38}$$

where $\lambda_T = \lambda_w + \lambda_g$ is the total mobility. Note that the pressure drop is calculated as $\Delta P(t) = P(0, t) - P(1, t)$.

4.3 SOLUTION PROFILES

In order to better understand how nanoparticles affect foam flow in the quadratic model, we present some preliminary results. Fig. 48 shows water saturation profiles at $t = 5$ min (before breakthrough) for different nanoparticle concentrations. Note that the presence of nanoparticles results in a delay of the gas front, consequently leading to a delay in breakthrough. The bubble density (calculated as $(1 - S) \cdot n_{max}(C)$) at the same time is presented in the left panel of Fig. 49. The foam front propagates faster with a lower bubble

density in the case without nanoparticles. In the presence of nanoparticles, the bubble densities can be up to four times greater than the case without nanoparticles. The right panel of Fig. 49 shows the water pressure profiles for different nanoparticle concentrations at $t = 5$ min, considering the pressure at the core's outlet fixed as $P_{out} = 2026.5$ kPa (as in [43]). The pressure of water (or gas) in the core is estimated by integrating the total mobility of the mixture over space. Note that the presence of nanoparticles leads to higher pressures, especially in the core inlet region.

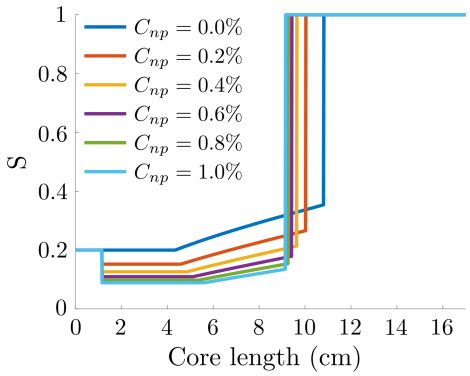

Figure 48 – Effect of nanoparticle concentration on the water saturation profiles during foam flow at $t = 5$ min. This example considers $U_L = (0.2, 0)$ and $U_R = (1.0, C_R)$, with C_R varying between 0 (without nanoparticles) and 1 (maximum nanoparticle concentration). For the case without nanoparticles, the solution is a rarefaction followed by a shock, while for $C_R > 0$, the solution is composed of a contact, a rarefaction, and a shock.

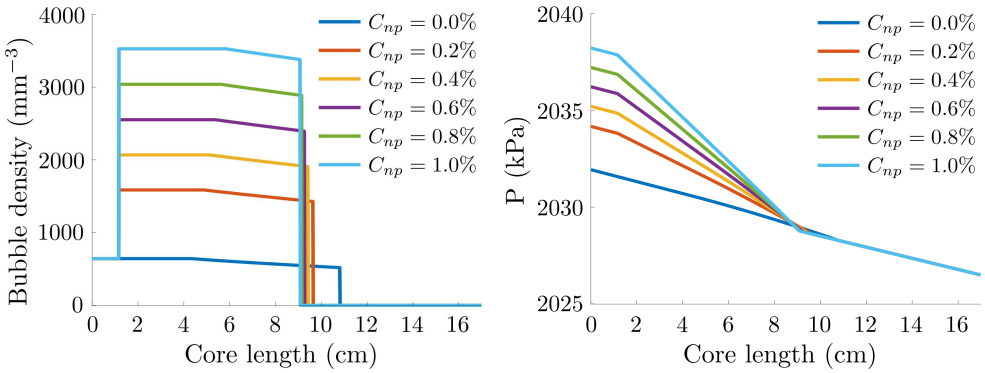

Figure 49 – Effect of nanoparticle concentration on the bubble density profiles (left panel) and the water pressure profiles (right panel) during foam flow at $t = 5$ min. This example considers $U_L = (0.2, 0)$ and $U_R = (1.0, C_R)$, with C_R varying between 0 (without nanoparticles) and 1 (maximum nanoparticle concentration).

4.4 MODEL SETUP FOR UQ AND SA STUDIES

We use the quadratic local equilibrium model to perform an uncertainty quantification and sensitivity analysis for NP-stabilized foam flow. As in Chapter 3, we focus on the drainage process (mainly gas injection) after injecting a chemical slug composed of water, surfactant, and nanoparticles. We consider the Riemann problem (3.13)-(3.15)

with injection condition $U_L = (0.2, 0)$ and initial water saturation $S_R = 1$. The initial nanoparticle concentration C_R varies, but when $C_R > 0$, the solution is always a CS-wave sequence. The particular case $C_R = 0$ represents the foam flow without nanoparticles. In this case, MRF > 1 is constant (see Eq. (3.4)), and the solution is always an S-wave. The S-wave can be a rarefaction followed by a shock (most common case) or a shock.

The forward propagation of uncertainties follows the Monte Carlo method, and we use Sobol indices [65] as a sensitivity measure; see Sections 2.5 and 2.6 for details. These results were computed using the UQLab package [115, 116] with the Latin Hypercube Sampling (LHS) technique.

When conducting uncertainty quantification and sensitivity analysis studies, we must define the relevant quantities of interest. We consider the breakthrough time (T_{bt}), cumulative water production (WP), and pressure drop (ΔP) because they are crucial parameters for industrial applications [131]. All output quantities can be determined by using the analytical solution presented in this chapter.

Consider the set of inputs $Z = \{c_{k_{rg}}, c_{k_{rw}}, b_1, b_2\}$. We assume normal (or Gaussian) distributions $\mathcal{N}(\mu, \sigma)$ for the endpoint relative permeabilities, where μ and σ are the mean and standard deviation. The mean values are calculated using the least squares method to fit the fractional flow function with quadratic relative permeabilities to the original function presented in [92] (based on experimental data [44]). In [137, 138], the authors found errors in the range of 0.2% to 15% in relative permeability estimates from several flow experiments. Therefore, we use a coefficient of variation (CV $= \sigma/\mu$) of 10% for these parameters. The distributions are summarized in Table 7.

Table 7 – Distributions of the permeability parameters. Source: [44, 92]

Symbol	Parameter	Distribution
$c_{k_{rg}}$ (-)	Gas endpoint relative perm.	$\mathcal{N}(3.95, 0.395)$
$c_{k_{rw}}$ (-)	Water endpoint relative perm.	$\mathcal{N}(0.25, 0.025)$

We adopt uniform distributions $\mathcal{U}(\theta_1, \theta_2)$ for the nanoparticles parameters, representing an experiment with arbitrary outcome between θ_1 and θ_2. These coefficients are related to the mean and standard deviation of a distribution by $\theta_1 = \mu - \sqrt{3}\sigma$ and $\theta_2 = \mu + \sqrt{3}\sigma$. We use the least squares method to derive the mean values from literature [30] (based on experimental data [19]); see the left panel in Fig. 50. Since b_1 and b_2 are the angular and linear coefficients of n_{max}, we adopt normal (or Gaussian) copula with coefficient -0.6 to include a negative dependence between them. Then, small values of b_1 are related to large values of b_2 and vice versa. Due to this correlation, we increased the CV of each parameter by 50% to better cover the prediction interval. We obtained a CV of 10.5% for b_1 and 37.5% for b_2; see the distributions in Table 8. The right panel in

Fig. 50 shows samples drawn from these distributions with the normal copula obtained by the MC method.

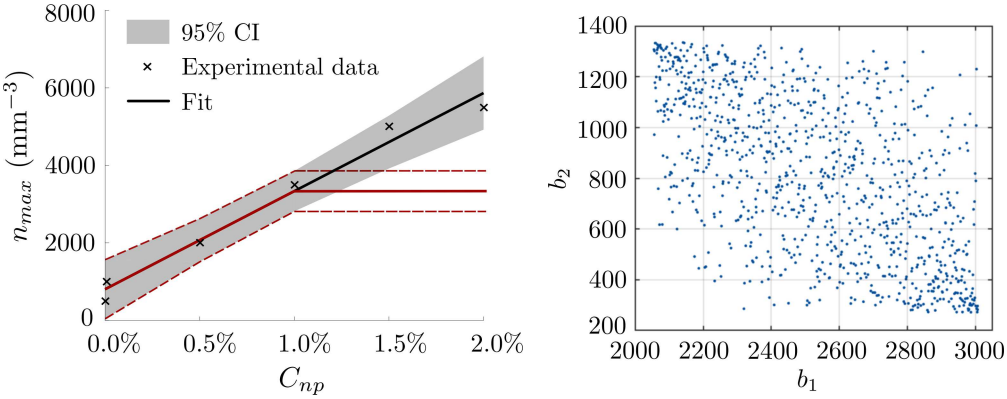

Figure 50 – Distribution and correlation corresponding to nanoparticle parameters. The left panel shows the fit (black line) based on literature data [30] (cross-mark). The mean values are $b_1 = 2531.80$ and $b_2 = 802.58$ (mm^{-3}), with the 95% confidence interval (95% CI) represented by the shaded region. The red lines illustrate the proposed n_{max} (see Eq. (3.7)) and the corresponding 95% CI. The right panel shows samples drawn from the uniform distributions presented in Table 8 with a normal copula coefficient -0.6.

Table 8 – Distributions of the silica nanoparticles parameters. Source: [19, 30]

Symbol	Parameter	Distribution
b_1 (mm^{-3})	Angular coef. of n_{max}	$\mathcal{U}(2054.82, 3008.78)$
b_2 (mm^{-3})	Linear coef. of n_{max}	$\mathcal{U}(269.30, 1335.86)$

The other parameters, inspired by the core-flood experiment presented in [44], are summarized in Table 2.

4.5 UNCERTAINTY PROPAGATION

To investigate how uncertainties propagate through the model, we calculate the mean, variance, confidence intervals, and prediction intervals for each QoI (the breakthrough time and water production). The last one was obtained by selecting the results within the 5th and 95th percentiles from the output distributions (90% prediction interval).

In order to obtain accurate results, we conducted a convergence analysis of the mean and the confidence bounds, increasing the size of samples from 10 to 2000; see Figs. 51 and 52. We perform 200 simulations, resulting in a total of 201000 calls to the model. Around the sample size 2000 convergence was achieved for all QoIs, so we use this value in the UQ studies below.

To analyze the impact of nanoparticle concentration on uncertainty propagation for the breakthrough time, we consider several concentration values ranging from 0.0% (without nanoparticles) to 1.0% (maximum amount of nanoparticles); see Fig. 53. The results show

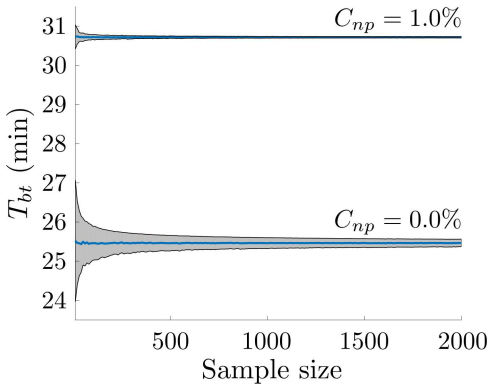

Figure 51 – Convergence analysis for the breakthrough time. We study the cases $C_{np} = 0.0\%$ (without nanoparticles) and $C_{np} = 1.0\%$ (maximum nanoparticle concentration). The blue central lines represent the mean, and the shaded regions correspond to the 95% confidence intervals.

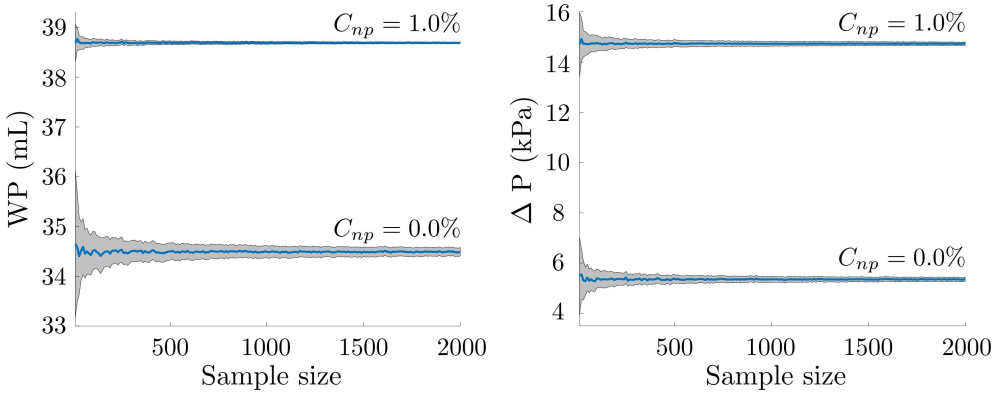

Figure 52 – Convergence analysis for the water production (left panel) and pressure drop (right panel), both at $t = 50$ min. We study the cases $C_{np} = 0.0\%$ (without nanoparticles) and $C_{np} = 1.0\%$ (maximum nanoparticle concentration). The blue central lines represent the mean, and the shaded regions correspond to the 95% confidence intervals.

a reduction in the model's uncertainties when nanoparticles are employed, indicating the stabilization potential of this technique. As expected, adding nanoparticles increases the breakthrough time, and this effect is less pronounced for high nanoparticle concentrations, aligned with [64]. To further investigate the significance of this phenomenon, we calculate the p-value, which is a statistical probability commonly used to measure the strength of evidence against a null hypothesis. In our case, we are testing the hypothesis that there is no significant difference between the model's output for the breakthrough time obtained for two different C_{np} values. The p-value ranges from 0 to 1, with 0 indicating that the observed results are impossible under the null hypothesis, while 1 indicates that the observed results are likely to occur by chance. As shown in Table 9, all of them can be considered null. Therefore, the effect of nanoparticle concentration in T_{bt} is statistically significant.

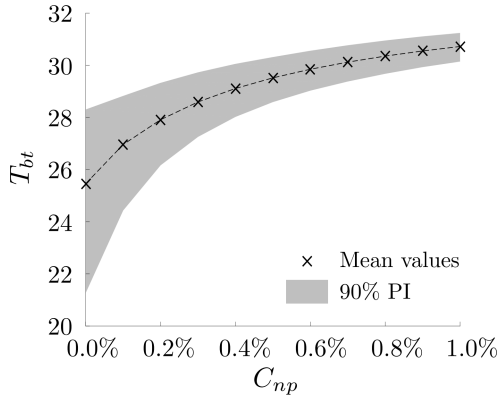

Figure 53 – Uncertainty quantification for the breakthrough time. We study several concentration values ranging from 0.0% (without nanoparticles) to 1.0% (maximum amount of nanoparticles). The markers represent the mean and the shaded region corresponds to the 90% prediction interval (90% PI).

Table 9 – Significance test for the difference in breakthrough time due to changes in nanoparticle concentration

C_{np} compared	p-value
$[0.0\%, 0.1\%]$	$3.222 \cdot 10^{-135}$
$[0.1\%, 0.2\%]$	$2.771 \cdot 10^{-133}$
$[0.2\%, 0.3\%]$	$4.600 \cdot 10^{-125}$
$[0.3\%, 0.4\%]$	$6.019 \cdot 10^{-114}$
$[0.4\%, 0.5\%]$	$1.309 \cdot 10^{-101}$
$[0.5\%, 0.6\%]$	$2.360 \cdot 10^{-89}$
$[0.6\%, 0.7\%]$	$5.578 \cdot 10^{-78}$
$[0.7\%, 0.8\%]$	$7.318 \cdot 10^{-68}$
$[0.8\%, 0.9\%]$	$4.345 \cdot 10^{-59}$
$[0.9\%, 1.0\%]$	$1.369 \cdot 10^{-51}$

To analyze the impact of nanoparticles on the uncertainties propagation for water production and pressure drop, we compare the cases $C_{np} = 1.0\%$ (maximum nanoparticle concentration) and $C_{np} = 0.0\%$ (without nanoparticles); as shown in Fig. 54. Since nanoparticles increase the breakthrough time, there is less water in the core compared with the case without nanoparticles at the same time. This leads to a reduction in both WP and ΔP uncertainties when nanoparticles are employed. The results also indicate that the WP with nanoparticles is larger than the other one, and the corresponding 90% prediction intervals do not intercept for a significant time interval (up to three breakthrough times); see the left panel in Fig. 54. Notice that WP curves will always intersect at large times, as proved in [64]. Furthermore, WP curves initially coincide because while the water saturation at the core's end is $S_R = 1.0$ the outflow rate remains constant; see Section 3.3 and Eq. (3.11). The pressure drop also increases due to the addition of nanoparticles; see the right panel in Fig. 54. Both cases (with and without nanoparticles) reach the maximum ΔP value at the breakthrough time, but this value is approximately three times

higher when nanoparticles are employed.

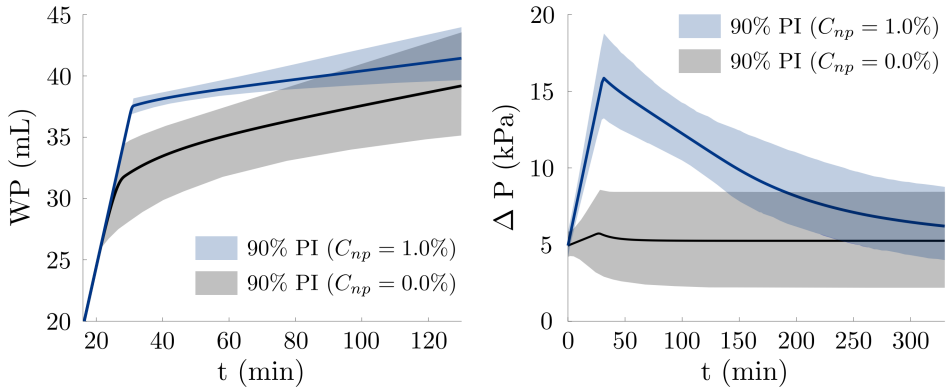

Figure 54 – Uncertainty quantification for the water production (left panel) and pressure drop (right panel) over time. We compare the cases $C_{np} = 1.0\%$ (maximum nanoparticle concentration) and $C_{np} = 0.0\%$ (without nanoparticles). The central lines represent the mean, and the shaded regions correspond to the 90% prediction interval (90% PI).

4.6 SENSITIVITY ANALYSIS

To perform the sensitivity analysis, we included the initial nanoparticle concentration as an uncertain input. We consider the uniform distribution $\mathcal{U}(0.7, 1.0)$, obtained from a mean of 0.85 and 10% for CV (the same adopted for endpoint relative permeabilities). We also perform a control test without nanoparticles. In this case, the set of uncertain inputs is composed only of $c_{k_{rg}}$, $c_{k_{rw}}$, and b_2.

The convergence of the sensitivity analysis considering the breakthrough time is presented in Figs. 55 (without nanoparticles) and 56 (with C_R as an uncertain input). We perform 200 simulations, increasing the size of samples from 40 to 8000. Convergence was achieved around 8000, so we use this sample size for the results presented in Fig. 57.

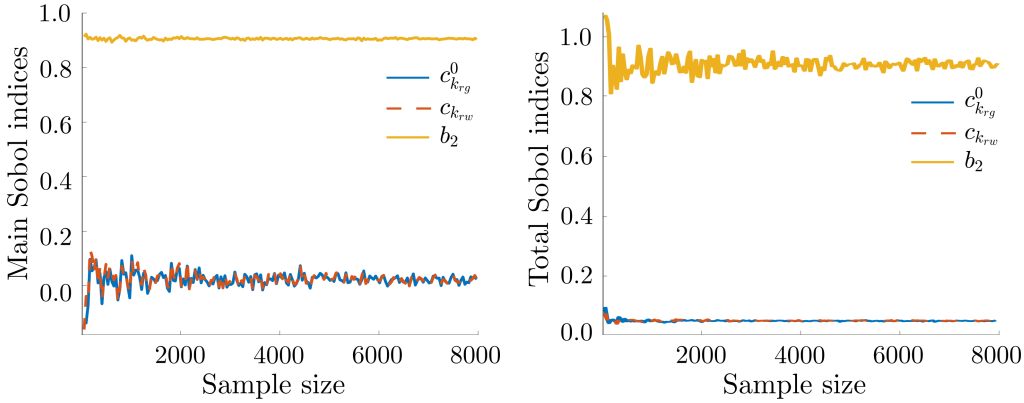

Figure 55 – Convergence of sensitivity analysis for the breakthrough time with $C_R = 0$. The left panel shows the main Sobol indices, and the right panel the total Sobol indices.

The left panel in Fig. 57 shows the Sobol indices for the T_{bt} with $C_R = 0$, where b_2 almost dominates the QoI. This was expected as it represents the maximum foam texture

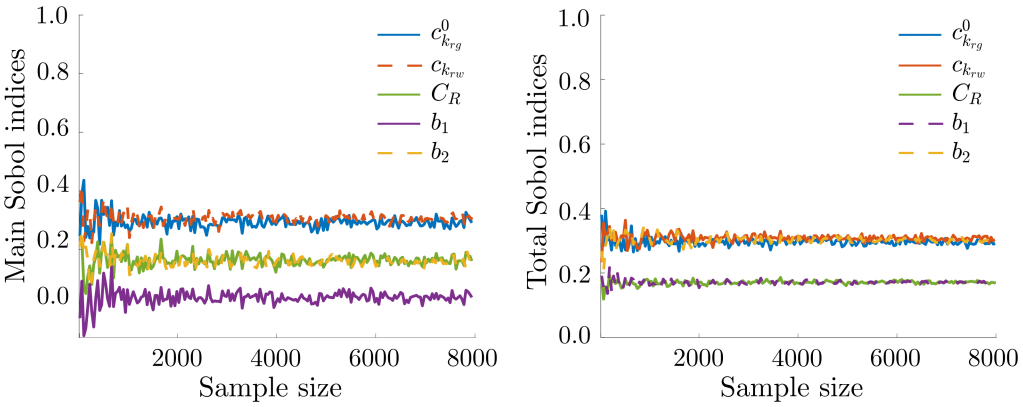

Figure 56 – Convergence of sensitivity analysis for the breakthrough time with C_R as uncertain input. The left panel shows the main Sobol indices, and the right panel the total Sobol indices.

without nanoparticles. The right panel of Fig. 57 shows the scenario where C_R is an uncertain input. We observe that the QoI sensitivity to the endpoint relative permeabilities becomes more relevant while b_2 decreases. Note that high-order interactions among the parameters, indicated by the total Sobol indices, were only observed with the presence of nanoparticles. This is due to the correlation between b_1 and b_2.

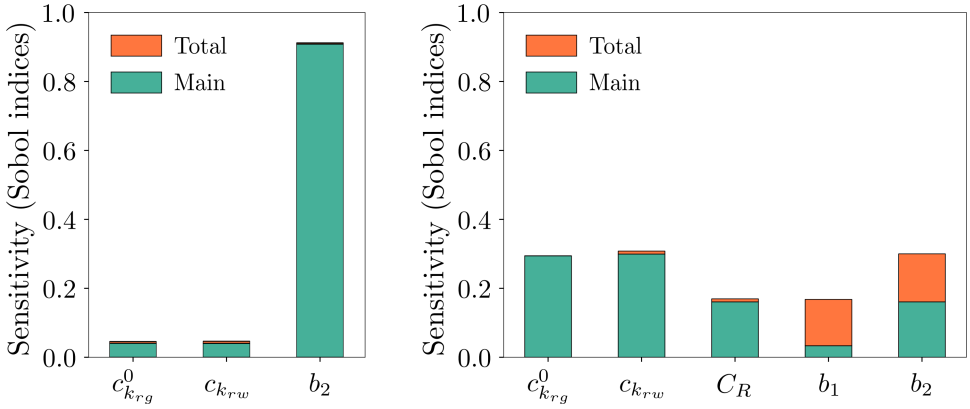

Figure 57 – Sensitivity analysis (Sobol indices) for the breakthrough time. The left panel shows the case without nanoparticles ($C_R = 0$), and the right panel shows the case with C_R as an uncertain input.

The convergence of the sensitivity analysis considering water production over time is presented in Figs. 58 (without nanoparticles) and 59 (with C_R as an uncertain input). Analogous to the previous study, we increased the size of samples from 40 to 8000, and the convergence was achieved. We use a sample size of 8000 for the results presented in Figs. 60 and 61. For both cases ($C_R = 0$ and C_R as an uncertain input), we begin calculating the Sobol indices at the breakthrough time, since WP curves coincide before that. We also consider a time interval where all waves composing the solution reach the end of the core.

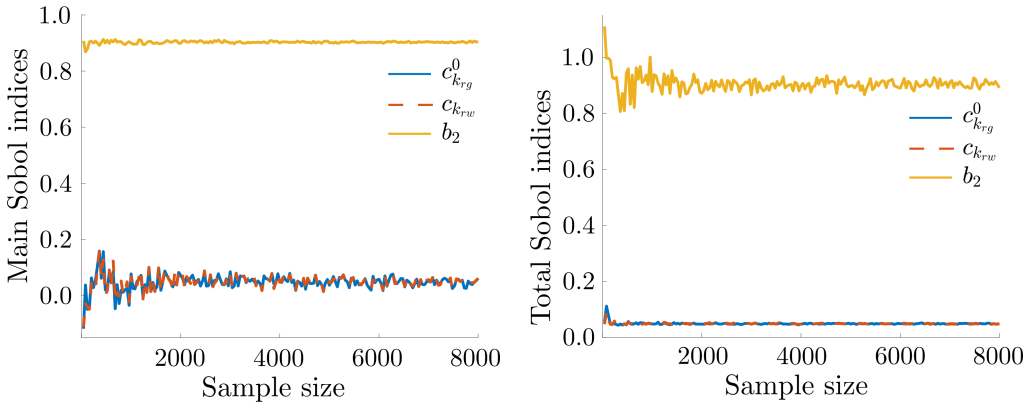

Figure 58 – Convergence of sensitivity analysis for water production at $t = 50$ min with $C_R = 0$. The left panel shows the main Sobol indices, and the right panel the total Sobol indices.

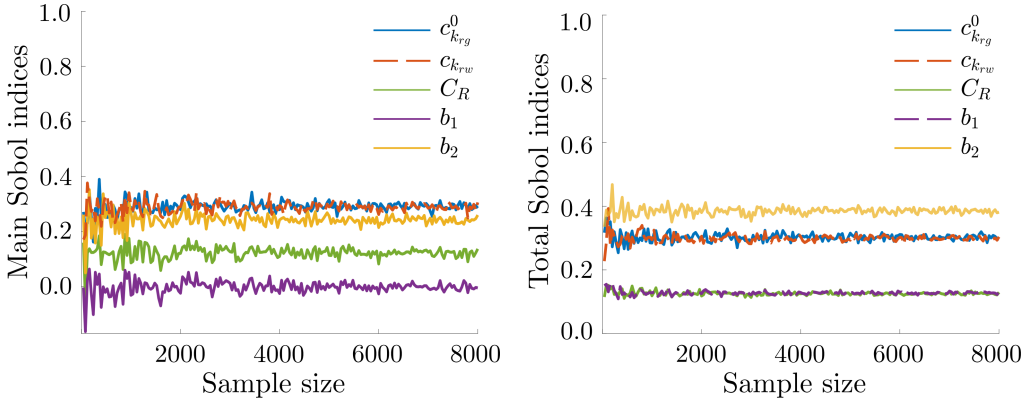

Figure 59 – Convergence of sensitivity analysis for water production at $t = 50$ min with C_R as uncertain input. The left panel shows the main Sobol indices, and the right panel the total Sobol indices.

Figure 60 shows that the model without nanoparticles is more sensitive to parameter b_2 for any time. In this case, there are no significant high-order interactions. Fig. 61 shows how the model's sensitivity changes over time in the presence of nanoparticles. By comparing the Sobol indices for the breakthrough time (right panel in Fig. 57), we observe that the sensitivity of WP to b_2 increases over time, while the sensitivity to other parameters decreases. At long times, as the WP curves coincide after the contact wave reaches the core end, the model's sensitivity to each parameter is very similar to the case without nanoparticles.

In the previous results for the T_{bt} and WP, it was observed that b_2 dominates the foam flow behavior in the absence of nanoparticles. Therefore, our next investigation focus only on the pressure drop sensitivity for the model with nanoparticles. We consider its maximum value ΔP_{max} (calculated at the breakthrough time for each sample) since this is a relevant parameter for practical applications. The convergence study considers 200 simulations, increasing the size of samples from 40 to 8000; see Fig. 62. Convergence was achieved around 8000, so we use this sample size for the results presented in Fig. 63. The

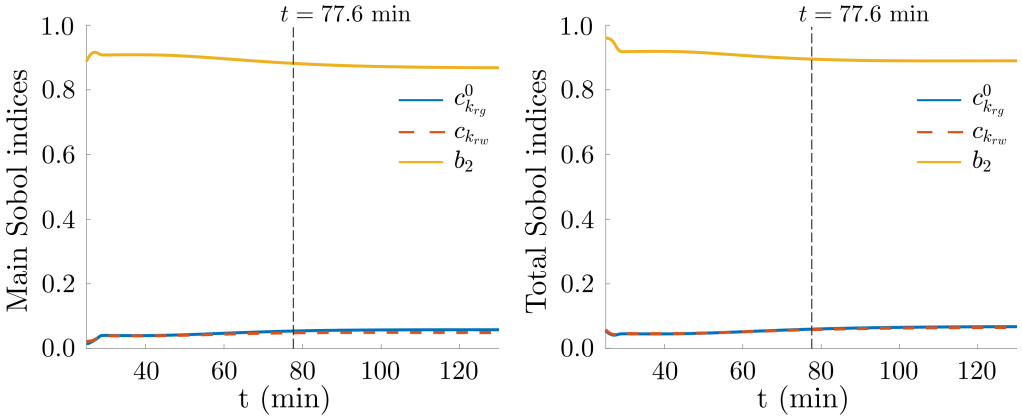

Figure 60 – Sensitivity analysis for the water production without nanoparticles ($C_R = 0$). The left panel shows the main Sobol indices and the right panel shows the total Sobol indices. The analysis begins at the breakthrough time (25.5 min), and the time when the rarefaction wave reaches the core's end is highlighted (77.6 min). These time values are calculated as an average for all samples, excluding particular cases where the S-wave is a shock.

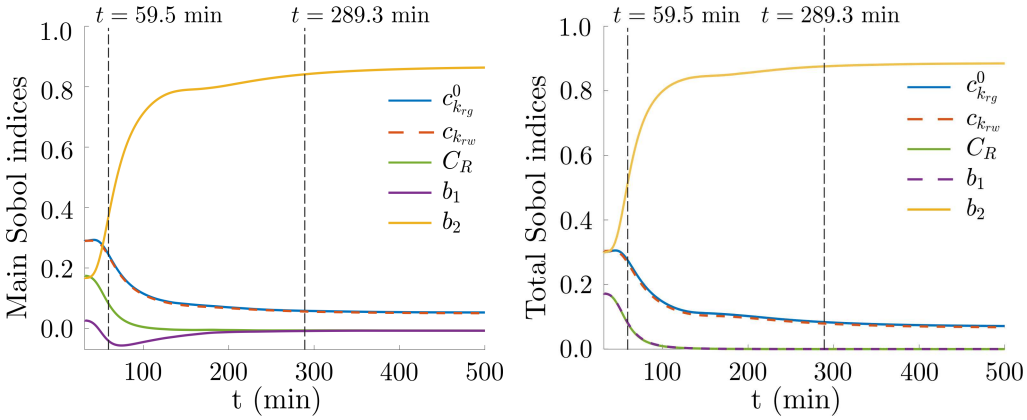

Figure 61 – Sensitivity analysis for the water production with C_R as an uncertain input. The left panel shows the main Sobol indices and the right panel shows the total Sobol indices. The analysis begins at the breakthrough time (30.4 min), and the time when the rarefaction and contact waves reach the reservoir's end is highlighted (59.5 and 289.3 min, resp.). These time values are calculated as an average for all samples, excluding particular cases where the S-wave is a shock.

analysis shows that ΔP_{max} is more sensitive to the gas endpoint relative permeability. However, C_R and b_2 are also relevant parameters. Furthermore, while the sensitivity to $c^0_{k_{rg}}$ and $c_{k_{rw}}$ was similar for the breakthrough time and water production, ΔP_{max} is much more sensitive to $c^0_{k_{rg}}$ than to $c_{k_{rw}}$. This occurs because most of the reservoir's initial content has already been swept at the moment of breakthrough. Consequently, gas mobility has a greater impact on total mobility.

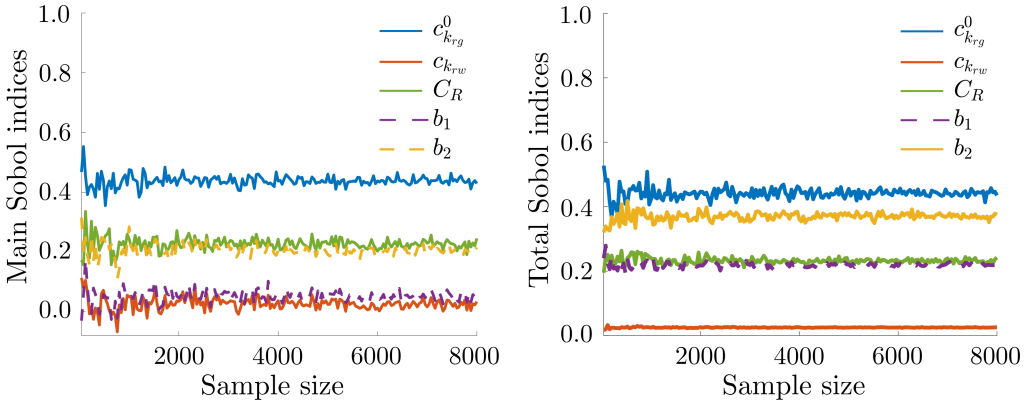

Figure 62 – Convergence of sensitivity analysis for the maximum pressure drop with C_R as an uncertain input. The left panel shows the main Sobol indices and the right panel shows the total Sobol indices.

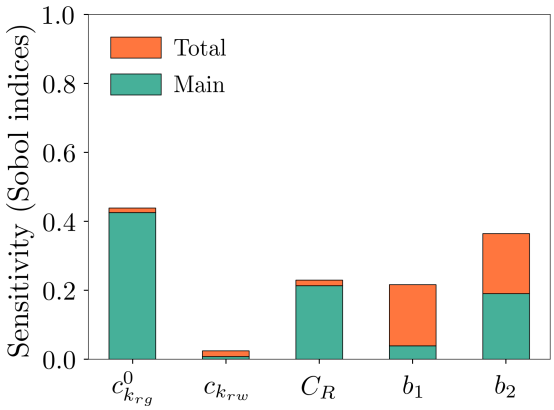

Figure 63 – Sensitivity analysis (Sobol indices) for the maximum pressure drop with C_R as an uncertain input.

4.7 DISCUSSION AND PARTIAL CONCLUSIONS

In this chapter, we simplified the NP-stabilized foam flow model proposed in Chapter 3 by using quadratic relative permeabilities to describe the water-gas fractional flow. Despite the simplification of the relative permeability model, the solution structure remains the same as the more realistic one. The proposed model allowed us to obtain algebraic expressions to analyze the solution type and construct the water saturation profiles, yielding performing an uncertainty quantification and sensitivity analysis study in a feasible time (drastically reducing computational costs). In particular, we achieved convergence for both UQ and SA, even using the Monte Carlo method, which is known to be computationally expensive. To the best of our knowledge, this is the first application of UQ and SA in the context of NP-stabilized foam.

Uncertainty quantification of the NP-stabilized foam model was performed for three quantities of interest (QoIs): breakthrough time, cumulative water production, and pressure drop. The developed analytical framework allowed us to obtain them all. Considering different values for nanoparticle concentration, as expected, we concluded that

adding nanoparticles increases the breakthrough time. This effect is less pronounced for high nanoparticle concentration. We also observed an increase in pressure drop with the addition of nanoparticles, with the maximum value increasing approximately three times compared to the case without nanoparticles. Our results showed that the water production with nanoparticles is larger than the other one, and the corresponding 90% prediction intervals do not intercept for a significant time interval (up to three breakthrough times). It indicates that measuring the effect of nanoparticles experimentally is statistically feasible.

We investigated the sensitivity of the same QoIs to the model's parameters. In this case, we included the nanoparticle concentration as an uncertain parameter. For the case without nanoparticles, the foam-related parameter dominates the breakthrough time and water production. For NP-stabilized foam, the breakthrough time sensitivity to the foam-related parameter decreased, and the endpoint relative permeabilities became more relevant. Over time, production's sensitivity to the foam-related parameter increased while the sensitivity to other parameters decreased. The maximum pressure drop was more sensitive to the gas endpoint relative permeability and the nanoparticle concentration.

5 NP-STABILIZED FOAM FLOW MODEL ACCOUNTING FOR RETENTION AND PERMEABILITY REDUCTION

In this chapter, we propose a mechanistic model describing NP-stabilized foam flow in porous media, accounting for nanoparticle retention and the resulting permeability reduction. The general assumptions for modeling NP-stabilized foam flow remain the same as in the previous chapters. However, we extend the model by incorporating the dynamics of bubble generation and coalescence, along with the inclusion of both suspended and retained nanoparticles.

Section 5.1 introduces the governing equations. In Section 5.2, we obtain a semi-analytical solution for this model under steady-state conditions. Section 3.3 presents the model calibration based on experimental data. Section 5.4 investigates the impact of nanoparticles on foam flow through solution profiles for water saturation, foam apparent viscosity, and pressure drop. In Section 5.6, we compare the steady-state model with a dynamic NP-stabilized foam flow model. In Section 5.7, we present discussions and partial conclusions based on the results presented in this chapter.

The results presented in this chapter are summarized in the paper [67].

5.1 GOVERNING EQUATIONS

We highlight that, in this chapter, we work directly with the dimensional system while maintaining simplified notation. Thus, x and t represent space and time (in units of length and time), and C denotes the nanoparticle concentration in wt%.

5.1.1 Nanoparticle transport models

Nanoparticles are expected to exhibit similar behavior to colloids (particles with diameters between 1 and 1000 nm) when they move through porous media [106]. As a result, some researchers have used colloid retention models to simulate the transport of nanoparticles in saturated columns [97, 106, 109, 139, 140], allowing them to interpret experimental data. Following the Colloid Filtration Theory (CFT) [48], the single-phase colloidal-suspension flow is modeled by considering advection, hydrodynamic dispersion, and deposition (filtration). At low particle concentrations and moderate ionic strength, the fluid-phase particle concentration $C(x,t)$ and retained particle concentration $\sigma(x,t)$ can be described by [48, 141]

$$\varphi\frac{\partial}{\partial t}(C+\sigma)+u\frac{\partial C}{\partial x}=D\frac{\partial^2 C}{\partial x^2}, \tag{5.1}$$

$$\frac{\partial \sigma}{\partial t}=\lambda(\sigma)uC, \tag{5.2}$$

where $u=u(t)$ is the flow velocity, λ is the filtration coefficient, and D is the hydrodynamic dispersion coefficient. Here, the suspended concentration is defined as the number (volume)

of particles per unit volume of the carrier fluid, while the retained concentration is defined as the number (volume) of particles per unit of the rock volume.

In many practical applications, the system (5.1)-(5.2) is typically analyzed at steady-state, where the effects of hydrodynamic dispersion are minimal and can be neglected [141]. It is commonly assumed that the particle deposition rate remains constant over time and space (λ is constant). Given these assumptions, initial conditions $C(x,0) = 0,\ \sigma(x,0) = 0$ and boundary condition $C(0,t) = C^I$, the solution of (5.1)-(5.2) is [142]

$$C(x,t) = C^I e^{-\lambda x}, \quad \sigma(x,t) = \lambda C^I (Ut - \varphi x) e^{-\lambda x}, \tag{5.3}$$

for $x < ut/\varphi$; otherwise, both concentrations C and σ vanish. Note that this model predicts that nanoparticle retention will continue to increase indefinitely as long as the dispersion concentration remains above zero. As a result, in a core-flooding experiment with continuous injection, the nanoparticle effluent concentration will not reach the injection concentration (even after the breakthrough).

The classical filtration model is based on the assumption of irreversible particle deposition, with no upper limit on filtration capacity. As more particles accumulate, the permeability gradually declines. A hyperbolic form is commonly assumed for the permeability reduction function, introduced in a modified form of Darcy's law as follows [142]

$$u = -\frac{k(\sigma)}{\mu}\frac{\partial P}{\partial x}, \quad k(\sigma) = \frac{k^0}{1+\theta\sigma}, \tag{5.4}$$

where μ is the water viscosity, P is the pressure, k^0 is the original permeability before injection, and $\theta > 0$ is the permeability-reduction coefficient.

Different models have been proposed modifying the CFT to include other phenomena, such as detachment, agglomeration, and even adsorption (retardation); for details, see [99, 143]. Due to the complexity of nanoparticle transport and experimental results reporting both reversible and irreversible particle capture, a mixed model, including mechanical retention and adsorption, seems to be the best way to model nanoparticle retention. However, there is still a lack of more rigorous studies, especially validation of mathematical models with reliable experimental data [102].

5.1.2 Foam flow with nanoparticles

Neglecting capillary effects ($p_w = p_g = P$), the foam transport is described by [13, 92]:

$$\varphi\frac{\partial}{\partial t}(S_g n) + \frac{\partial}{\partial x}(u_g n) = \Phi, \tag{5.5}$$

where n is the foam texture and the source term is $\Phi = \varphi S_g K_g(n_\infty - n)$; see Section 2.3 for details. Foam is a non-Newtonian fluid with apparent viscosity depending on the gas

velocity. We include the effect of nanoparticles on foam stabilization by increasing the foam's apparent viscosity, leading to lower mobility. Based on [93], we propose

$$\mu_{app} = \mu_g + \alpha(C) n u_g^d, \tag{5.6}$$

where μ_g is the foam-free gas viscosity and d is a constant related to the fluid viscosity. We assume α as a linear function $\alpha(C) = \alpha_1 C + \alpha_0$ depending on the nanoparticle concentration C in the aqueous phase.

Based on the CFT (see Eq. (5.1) and Eq. (5.2)) and following [33, 96] to include physicochemical adsorption, we propose the conservation law for nanoparticle transport as

$$\varphi \frac{\partial}{\partial t}(C S_w + \mathcal{A} + \sigma) + \frac{\partial}{\partial x}(C u_w) = 0, \tag{5.7}$$

where $\mathcal{A}$ is the concentration of nanoparticles adsorbed on the rock surface. Considering low suspension concentration, we use Henry's (linear) adsorption isotherm, i.e., $\mathcal{A} = \gamma C$. The nanoparticle capture rate is assumed to be proportional to the dispersion-free nanoparticles flux ($\partial\sigma/\partial t = \lambda(\sigma) C u_w$), and the filtration function is constant in time and space ($\lambda(\sigma) = \lambda$).

To model the fractional water-gas flow, we consider the original water and gas relative permeability functions k_{rw}^0 and k_{rg}^0 as described by Eq. (2.56) and Eq. (2.57). Since we introduced the effect of nanoparticles in the foam flow directly into the foam's apparent viscosity, the foam relative permeability function is assumed to be the same as that for free gas. However, the nanoparticles retained by mechanical entrapment change the relative permeabilities of each phase, which decrease monotonically with σ as [142]

$$k_{rw}(S_w, \sigma) = \frac{k_{rw}^0(S_w)}{(1 + \theta_w \sigma)}, \quad k_{rg}(S_w, \sigma) = \frac{k_{rg}^0(S_w)}{(1 + \theta_g \sigma)}, \tag{5.8}$$

where θ_w and θ_g are positive constants called permeability-reduction factors. Adsorption is considered low enough not to cause changes in permeability.

Consider the overall flux as the total superficial velocity of water and foam $u(t) = u_w + u_g$, which is independent of x due to the incompressibility of both phases. The water fractional flow function is defined as $f_w = u_w/u$. Following the introduction of the fractional flow theory for two-phase flow of non-Newtonian fluids [50], f_w becomes a function of the mobility ratio and the overall velocity, with

$$f_w = f_w(S_w, C, \sigma, u). \tag{5.9}$$

Therefore, the NP-stabilized foam flow is described by the following system of five unknowns

(S_w, C, P, n, and σ):

$$\varphi\frac{\partial S_w}{\partial t} + u\frac{\partial f_w}{\partial x} = 0, \tag{5.10}$$

$$u = -k\left(\frac{k_{rw}}{\mu_w} + \frac{k_{rg}}{\mu_{app}}\right)\frac{\partial P}{\partial x}, \tag{5.11}$$

$$\varphi\frac{\partial}{\partial t}[n(1-S_w)] + u\frac{\partial}{\partial x}[n(1-f_w)] = \varphi(1-S_w)K_g(n_\infty - n), \tag{5.12}$$

$$\varphi\frac{\partial}{\partial t}(CS_w + \mathcal{A} + \sigma) + u\frac{\partial}{\partial x}(Cf_w) = 0, \tag{5.13}$$

$$\frac{\partial \sigma}{\partial t} = \lambda(\sigma)uCf_w. \tag{5.14}$$

The initial conditions corresponding to the water-saturated core with no bubbles or particles are given by

$$C = 0, \quad \sigma = 0, \quad n = 0, \quad S_w = 1, \tag{5.15}$$

and inlet boundary conditions corresponding to the co-injection of a chemical solution (water with surfactant and nanoparticles) and gas are

$$C = C^I, \quad P = P^I, \quad n = 0. \tag{5.16}$$

5.2 STEADY-STATE SEMI-ANALYTICAL SOLUTION

The system composed of Eqs. (5.10) to (5.14) is quite complex to allow an analytical solution. Therefore, in this section, we study the steady-state case, with the flow velocities u_w and u_g independent of x. We divide this section into two parts. First, we investigate the foam flow model (without nanoparticles) at steady-state, presenting an analytical solution. Analogously, we study the NP-stabilized foam flow model, obtaining a semi-analytical solution.

5.2.1 Foam flow model at steady-state

Consider normalized water saturation $S = (S_w - S_{wc})/(1 - S_{wc})$. At steady-state and without nanoparticles, the Darcy velocities and bubble balance equation associated with the system of Eq. (5.10) to (5.14) are given by

$$u_w = -k\frac{c_{k_{rw}}S^\tau}{\mu_w}\frac{dP}{dx}, \tag{5.17}$$

$$u_g = -k\frac{c_{k_{rg}}(1-S)^{3+\frac{2}{\tau}}}{\mu_g + \alpha_0 n u_g^d}\frac{dP}{dx}, \tag{5.18}$$

$$\frac{dn}{dx} = \frac{\varphi}{u_g}(1-S_{wc})(1-S)K_g(n_\infty - n). \tag{5.19}$$

Let us consider the constant $A = (u_w\mu_w c_{k_{rg}})/(u_g c_{k_{rw}})$. The solution procedure follows four steps, as described next.

1. Equate pressure gradient from Eq. (5.17) and Eq. (5.18), to obtain an expression describing the foam texture:

$$n(x) = \frac{AS^{-\tau}(1-S)^{3+\frac{2}{\tau}} - \mu_g}{\alpha_0 u_g^d}. \tag{5.20}$$

2. Substitute Eq. (5.20) and its derivative in relation to x into Eq. (5.19), to obtain an expression for dS/dx:

$$\frac{dS}{dx} = \frac{[AS^{-\tau}(1-S)^{3+\frac{2}{\tau}} - \mu_g - \alpha u_g^d n_\infty](1-S)}{\tau S^{-\tau-1}(1-S)^{3+\frac{2}{\tau}} + \left(3+\frac{2}{\tau}\right) S^{-\tau}(1-S)^{2+\frac{2}{\tau}}} \frac{\varphi K_g (1-S_{wc})}{A u_g}. \tag{5.21}$$

3. Assuming that there is no bubble at the inlet ($n(0) = 0$), from Eq. (5.20) we obtain

$$S^{-\tau}(1-S)^{3+\frac{2}{\tau}} - \mu_g/A = 0. \tag{5.22}$$

   This is the transcendental equation for $S(x=0) = S^I$, allowing us to determine the inlet boundary condition for water saturation.

4. Distribution $n(x)$ is calculated by Eq. (5.20) for known profile $S(x)$. The pressure profile is obtained by

$$P(x) = P^I - \frac{u_w \mu_w}{k c_{k_{rw}}} \int_0^x S(x)^{-\tau} dx. \tag{5.23}$$

   Note that the solution $S(x)$ can be obtained by separation of variables

$$\int_{S^I}^{S(x)} \frac{1}{g(S)}\, dS = x, \tag{5.24}$$

where the function $g(S)$ is defined as the right side of Eq. (5.21).

5.2.2 NP-stabilized foam flow model at steady-state

Consider normalized water saturation $S = (S_w - S_{wc})/(1 - S_{wc})$. At steady-state, the Darcy velocities and bubble balance equation associated with the system of Eq. (5.10) to 5.14 are given by

$$u_w = -\frac{k c_{k_{rw}} S^\tau}{\mu_w (1+\theta_w \sigma)} \frac{dP}{dx}, \tag{5.25}$$

$$u_g = -\frac{k c_{k_{rg}} (1-S)^{3+\frac{2}{\tau}}}{[\mu_g + (\alpha_1 C + \alpha_0) n u_g^d](1+\theta_g \sigma)} \frac{dP}{dx}, \tag{5.26}$$

$$\frac{dn}{dx} = \frac{\varphi}{u_g}(1-S_{wc})(1-S) K_g (n_\infty - n). \tag{5.27}$$

Since we assume that adsorption only delays the front propagation of the nanoparticles, it does not impact this steady-state analysis.

According to the CFT, the solution for C and σ is given by Eq. (5.3); see [142] for details. As we are looking for the stationary solution, we approximate the retained nanoparticle concentration as

$$\sigma(x) = \Gamma C(x) = \Gamma C^I e^{-\lambda x}, \tag{5.28}$$

which is valid for a limited time. Since C varies along the core, we still consider mechanical entrapment, with the retained concentration changing with x.

Analogous to the previous case (Subsection **5.2.1**), the solution procedure follows four steps.

1. Equate pressure gradient from Eq. (5.25) and Eq. (5.26), to obtain an expression describing the foam texture:

$$n(x) = \frac{A\left(\dfrac{1+\theta_w\Gamma C^I e^{-\lambda x}}{1+\theta_g\Gamma C^I e^{-\lambda x}}\right)(1-S)^{3+\frac{2}{\tau}}S^{-\tau} - \mu_g}{(\alpha_1 C^I e^{-\lambda x} + \alpha_0)u_g^d}, \tag{5.29}$$

   where $A = (u_w\mu_w c_{k_{rg}})/(u_g c_{k_{rw}})$.

2. Substitute Eq. (5.29) and its derivative in relation to x into Eq. (5.27), to obtain an expression for dS/dx:

$$\begin{aligned}\frac{dS}{dx} = \; & -\left[\frac{\alpha_1 C^I e^{-\lambda x}+\alpha_0}{u_g^{-d}}\left(\frac{\alpha_1 C^I \lambda u_g^{-d} e^{-\lambda x}(\mu_g - AB(1-S))}{(\alpha_1 C^I e^{-\lambda x}+\alpha_0)^2}\right.\right. \\ & \left. - \frac{\varphi K_g(1-S_{wc})(S-1)}{u_g}\left(n_\infty + \frac{u_g^{-d}(\mu_g - AB(1-S))}{\alpha_1 C^I e^{-\lambda x}+\alpha_0}\right)\right) \\ & \left. + \frac{AB(1-S)\lambda e^{\lambda x}\Gamma(\theta_g-\theta_w)C^I}{(e^{\lambda x}+\Gamma\theta_w C^I)(e^{\lambda x}+\Gamma\theta_g C^I)}\right]\cdot\left[AB\left(\frac{1-S}{S}\tau + 3 + \frac{2}{\tau}\right)\right]^{-1},\end{aligned} \tag{5.30}$$

   where

$$B = B(x, S(x)) = \frac{(1-S)^{2+\frac{2}{\tau}}}{S^\tau}\left(\frac{e^{\lambda x}+\Gamma\theta_w C^I}{e^{\lambda x}+\Gamma\theta_g C^I}\right). \tag{5.31}$$

3. Assuming that there is no bubble at the inlet ($n(0) = 0$), from Eq. (5.29) we obtain

$$(1-S)^{3+\frac{2}{\tau}}S^{-\tau} - \frac{\mu_g}{A}\left(\frac{1+\theta_g\Gamma C^I}{1+\theta_w\Gamma C^I}\right) = 0, \tag{5.32}$$

   allowing us to determine the inlet boundary condition $S(x=0) = S^I$ for water saturation.

4. Distribution $n(x)$ is calculated by Eq. (5.29) for known profile $S(x)$. The pressure profile is obtained by

$$P(x) = P^I - \frac{u_w\mu_w}{k c_{k_{rw}}}\int_0^x (1+\theta_w\Gamma C)S^{-\tau}dx. \tag{5.33}$$

Note that the right side of Eq. (5.30) depends on x, so the solution $S(x)$ can not be obtained by separation of variables as in the previous case. Therefore, we find the saturation profile numerically.

5.3 MODEL SETUP

This section presents the results obtained by using the steady-state solution developed in Section 5.2. We use the ODE45 solver from Matlab to obtain the numerical water saturation profiles. Given the absence of comprehensive experimental data for NP-stabilized foam flow that would allow us to fit both the SBP and the nanoparticle retention model, we use different data for each part. Model setup is detailed below.

The physical parameters used to calibrate the SBP model are the same as those in Chapter 3; see Tables 2 and 3. The parameters related to the effect of nanoparticles on foam flow were obtained from the local equilibrium foam texture proposed in Section 3.1 (based on experimental data [19, 30]). Using that $n_{max}(C) = 2531.80C + 802.58$ mm^{-3}, for $0 \leq C \leq 1$ representing nanoparticle concentration between 0.0 and 1.0 wt% of the total aqueous phase, we adjust the models through the foam apparent viscosity adopting $n_\infty = 802.58$ mm^{-3}, $\alpha_0 = 5.8 \cdot 10^{-16}$ Pa·s$^{2/3}$m$^{10/3}$, and $\alpha_1 = (2531.80\alpha_0)/n_\infty$ Pa·s$^{2/3}$m$^{10/3}$. Table 10 summarizes the model parameters used in this chapter.

To calibrate the nanoparticle retention model, we follow [97], where a core-flooding experiment was conducted to investigate the transport of silica nanoparticles in dolomite rocks. The experiments were carried out on several core samples with a diameter of 3.8 cm, an average length of 10 cm, and absolute permeability ranging from 23 to 40 mD. Nanofluids with 0.1 and 0.5 wt% SiO_2 nanoparticle concentrations were tested with different ionic strengths and ion types (NaCl, $MgCl_2$). The experiment was analyzed using deep-bed filtration theory, yielding the filtration (λ) and the permeability-reduction (θ_w) coefficients under these varying conditions. In the present study, we only consider the variations in nanoparticle (NP) and salt concentrations, as shown in Table 11. We included two artificial nanofluids with $C^I = 1.0$ wt% (NF5 and NF6). Since this nanoparticle concentration was not experimentally investigated in [97], we use the same values of λ and θ_w obtained for $C^I = 0.5$ wt%. This assumption may slightly overestimate or underestimate the positive effect of nanoparticles on foam flow, as increasing concentration raises foam viscosity without altering retention-related parameters. Additional experimental data is needed for more accurate estimates.

Table 10 – Population balance NP-stabilized foam flow model parameters. Source: [30, 44]

Symbol	Parameter	Value
α_0 (Pa·s$^{2/3}$m$^{10/3}$)	Viscosity proportionality const.	$5.8 \cdot 10^{-16}$
α_1 (Pa·s$^{2/3}$m$^{10/3}$)	Viscosity proportionality const.	$1.83 \cdot 10^{-15}$
τ $(-)$	Pore-size-distribution parameter	5.0
$c_{k_{rg}}$ $(-)$	Gas endpoint relative perm.	1.0
$c_{k_{rw}}$ $(-)$	Water endpoint relative perm.	0.75
K_g (s^{-1})	Bubble generation rate	0.1
n_∞ (mm^{-3})	Equilibrium foam texture	802.58

Table 11 – Nanoparticle retention parameters. Source: [97]

Nanofluid	SiO_2 (wt%)	NaCl (ppm)	λ (m^{-1})	θ_w (−)
NF1	0.1	0	1.51	2013
NF2	0.1	50000	2.95	3269
NF3	0.5	0	1.86	1312
NF4	0.5	50000	5.33	913
NF5	1.0	0	1.86	1312
NF6	1.0	50000	5.33	913

Note that the permeability-reduction factor θ_w was obtained for a single-phase model in [97]. In two-phase models involving the injection of an aqueous solution with suspended particles into an oil reservoir, permeability reduction is typically considered only for the aqueous phase. However, in this study, we examine the co-injection (or alternate injection) of gas and an aqueous solution with surfactant and nanoparticles. In this scenario, the retained particles influence the relative permeability of both phases. To be more realistic, we assume that this impact varies between phases, with $\theta_g = 0.5\theta_w$ as the equivalent parameter for gas relative permeability. This hypothesis is based on the fact that the presence of non-wetting fluids leads to lower permeability reduction due to particle retention, as there is incomplete accessibility of the available surface and pores to particles transported by the water phase [110].

Additionally, we consider $\Gamma = 0.3\lambda\mathrm{L}$ to calculate the retained nanoparticle concentration. This value was chosen to align the simplified (steady-state) σ solution proposed by Eq. (5.28) with the classical (dynamic) CFT solution calculated by Eq. (5.3) at 2 injected pore volumes (PV); see Fig. 64, 65, and 66. Note that, in the absence of NaCl (NF1, NF3, and NF5), the decay in the suspended and retained concentration profiles is similar for all nanoparticle concentrations. However, with NaCl (NF2, NF4, and NF6), the decay becomes more pronounced as nanoparticle concentration increases.

The co-injection of the nanofluid and gas can lead to nanoparticle entrapment on the rock surface and in pores accessible to both aqueous and gaseous phases, thereby reducing the relative permeabilities of water and gas. By calculating k_{rw} and k_{rg} using Eq. (5.8), we obtain the curves presented in Fig. 67 for nanofluids without NaCl (NF1, NF3, and NF5) and with NaCl (NF2, NF4, and NF6). This figure also displays the original curves with no particle retention (equivalent to water injection without nanoparticles, i.e., $C^I = 0$). Note that, for both cases without and with NaCl, the water permeability-reduction coefficients decrease (or remain the same) as the injected nanoparticle concentration increases; see Table 11. Even so, the endpoints of $k_{rw}(S_w, \sigma)$ and $k_{rg}(S_w, \sigma)$ decrease with increasing C^I. This occurs because σ varies with C^I and λ. In addition, the presence of salt increases particle retention (see Fig. 64, 65, and 66), resulting in a greater reduction in gas relative permeability compared to the case without salt. That is, the endpoints of $c_{k_{rg}}$

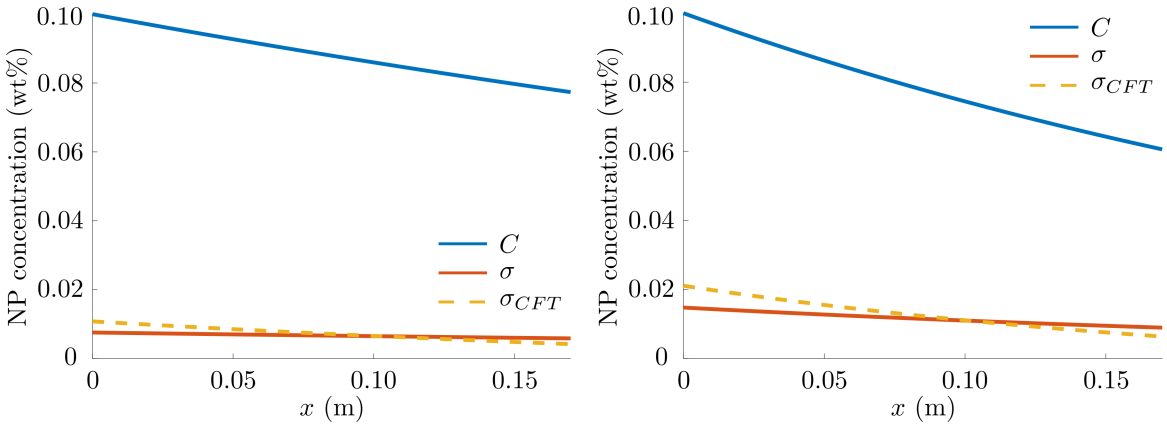

Figure 64 – Steady-state suspended (C) and retained (σ) nanoparticle concentration for NF1 (left panel) and NF2 (right panel), calculated by Eq. (5.28). The dashed lines show the dynamic retained nanoparticle concentration at 2 PVs following the CFT (σ_{CFT}), calculated by Eq. (5.3).

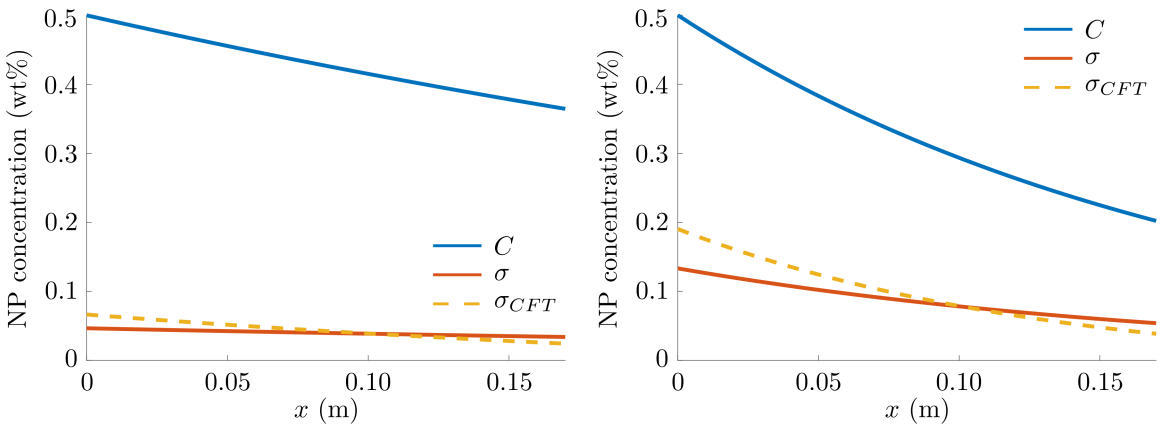

Figure 65 – Steady-state suspended (C) and retained (σ) nanoparticle concentration for NF3 (left panel) and NF4 (right panel), calculated by Eq. (5.28). The dashed lines show the dynamic retained nanoparticle concentration at 2 PVs following the CFT (σ_{CFT}), calculated by Eq. (5.3).

for NF2, NF4, and NF6 are much lower than for NF1, NF3, and NF5. As for the water relative permeability, the presence of salt is only significant for the lowest nanoparticle concentration (the endpoint of k_{rw} for NF2 is notably lower than for NF1).

5.4 IMPACT OF NANOPARTICLE RETENTION ON FOAM FLOW

The semi-analytical solution for NP-stabilized foam flow at steady-state, developed in Subsection **5.2.2**, allows us to obtain the water saturation, apparent viscosity, and pressure drop profiles for each nanofluid. To compare these results with foam flow (without nanoparticles), we use the steady-state analytical solution developed in Subsection **5.2.1**.

Before presenting the results for nanofluids 1-6, let us examine the effect of nanopar-

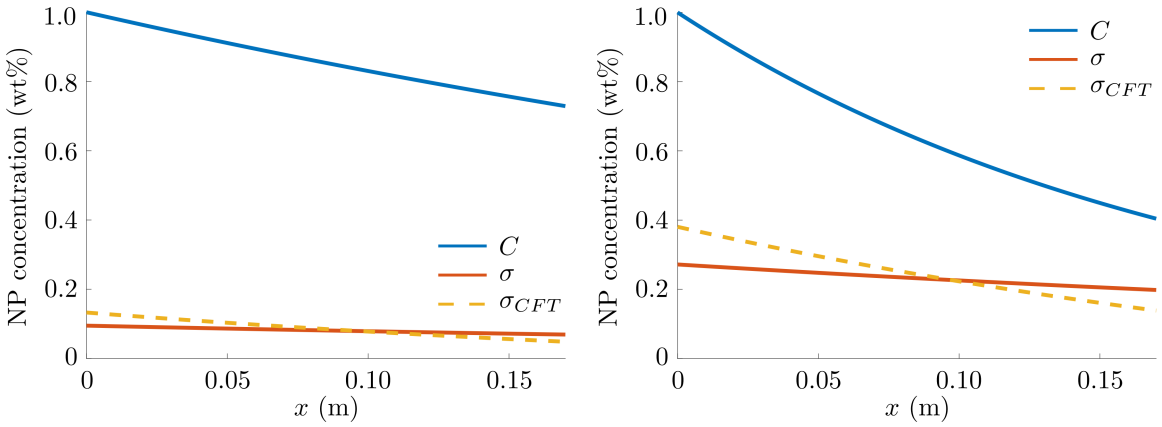

Figure 66 – Steady-state suspended (C) and retained (σ) nanoparticle concentration for NF5 (left panel) and NF6 (right panel), calculated by Eq. (5.28). The dashed lines show the dynamic retained nanoparticle concentration at 2 PVs following the CFT (σ_{CFT}), calculated by Eq. (5.3).

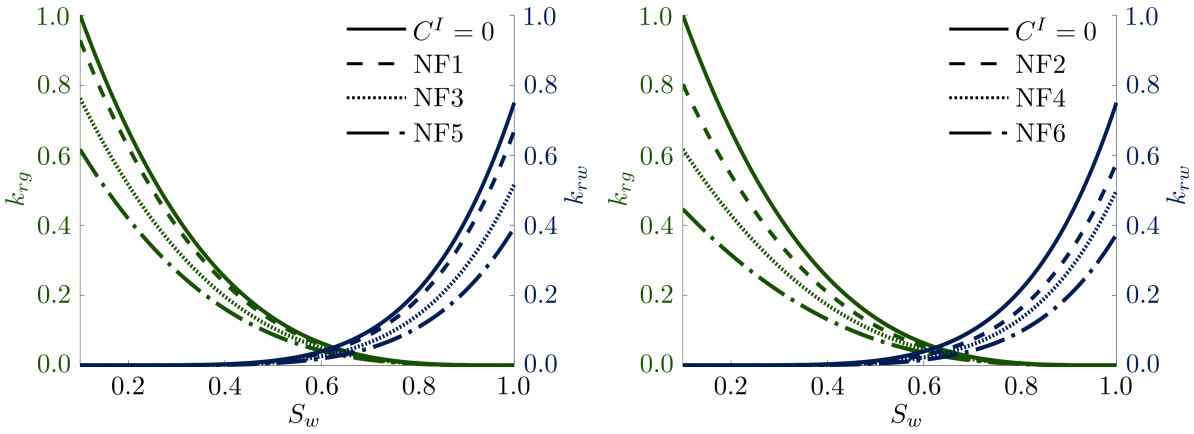

Figure 67 – Relative permeability curves for water (k_{rw}, blue curves) and gas (k_{rg}, green curves) after nanoparticle injection. The solid lines represent the case without nanoparticles. The left panel shows the relative permeability curves for nanofluids without NaCl, and the right panel shows the relative permeability curves for nanofluids with NaCl.

ticles on foam flow while neglecting particle retention (i.e., $\lambda = 0$). Fig. 68 shows the steady-state solution profiles for water saturation and foam apparent viscosity. Fig. 69 shows the steady-state pressure drop profiles, where $P_L = P(L)$ is the pressure at the core's end. The addition of nanoparticles increases the foam's apparent viscosity, resulting in a reduction in water saturation along the core and an increase in pressure drop. Moreover, this effect becomes more pronounced as the concentration of injected nanoparticles increases. Lower steady-state water saturation represents better sweeping efficiency since more water has been swept from the porous medium.

Now, let us analyze the complete model, taking into account particle retention for the case without NaCl (NF1, NF3, and NF5); see Figs. 70 and 71. From the saturation

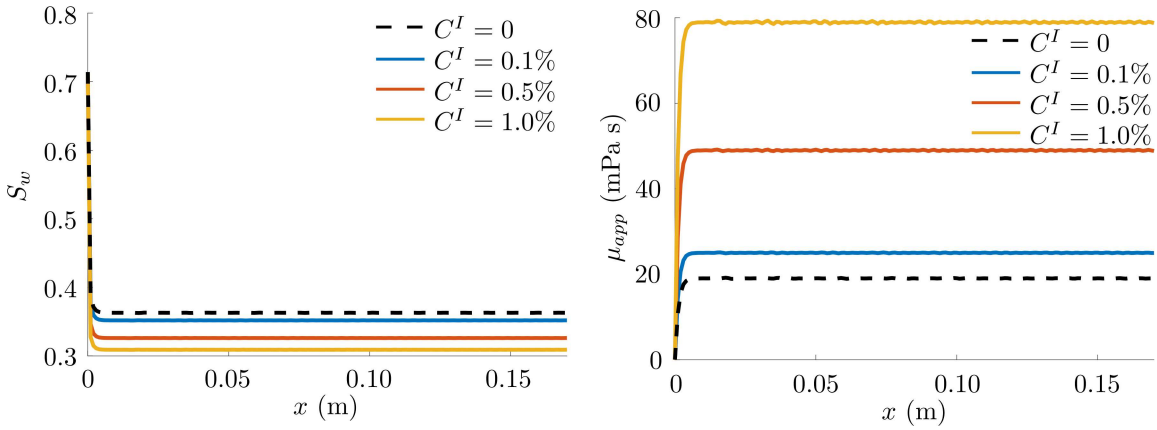

Figure 68 – Steady-state water saturation (left panel) and foam apparent viscosity (right panel) profiles. The solution profiles are presented for foam flow (without nanoparticles, $C^I = 0$) and NP-stabilized foam flow ($C^I = 0.1$, 0.5, and 1.0 wt%) neglecting particle retention ($\lambda = 0$).

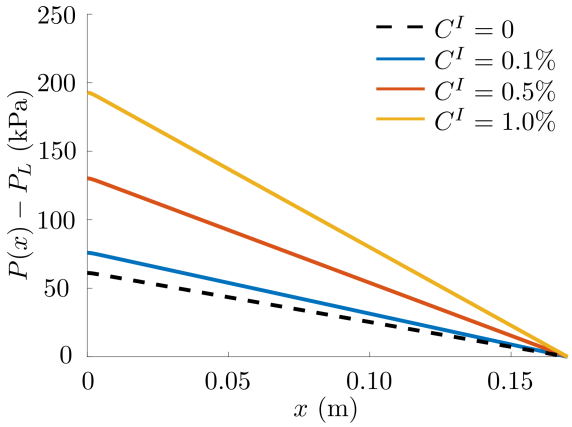

Nanofluid	ΔP (kPa)
$C^I = 0$	61.18
$C^I = 0.1\%$	75.89
$C^I = 0.5\%$	130.20
$C^I = 1.0\%$	192.77

Figure 69 – Steady-state pressure drop for foam flow (without nanoparticles, $C^I = 0$) and NP-stabilized foam flow ($C^I = 0.1$, 0.5, and 1.0 wt%) neglecting particle retention ($\lambda = 0$). The left panel shows the pressure drop profiles for $P(x) - P_L$, where $P_L = P(L)$ is the pressure at the core's end. The right panel shows the total pressure drop $\Delta P = P(0) - P_L$.

profiles, we observe that the water saturation along the core is slightly higher (for all nanofluids) compared to the case without retention. Additionally, there is a decay in the foam's apparent viscosity profiles, which intensifies as the core's end is approached. These two results are associated with the loss of nanoparticles due to retention, which reduces their effect on the foam's apparent viscosity and, consequently, reduces the sweep efficiency compared to the case without retention. On the other hand, the pressure drop shows a significant increase, which aligns with the reduction in relative permeabilities caused by the retained particles. For the case with NaCl (NF2, NF4, and NF6), the results are similar; see Figs. 72 and 73. However, as this case represents high ionic strength, nanoparticle retention is higher, leading to a more significant reduction in sweep efficiency and a more pronounced increase in pressure drop.

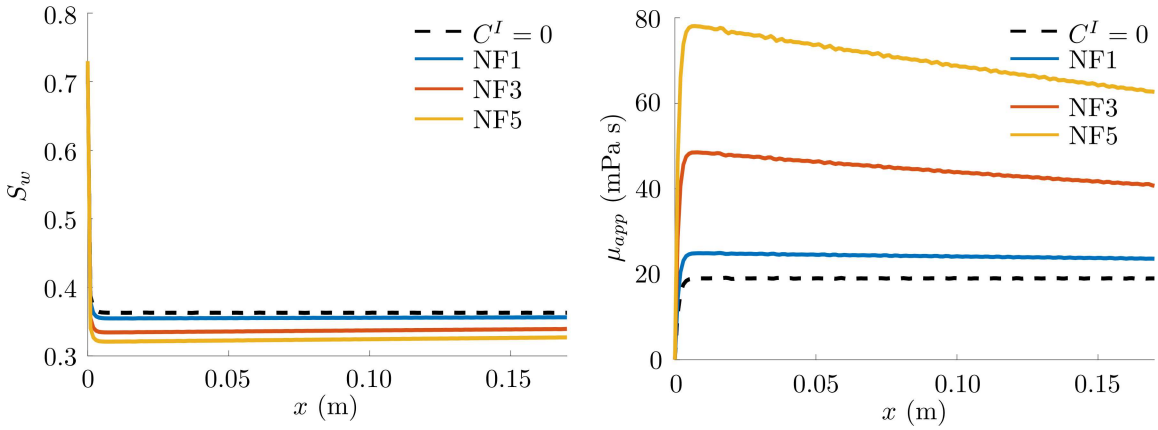

Figure 70 – Steady-state water saturation (left panel) and foam apparent viscosity (right panel) profiles. The solution profiles are presented for foam flow (without nanoparticles, $C^I = 0$) and NP-stabilized foam flow accounting for particle retention in the absence of NaCl (NF1, NF3, and NF5).

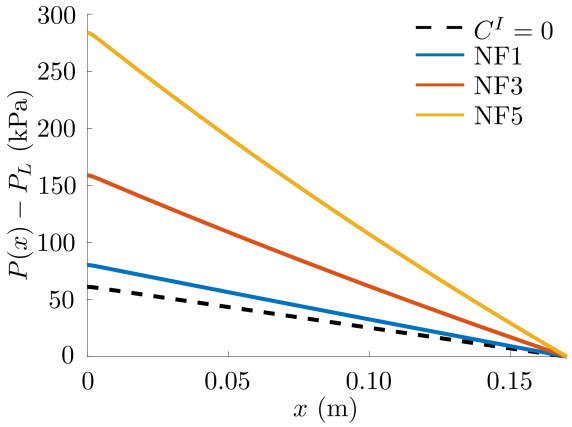

Nanofluid	ΔP (kPa)
$C^I = 0$	61.18
NF1	80.29
NF3	158.84
NF5	283.74

Figure 71 – Steady-state pressure drop for foam flow (without nanoparticles, $C^I = 0$) and NP-stabilized foam flow accounting for particle retention in the absence of NaCl (NF1, NF3, and NF5). The left panel shows the pressure drop profiles for $P(x) - P_L$, where $P_L = P(L)$ is the pressure at the core's end. The right panel shows the total pressure drop $\Delta P = P(0) - P_L$.

Remark 5.1. *Note that nanoparticle loss due to retention has a clear negative impact on foam flow, as it diminishes the positive effect of nanoparticles in increasing the foam's apparent viscosity. Conversely, analyzing the impact of the resulting permeability reduction is more complex. This reduction can lead to positive outcomes, such as reducing channeling (preferential paths), as well as negative consequences, such as a decline in injectivity. Opposite effects of permeability reduction can also be observed in the pressure drop, as detailed in Section 5.5 ahead.*

Remark 5.2. *In both laboratory and field tests, higher injection rates are required to maintain efficient foam flow as the foam's apparent viscosity increases. However, equipment*

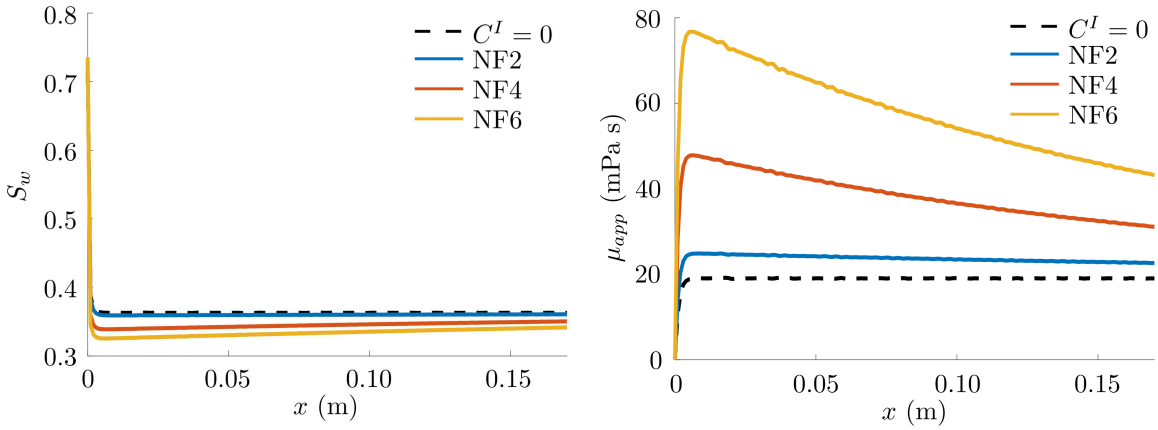

Figure 72 – Steady-state water saturation (left panel) and foam apparent viscosity (right panel) profiles. The solution profiles are presented for foam flow (without nanoparticles, $C^I = 0$) and NP-stabilized foam flow accounting for particle retention in the presence of NaCl (NF2, NF4, and NF6).

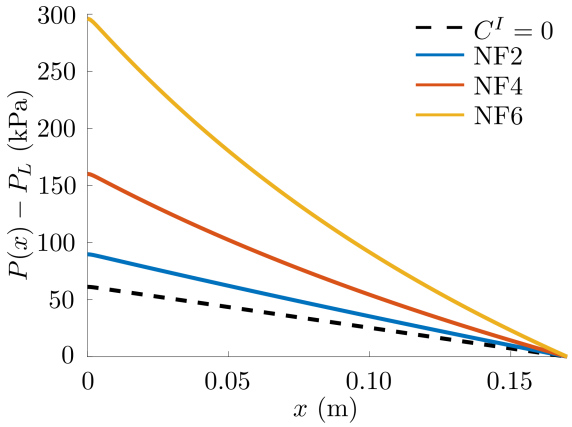

Nanofluid	ΔP (kPa)
$C^I = 0$	61.18
NF2	89.70
NF4	160.14
NF6	296.12

Figure 73 – Steady-state pressure drop for foam flow (without nanoparticles, $C^I = 0$) and NP-stabilized foam flow accounting for particle retention in the presence of NaCl (NF2, NF4, and NF6). The left panel shows the pressure drop profiles for $P(x) - P_L$, where $P_L = P(L)$ is the pressure at the core's end. The right panel shows the total pressure drop $\Delta P = P(0) - P_L$.

capacity and rock resistance impose a limit on the injection pressure. Thus, although the high-viscosity nature of foam solutions enhances reservoir sweep efficiency by controlling gas mobility, it reduces injectivity and can even make flow impossible. In this work, we do not establish an injection pressure limit or study injectivity decline. The NP-stabilized foam injection study presented here involves high pressure drop values (see Fig. 69, 71, and 73), which would be impractical for field applications; however, these pressure values are compatible with laboratory experiments.

5.5 INVESTIGATING EFFECTS OF RETENTION AND PERMEABILITY REDUCTION ON PRESSURE DROP

As shown in Section 5.4, when particle retention is neglected, nanoparticles improve the sweep efficiency of the porous medium by increasing the foam's apparent viscosity. This results in a lower steady-state water saturation and a higher pressure drop. However, when nanoparticle retention is considered, two effects occur: (i) the loss of suspended nanoparticles reduces their impact on μ_{app}, and (ii) the retained nanoparticles reduce the relative permeabilities. Mathematically, both effects lead to an increase in water saturation, which generally decreases the pressure drop compared to a model that neglects retention. Nevertheless, the reduction in permeability directly increases the pressure drop (see Eq. (5.33)). As a result, whether the pressure drop increases or decreases when considering particle retention depends on which of these opposing effects is more dominant.

To better understand the effects of particle retention on the pressure drop profiles, we study separately:

1. The impact of suspended nanoparticles loss, by comparing a model without retention (i.e., $\lambda = 0$) with a model with retention but no permeability reduction (i.e., $\theta_w = \theta_g = 0$).

2. The impact of suspended nanoparticles loss and permeability reduction, by comparing a model without retention with the complete model.

Figure 74 presents the pressure drop profiles for the nanofluids without NaCl (NF1, NF3, and NF5). In the left panel of Fig. 74, when only the loss of suspended nanoparticles is considered (solid lines), the pressure drop is lower compared to the case without retention (dashed lines). In the right panel of Fig. 74, when permeability reduction is also taken into account (solid lines), the pressure drop is higher compared to the case without retention (dashed lines), particularly for NF5 (highest nanoparticle concentration). For the nanofluids with salt (NF2, NF4, and NF6), the results are similar, as shown in Fig. 75. In this scenario, however, the loss of suspended nanoparticles due to retention is greater. Consequently, even when only this loss is considered, without accounting for permeability reduction, a significant difference in pressure drop for NF4 and NF6 is observed compared to the case without retention; see the left panel of Fig. 75.

Let us quantify the difference in the pressure drop when retention is considered, compared to the case $\lambda = 0$. By substituting $\sigma = \Gamma C$ from Eq. (5.28) into Eq. (5.33), and after some calculations, the difference between the total pressure drop considering particle retention (ΔP) and the total pressure drop neglecting particle retention ($\Delta P_{\lambda=0}$) can be

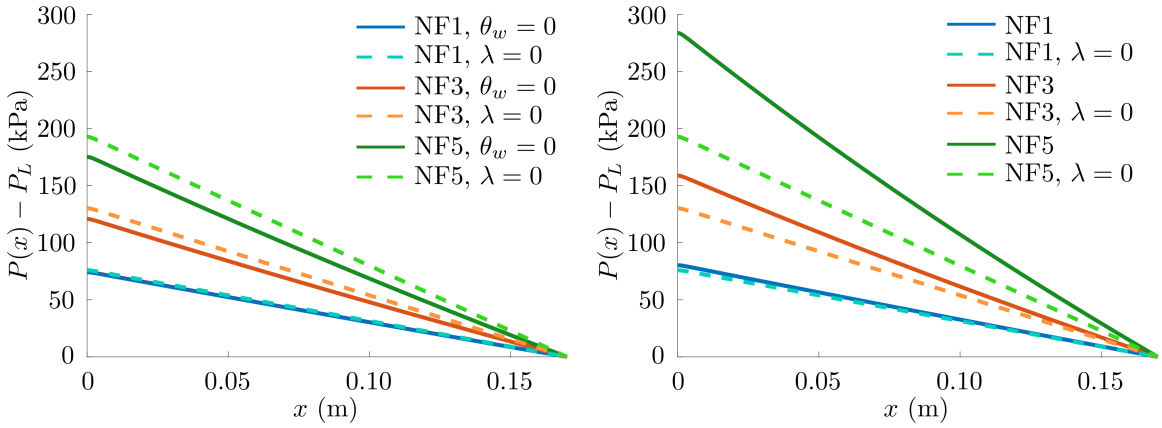

Figure 74 – Steady-state pressure drop profiles for NP-stabilized foam flow in the absence of NaCl (NF1, NF3, and NF5). The left panel compares the model without particle retention ($\lambda = 0$) with the model with retention but no permeability reduction ($\theta_w = 0$). The right panel compares the model without particle retention with the complete model.

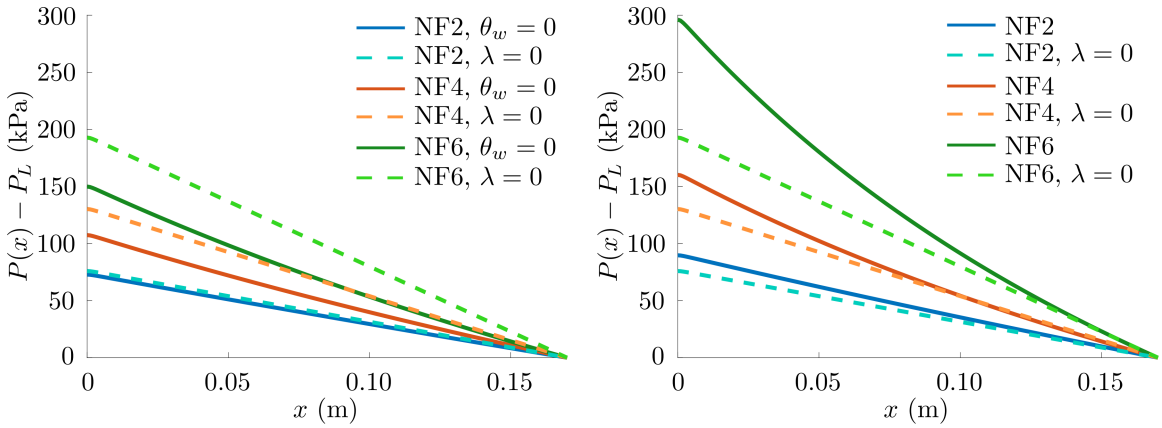

Figure 75 – Steady-state pressure drop profiles for NP-stabilized foam flow in the presence of NaCl (NF2, NF4, and NF6). The left panel compares the model without particle retention ($\lambda = 0$) with the model with retention but no permeability reduction ($\theta_w = 0$). The right panel compares the model without particle retention with the complete model.

written as

$$\Delta P - \Delta P_{\lambda=0} = \frac{u_w \mu_w}{k c_{k_{rw}}} \left[\theta_w \Gamma \int_0^L \frac{C}{S^\beta}\, dx + \int_0^L \left(\frac{1}{S^\beta} - \frac{1}{S^\beta_{\lambda=0}} \right) dx \right]. \tag{5.34}$$

Analogously, the pressure drop considering retention but with no permeability reduction ($\Delta P_{\theta_w=0}$) is given by

$$\Delta P_{\theta_w=0} - \Delta P_{\lambda=0} = \frac{u_w \mu_w}{k c_{k_{rw}}} \int_0^L \left(\frac{1}{S^\beta} - \frac{1}{S^\beta_{\lambda=0}} \right) dx. \tag{5.35}$$

Figure 76 presents the total pressure drop for each nanofluid in the three cases. The numbers on top of each bar indicate the relative difference in pressure drop compared to the no-retention model.

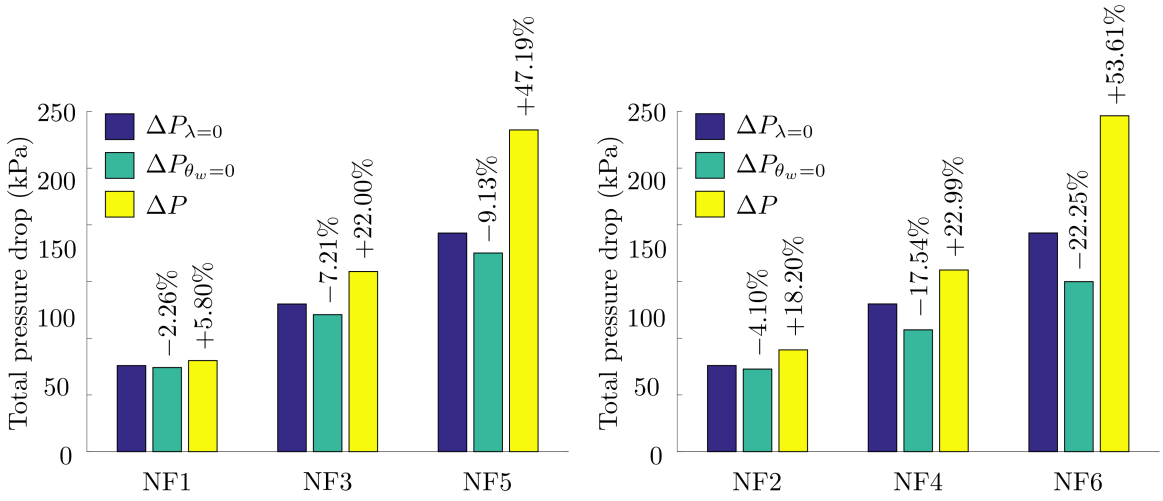

Figure 76 – Total pressure drop at steady-state for NP-stabilized foam flow with (left panel) and without (right panel) NaCl. We study the pressure drop: neglecting particle retention ($\Delta P_{\lambda=0}$), considering retention but with no permeability reduction ($\Delta P_{\theta_w=0}$), and considering both particle retention and permeability reduction (ΔP). The numbers on top of each bar indicate the pressure drop variation in relation to $\Delta P_{\lambda=0}$.

Since the presence of NaCl is associated with higher ionic strength and, consequently, greater retention, we expect that neglecting particle retention will have a more pronounced effect in this case. Indeed, when there is no permeability reduction, the variation in pressure drop $\Delta P_{\theta_w=0}$ relative to $\Delta P_{\lambda=0}$ is smaller for NF1 compared to NF2, for NF3 compared to NF4, and for NF5 compared to NF6. All these differences are negative, indicating the dominance of nanoparticle loss decreasing the pressure drop. When permeability reduction is considered, neglecting particle retention also has a more pronounced effect in the case of NaCl. Nevertheless, the variation in pressure drop ΔP relative to $\Delta P_{\lambda=0}$ is positive, indicating the dominance of permeability reduction increasing the pressure drop.

Based on our findings, models that neglect nanoparticle retention and those that account for retention but neglect permeability reduction underestimate the pressure drop. It is worth noting that if we consider the complete model to be closer to reality, the model that considers only nanoparticle loss results in pressure drop values further from the actual behavior than the model that entirely neglects the retention phenomenon. The differences between these pressure drop estimates increase with the ionic strength and the nanoparticle concentration. Nevertheless, due to the lack of experimental data for higher concentrations, we employed the same retention parameters for NF5 and NF6 as those used for NF3 and NF4, respectively. Thus, further investigation is necessary to validate our results.

5.6 COMPARING POPULATION BALANCE AND LOCAL EQUILIBRIUM MODELS UNDER STEADY-STATE CONDITIONS

Let us compare the steady-state model introduced in Section 5.2 with the dynamic NP-assisted foam flow model proposed in Chapter 3 (with the original relative permeability functions). In this local equilibrium model, particle retention was neglected. Therefore, to appropriately compare the results, we analyze Eq. (5.25)-(5.27) without retention ($\lambda = 0$), which yields a specific case of the solution developed in Subsection **5.2.2** for the complete system. In addition, we consider the dynamic model solution for large times after all waves have reached the core's end.

In this section, we will refer to the model proposed in this chapter as the PB (population balance) model and the one proposed in Chapter 3 as the LE (local equilibrium) model. For the PB model, the initial and boundary conditions are described by Eq. (5.15) and Eq. (5.16). For the LE model, in which we have only two unknowns (S_w and C), we also consider the core to be initially saturated with no particles ($S_w(x,0) = 1$, $C(x,0) = 0$) and with the same injected nanoparticle concentration ($C(0,t) = C^I$). However, the injected water saturation S_w^I is chosen as the saturation at the core outlet obtained by the PB model rather than being set as a boundary condition.

Figures 77 and 78 compare each model's water saturation, foam apparent viscosity, and pressure drop profiles at steady-state for $C^I = 1.0$ wt%. The blue and gray lines show results obtained with the same fluid velocities presented in Table 2 ($u_w = 1.45 \cdot 10^{-6}$ m/s and $u_g = 1.47 \cdot 10^{-5}$ m/s), while the red and yellow lines represent results for a higher gas velocity ($u_g = 3.0 \cdot 10^{-5}$ m/s). There is a good agreement between the results, even considering no bubbles at $x = 0$ in the PB model. That is, foam is generated very close to the core's inlet, and the bubble density can be well approximated by an equilibrium value n_∞. It is also possible to observe changes in the solution according to the foam velocity due to the non-Newtonian behavior of the foam.

To obtain the results of Figs. 77 and 78, we considered a high bubble generation rate ($K_g = 0.1$ s^{-1}). Figs. 79 and 79 show the solution for a lower value ($K_g = 0.02$ s^{-1}). In this case, the LE model does not describe the foam behavior as well at the core's inlet, since the foam is generated further along the core.

5.7 DISCUSSION AND PARTIAL CONCLUSIONS

In this chapter, we proposed a new mechanistic model for NP-stabilized foam flow in porous media, considering particle retention and the resulting permeability reduction. Analyzing the steady-state simplification of the model, we derived an analytical solution for the foam flow without nanoparticles and a semi-analytical solution for the complete case of foam assisted by nanoparticles. This solution allowed for the analysis of water

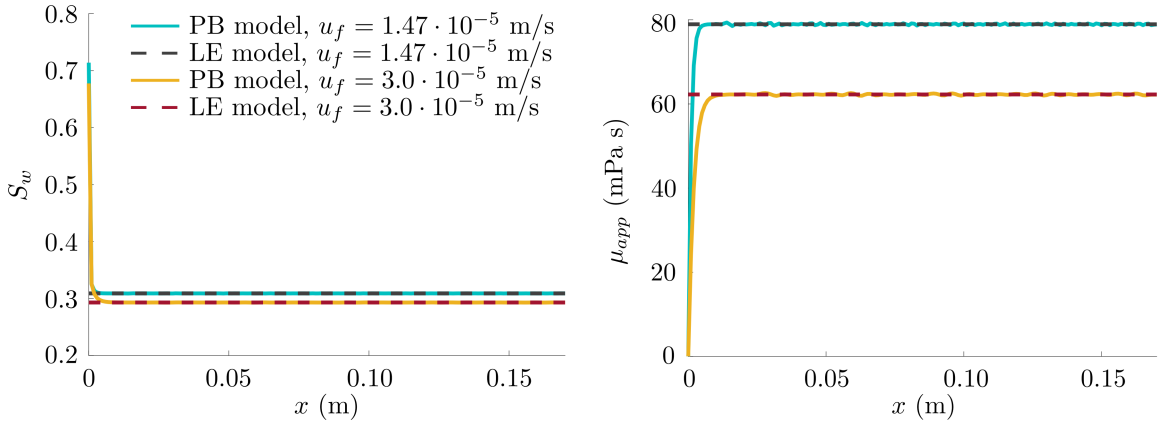

Figure 77 – Comparison between steady-state water saturation (left panel) and foam apparent viscosity (right panel) profiles for the population balance (PB) and local equilibrium (LE) models for $C^I = 1.0$ wt%. The results consider two foam velocities. Retention was neglected in the PB model ($\lambda = 0$) and $K_g = 0.1$ s^{-1}.

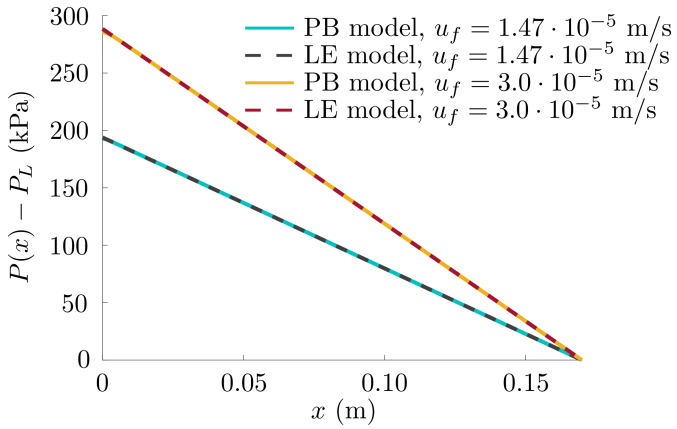

Figure 78 – Comparison between steady-state pressure drop profiles for the population balance (PB) and local equilibrium (LE) models for $C^I = 1.0$ wt%. The results consider two foam velocities. Retention was neglected in the PB model ($\lambda = 0$) and $K_g = 0.1$ s^{-1}.

saturation, foam apparent viscosity, and pressure drop profiles. Results were obtained for nanoparticle concentrations of 0.1, 0.5, and 1.0 wt%, both with and without NaCl, using retention parameters based on experimental data.

When comparing NP-stabilized foam with different nanoparticle concentrations, higher values lead to increased foam apparent viscosity, reducing steady-state water saturation and increasing pressure drop, thereby improving the sweep efficiency. Comparing foam flows with and without nanoparticles, taking retention into account, resulted in enhanced sweep efficiency only for higher nanoparticle concentrations (0.5 and 1.0 wt%). For 0.1 wt% the difference is insignificant.

Based on our findings, models that neglect nanoparticle retention and those that account for retention but neglect permeability reduction underestimate the pressure drop.

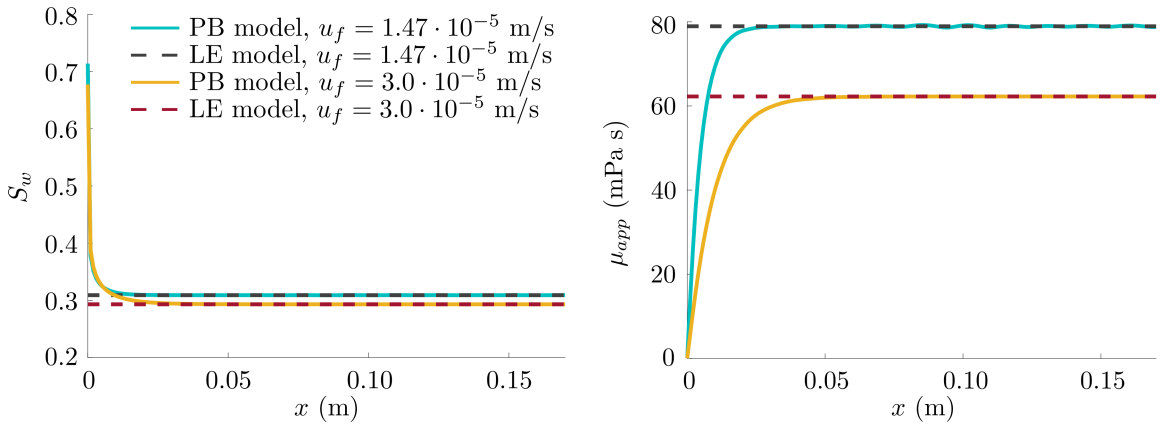

Figure 79 – Comparison between steady-state water saturation (left panel) and foam apparent viscosity (right panel) profiles for the population balance (PB) and local equilibrium (LE) models for $C^I = 1.0$ wt%. The results consider two foam velocities. Retention was neglected in the PB model ($\lambda = 0$) and $K_g = 0.02$ s^{-1}.

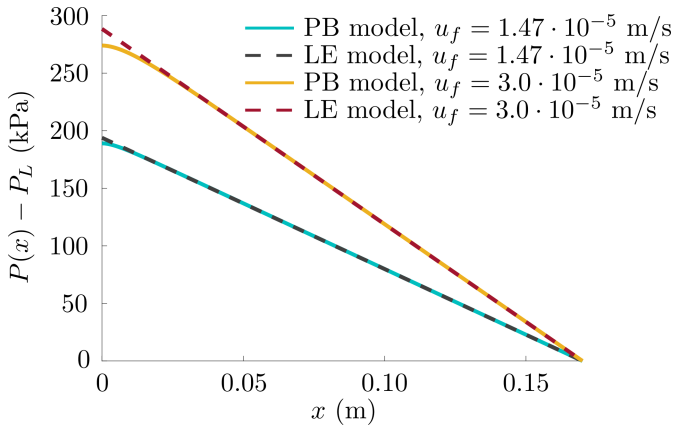

Figure 80 – Comparison between steady-state pressure drop profiles for the population balance (PB) and local equilibrium (LE) models for $C^I = 1.0$ wt%. The results consider two foam velocities. Retention was neglected in the PB model ($\lambda = 0$) and $K_g = 0.02$ s^{-1}.

The differences between these pressure drop estimates increase in scenarios with significant retention (e.g., in the presence of NaCl and high nanoparticle concentration). Considering retention, while retained nanoparticles increase pressure by reducing permeability, the loss of suspended nanoparticles decreases pressure by reducing the foam's apparent viscosity. Consequently, when considering both nanoparticle loss and reduced permeability, the pressure drop is higher than in models that ignore retention. In contrast, omitting retention effects on permeability lowers the pressure drop.

We also compared the semi-analytical steady-state solution for NP-stabilized foam flow developed in this chapter with a dynamic model solution (for large times). The comparison, neglecting particle retention, showed excellent agreement.

6 CONCLUDING REMARKS

In this thesis, we proposed two mathematical models for NP-stabilized foam flow in porous media: a local equilibrium (LE) model and a population balance (PB) model. In both cases, the flow dependence on nanoparticle concentration was formulated from the literature's experimental data. The LE model is simpler, allowing for a global analytical solution. The PB model is more complex and considers particle retention and permeability reduction; therefore, we provide a semi-analytical steady-state solution for this case. Each model solutions were used to analyze the effect of nanoparticles on foam flow, as detailed below.

The LE NP-stabilized foam flow model is a non-strictly hyperbolic system of conservation laws, solved for generic Riemann problem initial conditions. The mathematical solution changes qualitatively compared to the same model without nanoparticles due to a contact discontinuity that appears when the nanoparticle concentration changes. All analytical results are in good agreement with direct numerical simulations. Key industrial metrics, breakthrough time, and cumulative water production were derived using the analytical framework. Results show that higher nanoparticle concentrations increase foam stability and sweep efficiency, enhancing breakthrough time and water production during pure gas injection. However, this beneficial effect is less pronounced for high nanoparticle concentration, consistent with literature findings. Counterintuitively, for water-gas co-injection, nanoparticle addition can reduce breakthrough time under a specific parameter range with negligible impact on water production. Our results suggest that optimal conditions to observe enhanced water production in core-flooding experiments occur in partially saturated cores ($S_R \in [0.5, 0.6]$) and a co-injection water/gas ratio of up to 40/60% ($S_L \in [0, 0.4]$).

We also proposed a simplified LE model for NP-stabilized foam flow using quadratic Corey permeabilities. The solution structure remains the same as the more realistic model. This simplification enabled algebraic expressions for analyzing solution types and constructing water saturation profiles, facilitating an uncertainty quantification (UQ) and sensitivity analysis (SA) study with significantly reduced computational costs. Notably, convergence was achieved for both UQ and SA, even with the computationally intensive Monte Carlo method. We consider three quantities of interest (QoIs): breakthrough time, water production, and pressure drop.

As expected, adding nanoparticles increased breakthrough time, though the effect diminished at higher concentrations. Pressure drop also increased significantly with nanoparticles, reaching approximately three times the value observed without them. WP with nanoparticles was consistently higher, with non-overlapping 90% prediction intervals for up to three breakthrough times, demonstrating the statistical feasibility

of experimentally measuring nanoparticle effects. Sensitivity analysis revealed that for foam without nanoparticles, the foam-related parameter had the greatest influence on breakthrough time and WP. With nanoparticles, the breakthrough time sensitivity to the foam-related parameter decreased, and the endpoint relative permeabilities became more relevant. Over time, WP's sensitivity to the foam-related parameter increased while the sensitivity to other parameters decreased. The maximum pressure drop was most sensitive to gas endpoint relative permeability and nanoparticle concentration.

For the PB NP-stabilized foam flow model, we obtained a semi-analytical solution under steady-state conditions, simplifying to an analytic solution in the absence of nanoparticles. This framework enabled the analysis of water saturation, foam apparent viscosity, and pressure drop profiles for nanoparticle concentrations of 0.1, 0.5, and 1.0 wt%, with and without NaCl, using retention parameters derived from experimental data. Higher nanoparticle concentrations increased foam apparent viscosity, reducing steady-state water saturation and increasing pressure drop, which improved sweep efficiency. However, the comparison between foam flows with and without nanoparticles revealed enhanced sweep efficiency only for higher concentrations (0.5 and 1.0 wt%), while 0.1 wt% showed negligible differences. The semi-analytical solution aligned well with the solution for the dynamic LE model (for large times) when nanoparticle retention was neglected.

Incorporating nanoparticle retention revealed that the loss of suspended nanoparticles diminishes their positive effect on foam's apparent viscosity, while retained particles reduce permeability. Mathematically, these effects increase water saturation, generally leading to a lower pressure drop compared to models that ignore retention. Nevertheless, the reduction in permeability directly increases the pressure drop, so whether the pressure drop increases or decreases depends on which of these opposing effects is more dominant. Notably, models neglecting nanoparticle retention or omitting permeability reduction underestimate pressure drop. This underestimation becomes more pronounced in cases with significant retention, such as when NaCl is present or the nanoparticle concentration is high.

6.1 LIMITATIONS

The use of foam stabilized by nanoparticles for subsurface applications is still in the laboratory stage. This technique presents some limitations regarding the costs and technology involved in large-scale production [34]. It is important to note that while higher pressure gradients can lead to increased water production, excessively high values may result in injectivity loss. Therefore, determining the optimal nanoparticle concentration that effectively stabilizes foam without causing detrimental retention during displacement is a key challenge for NP-stabilized foam.

The specific limitation of this study is related to the lack of data on NP-stabilized

foam flow in porous media, particularly experiments with nanoparticle retention tests in the presence of a gaseous phase. We calibrated our models based on several literature experiments [19,22,44,120], so differences between the rocks in each experiment, in addition to other experimental conditions, can affect the reliability of the model's predictions.

Since foam flow assisted by nanoparticles is a recent area of study, there are only a few models available, and they are rarely validated against experimental data [144]. So far, we did not find any experiments in the literature that could be used for such a comparison. Advancing research in this direction depends on new core-flooding experiments with foam and nanoparticles, which are quite challenging. Observing the spatial propagation of foam front requires Micro Computational Tomography or numerous precision pressure measurement equipment, making these experiments time-consuming and costly. Analytical investigations, such as those discussed here, can assist in predicting flow behavior and optimizing the design of these experiments.

6.2 CONTRIBUTIONS

The development of the present work resulted in the following papers, presentations, and awards:

- **Full-length articles in journals:**

  DANELON, T. A.; PAZ, P. S.; CHAPIRO, G. The mathematical model and analysis of the nanoparticle-stabilized foam. **Appl. Math. Model.**, v. 125, p. 630-649, 2024.

  DANELON, T. A.; ROCHA, B. M.; SANTOS, R. W.; CHAPIRO, G. Sensitivity analysis and uncertainty quantification based on the analytical solution for nanoparticle-stabilized foam flow in porous media. **Geoenergy Sci. Eng.**, v. 242, p. 213285, 2024.

  DANELON, T. A.; FARAJZADEH, R.; BEDRIKOVETSKY, P.; CHAPIRO, G. Modeling nanoparticle-stabilized foam flow in porous media accounting for particle retention and permeability reduction. **To appear in Interpore Journal**, 2024.

- **Full-length paper in conference proceedings:**

  DANELON, T.; CHAPIRO, G. Análise de incertezas para escoamento em meios porosos de espuma estabilizada por nanopartículas. In: **Encontro Nacional de Modelagem Computacional**. Ilhéus, Brazil: Proceedings ENMC, 2024. p. 531–540.

CASCELLI, R. S. S.; SANTOS, T. F. C.; DANELON, T.; CHAPIRO, G. Modelagem matemática e computacional de subsidência em regiões afetadas pela dissolução de sal em Maceió/AL. In: **Encontro Nacional de Modelagem Computacional**. Ilhéus, Brazil: Proceedings ENMC, 2024. p. 521–530.

- **Conference oral presentations:**

  The mathematical model and analysis of the nanoparticle-stabilized foam. **16th InterPore Annual Meeting** & **Conference Courses (InterPore 2024)**, Qingdao, China, May 2024. Presented by T. DANELON.

  Análise de incertezas para escoamento em meios porosos de espuma estabilizada por nanopartículas. **XXVII Encontro Nacional de Modelagem Computacional (ENMC 2024)**, Ilhéus, BA/Brazil, Oct 2024. Presented by T. DANELON.

  Modelagem matemática e computacional de subsidência em regiões afetadas pela dissolução de sal em Maceió/AL. **XXVII Encontro Nacional de Modelagem Computacional (ENMC 2024)**, Ilhéus, BA/Brazil, Oct 2024. Presented by T. DANELON.

- **Awards:**

  Nomination to Best Student Paper Award by InterPore Journal for work presented at InterPore 2024.

  Honorable Mention in the Professor Francisco Duarte Moura Neto Award for work presented at ENMC 2024.

REFERENCES

1 WANG, S.; MULLIGAN, C. N. An evaluation of surfactant foam technology in remediation of contaminated soil. **Chemosphere**, Elsevier, v. 57, n. 9, p. 1079–1089, 2004.

2 HIRASAKI, G. J.; MILLER, C. A.; SZAFRANSKI, R.; LAWSON, J. B.; AKIYA, N. Surfactant/foam process for aquifer remediation. In: **International symposium on oilfield chemistry**. Houston, USA: SPE, 1997. p. 471–480.

3 PORTOIS, C.; BOEIJE, C. S.; BERTIN, H. J.; ATTEIA, O. Foam for environmental remediation: Generation and blocking effect. **Transp. Porous Media**, Springer, v. 124, n. 3, p. 787–801, 2018.

4 HU, J.; LAN, J. W.; CHEN, Y. M.; XU, W. J.; MENG, M.; MA, P. C.; KE, H. Foam flow model of municipal solid waste and its application in landfill gas pressure prediction. **J. Geotech. Geoenvironmental Eng.**, v. 149, n. 3, p. 04023004, 2023.

5 SHOJAEI, M. J.; OR, D.; SHOKRI, N. Localized delivery of liquid fertilizer in coarse-textured soils using foam as carrier. **Transp. Porous Media**, v. 143, n. 3, p. 787–795, 2022.

6 LYU, X.; VOSKOV, D.; ROSSEN, W. R. Numerical investigations of foam-assisted CO_2 storage in saline aquifers. **Int. J. Greenh. Gas Control.**, v. 108, p. 103314, 2021.

7 ROSSEN, W. R. Foams in enhanced oil recovery. In: PRUD'HOMME, R. K.; KHAN, S. (Ed.). **Foams: Theory, Measurements, and Applications**. New York: Marcel Dekker, 1996. v. 57, cap. 11, p. 414–464.

8 SUNMONU, R. M.; ONYEKONWU, M. Enhanced oil recovery using foam injection; a mechanistic approach. In: **Nigeria Annual International Conference and Exhibition**. Lagos, Nigeria: SPE, 2013.

9 FRAGA, C. T. C.; PINTO, A. C. C.; BRANCO, C. C. M.; PIZARRO, J. O. S.; PAULO, C. A. S. Brazilian pre-salt: An impressive journey from plans and challenges to concrete results. In: **Offshore Technology Conference**. Houston, USA: OTC, 2015.

10 GODOI, J. M. A.; MATAI, P. H. L. S. Enhanced oil recovery with carbon dioxide geosequestration: First steps at pre-salt in Brazil. **J. Pet. Explor. Prod. Technol.**, v. 11, p. 1429–1441, 2021.

11 HEMATPUR, H.; MAHMOOD, S. M.; NASR, N. H.; ELRAIES, K. A. Foam flow in porous media: Concepts, models and challenges. **J. Nat. Gas Sci. Eng.**, v. 53, p. 163–180, 2018.

12 EFTEKHARI, A. A.; FARAJZADEH, R. Effect of foam on liquid phase mobility in porous media. **Sci. Rep.**, v. 7, p. 43870, 2017.

13 ZITHA, P. L. J.; DU, D. X. A new stochastic bubble population model for foam flow in porous media. **Transp. Porous Media**, Springer, v. 83, n. 3, p. 603–621, 2010.

14 ASHOORI, E.; MARCHESIN, D.; ROSSEN, W. R. Roles of transient and local equilibrium foam behavior in porous media: Traveling wave. **Colloids Surf. A Physicochem. Eng. Asp.**, v. 377, p. 228–242, 2011.

15 CEDRO, J. B.; CHAPIRO, G. Traveling wave solutions for a realistic non-Newtonian foam flow model. **Geoenergy Sci. Eng.**, v. 232, p. 212478, 2024.

16 ROEBROEKS, J.; EFTEKHARI, A. A.; FARAJZADEH, R.; VINCENT-BONNIEU, S. Nanoparticle stabilized foam in carbonate and sandstone reservoirs. In: **18th European Symposium on IOR**. Dresden, Germany: EAGE, 2015.

17 ROGNMO, A.; HORJEN, H.; FERNø, M. Nanotechnology for improved CO_2 utilization in CCS: Laboratory study of CO_2-foam flow and silica nanoparticle retention in porous media. **Int. J. Greenh. Gas Control**, v. 64, p. 113–118, 2017.

18 ESPINOSA, D.; CALDELAS, F.; JOHNSTON, K.; BRYANT, S. L.; HUH, C. Nanoparticle-stabilized supercritical CO_2 foams for potential mobility control applications. In: **Improved Oil Recovery Conference**. Tulsa, USA: SPE, 2010. p. 129925.

19 SUN, Q.; LI, Z.; LI, S.; JIANG, L.; WANG, J.; WANG, P. Utilization of surfactant-stabilized foam for enhanced oil recovery by adding nanoparticles. **Energy Fuels**, v. 28, n. 4, p. 2384–2394, 2014.

20 LI, S.; LI, Z.; WANG, P. Experimental study of the stabilization of CO_2 foam by sodium dodecyl sulfate and hydrophobic nanoparticles. **Ind. Eng. Chem. Res.**, v. 55, n. 5, p. 1243–1253, 2016.

21 PÉREZ-GRAMATGES, A.; MAIA, C. B.; FREITAS, F. A. de; NASCIMENTO, M. A. C.; NASCIMENTO, R. S. V. Silica particles as surfactant nanocarriers for enhanced oil recovery. In: SHANKAR, S.; MULLER, R.; DUNNING, T.; CHEN, G. H. (Ed.). **Computational Materials, Chemistry, and Biochemistry: From Bold Initiatives to the Last Mile**. Switzerland: Springer Cham, 2021. cap. 22, p. 503–519.

22 YEKEEN, N.; IDRIS, A. K.; MANAN, M. A.; SAMIN, A. M.; RISAL, A. R.; KUN, T. X. Bulk and bubble-scale experimental studies of influence of nanoparticles on foam stability. **Chin. J. Chem. Eng.**, v. 25, n. 3, p. 347–357, 2017.

23 ROGNMO, A. U.; AL-KHAYYAT, N.; HELDAL, S.; VIKINGSTAD, I.; EIDE, Ø.; FREDRIKSEN, S. B.; ALCORN, Z.; GRAUE, A.; BRYANT, S.; KOVSCEK, A. R.; FERNO, M. A. Performance of silica nanoparticles in CO_2 foam for EOR and CCUS at tough reservoir conditions. **SPE J.**, v. 25, n. 1, p. 406–415, 2020.

24 FAÇANHA, J. M.; LOPES, L. F.; FRITIS, G.; GODOY, P.; SANTOS, R. W. dos; CHAPIRO, G.; PÉREZ--GRAMATGES, A. Bubble-growth regime for confined foams: Comparison between N_2-CO_2/foam and CO_2/foam stabilized by silica nanoparticles. **J. Pet. Sci. Eng.**, Elsevier, v. 218, p. 111006, 2022.

25 YEKEEN, N.; MANAN, M. A.; IDRIS, A. K.; PADMANABHAN, E.; JUNIN, R.; SAMIN, A. M.; GBADAMOSI, A. O.; OGUAMAH, I. A comprehensive review of experimental studies of nanoparticles-stabilized foam for enhanced oil recovery. **J. Pet. Sci. Eng.**, v. 164, p. 43–74, 2018.

26 ISSAKHOV, M.; KHANJANI, M.; MURATKHOZHINA, A.; POURAFSHARY, P.; AIDAROVA, S.; SHARIPOVA, A. Experimental and data-driven analysis for predicting nanofluid performance in improving foam stability and reducing mobility at critical micelle concentration. **Sci. Rep.**, v. 14, n. 7856, 2024.

27 BENNETZEN, M. V.; MOGENSEN, K. Novel applications of nanoparticles for future enhanced oil recovery. In: **International Petroleum Technology Conference**. Kuala Lumpur, Malaysia: IPTC, 2014.

28 SINGH, R.; MOHANTY, K. K. Synergy between nanoparticles and surfactants in stabilizing foams for oil recovery. **Energy Fuels**, v. 29, n. 2, p. 467–479, 2015.

29 RAHMAN, A.; TORABI, F.; SHIRIF, E. Surfactant and nanoparticle synergy: Towards improved foam stability. **Petroleum**, v. 9, n. 2, p. 255–264, 2023.

30 DU, D.; ZHAO, D.; LI, F. W. Y.; LI, J. Parameter calibration of the stochastic bubble population balance model for predicting NP-stabilized foam flow characteristics in porous media. **Colloids Surf. A Physicochem. Eng. Asp.**, v. 614, p. 126180, 2021.

31 DARYASAFAR, A.; SHAHBAZI, K. Using nanotechnology for co_2-foams stabilization for application in enhanced oil recovery. **Int. J. Energy a Clean Environ.**, v. 19, p. 217–235, 2018.

32 YU, H.; KOTSMAR, C.; YOON, K. Y.; INGRAM, D. R.; JOHNSTON, K. P.; BRYANT, S. L.; HUH, C. Transport and retention of aqueous dispersions of paramagnetic nanoparticles in reservoir rocks. In: **Improved Oil Recovery Conference**. Tulsa, USA: SPE, 2010. p. 129887.

33 FARAJZADEH, R.; BEDRIKOVETSKY, P.; LOTFOLLAHI, M.; LAKE, L. W. Simultaneous sorption and mechanical entrapment during polymer flow through porous media. **Water Resour. Res.**, v. 52, n. 3, p. 2279–2298, 2016.

34 AGI, A.; JUNIN, R.; GBADAMOSI, A. Mechanism governing nanoparticle flow behaviour in porous media: Insight for enhanced oil recovery applications. **Int. Nano Lett.**, v. 8, p. 49–77, 2018.

35 KOVSCEK, A. R.; RADKE, C. J. Fundamentals of foam transport in porous media. In: SCHRAMM, L. L. (Ed.). **Foams: Fundamentals and Applications in the Petroleum Industry**. Washington, DC: American Chemical Society, 1994. cap. 3, p. 115–163.

36 MARSDEN, S. S. **Foams in porous media**. Stanford, USA, 1986.

37 KAM, S. I. Improved mechanistic foam simulation with foam catastrophe theory. **Colloids Surf. A Physicochem. Eng. Asp.**, v. 318, n. 1, p. 62–77, 2008.

38 KOVSCEK, A. R.; PATZEK, T. W.; RADKE, C. J. A mechanistic population balance model for transient and steady-state foam flow in Boise sandstone. **Chem. Eng. Sci.**, v. 50, n. 23, p. 3783–3799, 1995.

39 TANG, J.; CASTAÑEDA, P.; MARCHESIN, D.; ROSSEN, W. R. Three-phase fractional-flow theory of foam-oil displacement in porous media with multiple steady states. **Water Resour. Res.**, Wiley Online Library, v. 55, n. 12, p. 10319–10339, 2019.

40 EIDE, Ø.; FERNØ, M.; BRYANT, S.; KOVSCEK, A.; GAUTEPLASS, J. Population-balance modeling of CO_2 foam for CCUS using nanoparticles. **J. Nat. Gas Sci. Eng.**, v. 80, p. 103378, 2020.

41 LI, Q.; PRIGIOBBE, V. Modeling nanoparticle transport in porous media in the presence of a foam. **Transp. Porous Media**, v. 131, n. 1, p. 269–288, 2020.

42 LI, Q.; PRIGIOBBE, V. Measuring and modeling nanoparticle transport by foam in porous media. **J. Contam. Hydrol.**, v. 243, p. 103881, 2021.

43 SIMJOO, M.; ZITHA, P. L. J. Modeling of foam flow using stochastic bubble population model and experimental validation. **Transp. Porous Media**, Springer, v. 107, n. 3, p. 799–820, 2015.

44 SIMJOO, M.; DONG, Y.; ANDRIANOV, A.; TALANANA, M.; ZITHA, P. L. J. Novel insight into foam mobility control. **SPE J.**, Soc. Pet. Eng., v. 18, n. 3, 2013.

45 KAM, S. I.; NGUYEN, Q. P.; LI, Q.; ROSSEN, W. R. Dynamic simulations with an improved model for foam generation. **SPE J.**, Soc. Pet. Eng., v. 12, n. 1, p. 35–48, 2007.

46 LEVEQUE, R. J. **Numerical methods for conservation laws**. Basel: Birkhäuser Basel, 1990.

47 SMOLLER, J. **Shock waves and reaction-diffusion equations**. New York: Springer Science & Business Media, 2012.

48 HERZIG, J. P.; LECLERC, D. M.; GOFF, P. L. Flow of suspensions through porous media—application to deep filtration. **Ind. Eng. Chem. Res.**, v. 62, n. 5, p. 8–35, 1970.

49 SHARMA, M. M.; YORTSOS, Y. C. Transport of particulate suspensions in porous media: Model formulation. **AIChE Journal**, v. 33, n. 10, p. 1636–1643, 1987.

50 BEDRIKOVETSKY, P. **Mathematical Theory of Oil and Gas Recovery**: With applications to ex-USSR oil and gas fields. Dordrecht: Springer Science & Business Media, 1993. (Petroleum Engineering and Development Studies).

51 SUDRET, B.; MARELLI, S.; WIART, J. Surrogate models for uncertainty quantification: An overview. In: **11th European Conference on Antennas and Propagation**. Paris, France: EurAAP, 2017. p. 793–797.

52 SUDRET, B. Meta-models for structural reliability and uncertainty quantification. In: **Asian-Pacific Symposium on Structural Reliability and its Applications**. Singapore: HAL, 2012. p. 1–24.

53 CIRIELLO, V.; Di Federico, V. Similarity solutions for flow of non-Newtonian fluids in porous media revisited under parameter uncertainty. **Adv. Water Resour.**, v. 43, p. 38–51, 2012.

54 CIRIELLO, V.; Di Federico, V. Analysis of a benchmark solution for non-newtonian radial displacement in porous media. **Int. J. Non Linear Mech.**, v. 52, p. 46–57, 2013.

55 TENNOE, S.; HALNES, G.; EINEVOLL, G. T. Uncertainpy: A python toolbox for uncertainty quantification and sensitivity analysis in computational neuroscience. **Front. Neuroinform.**, v. 12, 2018.

56 LOTFOLLAHI, M.; KIM, I.; BEYGI, M. R.; WORTHEN, A. J.; HUH, C.; JOHNSTON, K. P.; WHEELER, M. F.; DICARLO, D. A. Experimental Studies and Modeling of Foam Hysteresis in Porous Media. In: **Improved Oil Recovery Conference**. Tulsa, USA: SPE, 2016.

57 MA, K.; LOPEZ-SALINAS, J.; PUERTO, M.; MILLER, C.; BISWAL, S.; HIRASAKI, G. Estimation of parameters for the simulation of foam flow through porous media. Part 1: the dry-out effect. **Energy Fuels**, v. 27, n. 5, p. 2363–2375, 2013.

58 VALDEZ, A. R.; ROCHA, B. M.; FAÇANHA, J. M. da F.; SOUZA, A. V. O. de; PÉREZ--GRAMATGES, A.; CHAPIRO, G.; SANTOS, R. W. dos. Foam-assisted water–gas flow parameters: From core-flood experiment to uncertainty quantification and sensitivity analysis. **Transp. Porous Media**, v. 144, p. 189–209, 2022.

59 MIRANDA, G. B.; RIBEIRO, L. S.; FAÇANHA, J. M. F.; PÉREZ--GRAMATGES, A.; ROCHA, B. M.; CHAPIRO, G.; SANTOS, R. W. Characterization of foam-assisted water-gas flow via inverse uncertainty quantification techniques. **Lect. Notes Comput. Sci.**, v. 13353, p. 310–322, 2022.

60 MIRANDA, G. de; RIBEIRO, L.; ROCHA, B.; FAçANHA, J.; Pérez-Gramatges, A.; SANTOS, R. D.; CHAPIRO, G. An improved approach for uncertainty quantification based on steady-state experimental data in foam-assisted enhanced oil recovery. In: **European Conference on the Mathematics of Geological Reservoirs**. The Hague, Netherlands: EAGE, 2022. p. 1–14.

61 VALDEZ, A. R.; ROCHA, B. M.; CHAPIRO, G.; dos Santos, R. W. Assessing uncertainties and identifiability of foam displacement models employing different objective functions for parameter estimation. **J. Pet. Sci. Eng.**, v. 214, n. 110551, 2022.

62 RIBEIRO, L. S.; MIRANDA, G. B.; ROCHA, B. M.; CHAPIRO, G.; SANTOS, R. W. d. On the identifiability of relative permeability and foam displacement parameters in porous media flow. **Water Resour. Res.**, v. 60, n. 3, 2024.

63 MIRANDA, G. B. de; SANTOS, R. W. dos; CHAPIRO, G.; ROCHA, B. M. Uncertainty quantification on foam modeling: The interplay of relative permeability and implicit-texture foam parameters. **Transp. Porous Media**, v. 152, n. 8, 2024.

64 DANELON, T.; PAZ, P.; CHAPIRO, G. The mathematical model and analysis of the nanoparticle-stabilized foam displacement. **Appl. Math. Model.**, v. 125, p. 630–649, 2024.

65 SOBOL', I. Global sensitivity indices for nonlinear mathematical models and their Monte Carlo estimates. **Math. Comput. Simul.**, v. 55, n. 1, p. 271–280, 2001.

66 DANELON, T.; ROCHA, B. M.; dos Santos, R. W.; CHAPIRO, G. Sensitivity analysis and uncertainty quantification based on the analytical solution for nanoparticle-stabilized foam flow in porous media. **Geoenergy Sci. Eng.**, v. 242, p. 213285, 2024.

67 DANELON, T.; FARAJZADEH, R.; BEDRIKOVETSKY, P.; CHAPIRO, G. Modeling nanoparticle-stabilized foam flow in porous media accounting for particle retention and permeability reduction. **To appear in Interpore Journal**, 2024.

68 LEVEQUE, R. J. **Finite volume methods for hyperbolic problems**. Cambridge: Cambridge University Press, 2002.

69 DAFERMOS, C. M. **Hyperbolic conservation laws in continuum physics**. [S.l.]: Springer, 2005. v. 3.

70 OLEĬNIK, O. A. On the uniqueness of generalized solution of Cauchy problem for non linear system of equations ocurring in mechanics. **Uspekhi Mat. Nauk**, v. 6, n. 78, p. 169–176, 1957.

71 BUCKLEY, S. E.; LEVERETT, M. C. Mechanism of fluid displacement in sands. **Transactions of the AIME**, Soc. Pet. Eng., v. 146, 1942.

72 WELGE, H. J. A Simplified Method for Computing Oil Recovery by Gas or Water Drive. **J. Pet. Technol.**, v. 4, n. 04, p. 91–98, 1952.

73 WALSH, M. P.; LAKE, L. W. Applying fractional flow theory to solvent flooding and chase fluids. **J. Pet. Sci. Eng.**, v. 2, n. 4, p. 281–303, 1989.

74 LAX, P. D. Hyperbolic systems of conservation laws II. **Commun. Pure Appl. Math.**, v. 10, n. 4, p. 537–566, 1957.

75 ROSSEN, W. R.; ZEILINGER, S. C.; SHI, J. X.; LIM, M. T. Simplified mechanistic simulation of foam processes in porous media. **SPE J.**, Soc. Pet. Eng., v. 4, n. 03, p. 279–287, 1999.

76 BEAR, J. **Modeling Phenomena of Flow and Transport in Porous Media**. [S.l.]: Springer Cham, 2018. (Theory and Applications of Transport in Porous Media).

77 COREY, A. The interrelation between gas and oil relative permeabilites. **Producers Monthly**, v. 19, n. 1, p. 38–41, 1954.

78 BROOKS, R. H.; COREY, A. T. Properties of porous media affecting fluid flow. **J. Irrig. Drain. Div.**, ASCE, v. 92, n. 2, p. 61–90, 1966.

79 GENUCHTEN, M. T. van. A Closed-form Equation for Predicting the Hydraulic Conductivity of Unsaturated Soils. **Soil Sci. Soc. Am. J.**, v. 44, n. 5, p. 892–898, 1980.

80 LOMELAND, F.; EBELTOFT, E.; THOMAS, W. H. A new versatile relative permeability correlation. In: **Society of Core Analysis Conference**. Toronto, Canada: Proceedings SCA, 2005.

81 CHIERICI, G. L. Novel relations for drainage and imbibition relative permeabilities. **Soc. Pet. Eng. J.**, v. 24, 1984.

82 DARCY, H. **Les fontaines publiques de la ville de Dijon**. Paris, France: Dalmont, 1856.

83 COLLINS, R. E. **Flow of fluids through porous materials**. Tulsa, OK: Petroleum Publishing, 1976.

84 MUSKAT, M.; MERES, M. W. The flow of heterogeneous fluids through porous media. **Physics**, American Institute of Physics, v. 7, n. 9, p. 346–363, 1936.

85 LI, K.; HORNE, R. N. Comparison of methods to calculate relative permeability from capillary pressure in consolidated water-wet porous media. **Water Resour. Res.**, v. 42, n. 6, 2006.

86 PURCELL, W. R. Capillary pressure - Their measurement using mercury and the calculation of permeability there form. **Transaction of AIME**, v. 1, n. 2, p. 39–48, 1949.

87 BURDINE, N. Relative permeability calculations from pore size distribution data. **Transaction of AIME**, v. 198, p. 71–78, 1953.

88 ISAACSON, E. L. **Global solution of a Riemann problem for a non-strictly hyperbolic system of conservation laws arising in enhanced oil recovery**. New York, USA: Rockefeller University, 1981.

89 JOHANSEN, T.; WINTHER, R. The solution of the Riemann problem for a hyperbolic system of conservation laws modeling polymer flooding. **SIAM J. Math. Anal.**, SIAM, v. 19, n. 3, p. 541–566, 1988.

90 THORAT, R.; BRUINING, H. Foam flow experiments. i. Estimation of the bubble generation-coalescence function. **Transp. Porous Media**, v. 112, n. 1, p. 53–76, 2016.

91 FRITIS, G. C.; PAZ, P. S.; LOZANO, L. F.; CHAPIRO, G. On the Riemann problem for the foam displacement in porous media with linear adsorption. **SIAM Applied Mathematics**, v. 84, n. 2, p. 581–601, 2024.

92 ZAVALA, R. Q.; LOZANO, L. F.; ZITHA, P. L. J.; CHAPIRO, G. Analytical solution for the population-balance model describing foam displacement. **Transp. Porous Media**, Springer, v. 144, n. 1, p. 211–227, 2022.

93 HIRASAKI, G. J.; LAWSON, J. B. Mechanisms of foam flow in porous media: Apparent viscosity in smooth capillaries. **SPE J.**, v. 25, n. 02, p. 176–190, 1985.

94 SHOJAEI, M. J.; MéHEUST, Y.; OSMAN, A.; GRASSIA, P.; SHOKRI, N. Combined effects of nanoparticles and surfactants upon foam stability. **Chem. Eng. Sci.**, v. 238, p. 116601, 2021.

95 PRIGIOBBE, V.; WORTHEN, A. J.; JOHNSTON, K. P.; HUH, C.; BRYANT, S. L. Transport of nanoparticle-stabilized CO_2-foam in porous media. **Transp. Porous Media**, v. 111, p. 265–285, 2016.

96 BORAZJANI, S.; DEHDARI, L.; BEDRIKOVETSKY, P. Exact solution for tertiary polymer flooding with polymer mechanical entrapment and adsorption. **Transp. Porous Media**, v. 134, p. 41–75, 2020.

97 KEYKHOSRAVI, A.; BEDRIKOVETSKY, P.; SIMJOO, M. Experimental insight into the silica nanoparticle transport in dolomite rocks: Spotlight on DLVO theory and permeability impairment. **J. Pet. Sci. Eng.**, v. 209, p. 109830, 2022.

98 ZHANG, T.; MURPHY, M. J.; YU, H.; BAGARIA, H. G.; YOON, K. Y.; NEILSON, B. M.; BIELAWSKI, C. W.; JOHNSTON, K. P.; HUH, C.; BRYANT, S. L. Investigation of nanoparticle adsorption during transport in porous media. **SPE Journal**, v. 20, n. 4, p. 667–677, 2015.

99 BABAKHANI, P.; BRIDGE, J.; DOONG, R.; PHENRAT, T. Continuum-based models and concepts for the transport of nanoparticles in saturated porous media: A state-of-the-science review. **Adv. Colloid Interface Sci.**, v. 246, p. 75–104, 2017.

100 RODRIGUEZ, E.; ROBERTS, M. R.; YU, H.; HUH, C.; BRYANT, S. L. Enhanced migration of surface-treated nanoparticles in sedimentary rocks. In: **Annual Technical Conference and Exhibition**. New Orleans, USA: SPE, 2009. p. 124418.

101 CALDELAS, F.; MURPHY, M. J.; HUH, C.; BRYANT, S. L. Factors governing distance of nanoparticle propagation in porous media. In: **Production and Operations Symposium**. Oklahoma City, USA: SPE, 2011. p. 142305.

102 DANESHFAR, R.; ASHOORI, S.; SOULGANI, B. S. Transport and retention of silica nanoparticles in glass-bead columns: effects of particle size, type, and concentration of ionic species. **Sci. Rep.**, v. 14, n. 685, 2024.

103 SAMENI, A.; POURAFSHARY, P.; GHANBARZADEH, M.; AYATOLLAHI, S. Effect of nanoparticles on clay swelling and migration. **Egypt. J. Pet.**, v. 24, n. 4, p. 429–437, 2015.

104 ARAIN, Z.; Al-Anssari, S.; ALI, M.; MEMON, S.; BHATTI, M. A.; LAGAT, C.; SARMADIVALEH, M. Reversible and irreversible adsorption of bare and hybrid silica nanoparticles onto carbonate surface at reservoir condition. **Petroleum**, v. 6, n. 3, p. 277–285, 2020.

105 HAJIABADI, S. H.; BEDRIKOVETSKY, P.; MAHANI, H.; KHOSHSIMA, A.; AGHAEI, H.; KALATEH-AGHAMOHAMMADI, M.; HABIBI, S. Effects of surface modified nanosilica on drilling fluid and formation damage. **J. Pet. Sci. Eng.**, v. 194, p. 107559, 2020.

106 ZHANG, T.; MURPHY, M.; YU, H.; HUH, C.; BRYANT, S. L. Mechanistic model for nanoparticle retention in porous media. **Transp. Porous Media**, v. 115, p. 387–406, 2016.

107 SUN, Q.; LIU, W.; LI, S.; ZHANG, N.; LI, Z. Interfacial rheology of foam stabilized by nanoparticles and their retention in porous media. **Energy Fuels**, v. 35, p. 6541–6552, 2021.

108 LYU, X.; VOSKOV, D.; MAO, J. Modeling of non-Newtonian polymer flooding with adsorption and retention using parametrization approach. In: **European Conference on the Mathematics of Geological Reservoirs**. The Hague, Netherlands: EAGE, 2022. p. 1–11.

109 FADILI, A.; MURTAZA, A.; ZITHA, P. Injectivity decline by nanoparticles transport in high permeable rock. **J. Pet. Sci. Eng.**, v. 211, p. 110121, 2022.

110 ZEINIJAHROMI, A.; FARAJZADEH, R.; (Hans) Bruining, J.; BEDRIKOVETSKY, P. Effect of fines migration on oil–water relative permeability during two-phase flow in porous media. **Fuel**, v. 176, p. 222–236, 2016.

111 CASCELLI, R. S. S.; SANTOS, T. F. C.; DANELON, T.; CHAPIRO, G. Modelagem matemática e computacional de subsidência em regiões afetadas pela dissolução de sal em Maceió/AL. In: **Encontro Nacional de Modelagem Computacional**. Ilhéus, Brazil: Proceedings ENMC, 2024. p. 521–530.

112 MCCLARREN, R. G. **Uncertainty quantification and predictive computational science**: A foundation for physical scientists and engineers. 1. ed. Switzerland: Springer Cham, 2018.

113 ECK, V. G.; DONDERS, W. P.; STURDY, J.; FEINBERG, J.; DELHAAS, T.; HELLEVIK, L. R.; HUBERTS, W. A guide to uncertainty quantification and sensitivity analysis for cardiovascular applications. **Int. J. numer. Method. Biomed. Eng.**, v. 32, n. 8, p. e02755, 2016.

114 SALTELLI, A.; ANNONI, P.; AZZINI, I.; CAMPOLONGO, F.; RATTO, M.; TARANTOLA, S. Variance based sensitivity analysis of model output. Design and estimator for the total sensitivity index. **Comput. Phys. Commun.**, v. 181, n. 2, p. 259–270, 2010.

115 MARELLI, S.; SUDRET, B. Qlab: A framework for uncertainty quantification in Matlab. In: **The 2nd International Conference on Vulnerability and Risk Analysis and Management**. Liverpool, United Kingdom: ASCE, 2014. p. 2554–2563.

116 MARELLI, S.; LAMAS, C.; KONAKLI, K.; MYLONAS, C.; WIEDERKEHR, P.; SUDRET, B. **UQLab user manual – Sensitivity analysis**. Zurich, Switzerland, 2022. Report UQLab-V2.0-106.

117 JANON, A.; KLEIN, T.; LAGNOUX, A.; NODET, M.; PRIEUR, C. Asymptotic normality and efficiency of two Sobol index estimators. **ESAIM Probab. Stat.**, v. 18, p. 342–364, 2014.

118 BARKVE, T. The Riemann problem for a nonstrictly hyperbolic system modeling nonisothermal, two-phase flow in a porous medium. **SIAM J. Appl. Math.**, v. 49, n. 03, p. 784–798, 1989.

119 LOZANO, L.; CHAPIRO, G.; MARCHESIN, D. Analytical investigation of the three-phase foam flow in porous media. In: **European Conference on the Mathematics of Geological Reservoirs**. Oslo, Norway: EAGE, 2024. p. 1–9.

120 KARAKASHEV, S. I.; OZDEMIR, O.; HAMPTON, M. A.; NGUYEN, A. V. Formation and stability of foams stabilized by fine particles with similar size, contact angle and different shapes. **Colloids Surf. A Physicochem. Eng. Asp.**, v. 382, p. 132–138, 2011.

121 CHAHAL, J. S. Solution of the cubic. **Resonance**, v. 11, n. 8, p. 53–61, 2006.

122 CARDANO, G. **The Great Art or The Rules of Algebra**. EUA: The MIT Press, 1968.

123 CASTAÑEDA, P. Dogma: S-shaped. **Math. Intell.**, v. 38, n. 2, p. 10–13, 2016.

124 RUDIN, W. **Principles of mathematical analysis**. EUA: McGraw-Hill, 1976. (International series in pure and applied mathematics).

125 ISAACSON, E. L.; TEMPLE, J. Analysis of a singular hyperbolic system of conservation laws. **J. Differ. Equ.**, v. 65, n. 2, p. 250–268, 1986.

126 SOUZA, A. J. de; MARCHESIN, D. Conservation laws possessing contact characteristic fields with singularities. **Acta Appl. Math.**, v. 51, n. 3, p. 353–364, 1998.

127 PETROVA, Y.; PLOHR, B. J.; MARCHESIN, D. Vanishing adsorption limit of riemann problem solutions for the polymer model. **J. Hyperbolic Differ. Equ.**, v. 21, n. 2, p. 299–327, 2024.

128 KEYFITZ, B. L.; KRANZER, H. C. A system of non-strictly hyperbolic conservation laws arising in elasticity theory. **Arch. Ration. Mech. Anal.**, Springer-Verlag, v. 72, n. 3, p. 219–241, 1980.

129 SCHECTER, S.; MARCHESIN, D.; PLOHR, B. J. Structurally stable Riemann solutions. **J. Differ. Equ.**, v. 126, n. 2, p. 303–354, 1996.

130 FURTADO, F. **Structural stability of nonlinear waves for conservation laws**. Ph.D. thesis: New York Univ., 1989.

131 BELLO, A.; DORHJIE, D.; IVANOVA, A.; CHEREMISIN, A.; CHEREMISIN, A. Reservoir modelling of nanoparticle-assisted foam to optimize gas injection in an unconsolidated heavy oilfield. In: **Gas & Oil Technology Showcase and Conference**. Dubai, UAE: SPE, 2023.

132 LAMBERT, W.; ALVAREZ, A.; LEDOINO, I.; TADEU, D.; MARCHESIN, D.; BRUINING, J. Mathematics and numerics for balance partial differential-algebraic equations (PDAEs). **J. Sci. Comput.**, Springer, v. 84, n. 2, p. 1–56, 2020.

133 ISAACSON, E. L.; MARCHESIN, D.; PLOHR, B. J. Transitional waves for Conservation Laws. **SIAM J. Math. Anal.**, v. 21, n. 4, p. 837–866, 1990.

134 CASTAÑEDA, P.; ABREU, E.; FURTADO, F.; MARCHESIN, D. On a universal structure for immiscible three-phase flow in virgin reservoirs. **Comput. Geosci.**, v. 20, p. 171–185, 2016.

135 DANELON, T.; CHAPIRO, G. Análise de incertezas para escoamento em meios porosos de espuma estabilizada por nanopartículas. In: **Encontro Nacional de Modelagem Computacional**. Ilhéus, Brazil: Proceedings ENMC, 2024. p. 531–540.

136 CURTIS, A. R. Solution of cubic and quartic equations. **J. RAeS**, Cambridge University Press, v. 70, n. 668, p. 819–820, 1966.

137 TAO, T.; WATSON, A. Accuracy of JBN estimates of relative permeability: Part 1 - Error analysis. **Soc. Pet. Eng. J.**, v. 24, n. 2, p. 209–214, 1984.

138 TAO, T.; WATSON, A. Accuracy of JBN estimates of relative permeability: Part 2 - Algorithms. **Soc. Pet. Eng. J.**, v. 24, n. 2, p. 215–223, 1984.

139 LI, Y.; WANG, Y.; PENNELL, K.; ABRIOLA, L. Investigation of the transport and deposition of fullerene (C60) nanoparticles in quartz sands under varying flow conditions. **Environ. Sci. Technol.**, v. 42, n. 19, p. 7174–7180, 2008.

140 WANG, Y.; LI, Y.; FORTNER, J.; HUGHES, J.; ABRIOLA, L.; PENNELL, K. Transport and retention of nanoscale C60 aggregates in water-saturated porous media. **Environ. Sci. Technol.**, v. 42, n. 10, p. 3588–3594, 2008.

141 TUFENKJI, N.; ELIMELECH, M. Deviation from the classical colloid filtration theory in the presence of repulsive DLVO interactions. **Langmuir**, v. 20, n. 25, p. 10818–10828, 2004.

142 BEDRIKOVETSKY, P.; MARCHESIN, D.; SHECAIRA, F.; SOUZA, A.; MILANEZ, P.; REZENDE, E. Characterisation of deep bed filtration system from laboratory pressure drop measurements. **J. Pet. Sci. Eng.**, v. 32, n. 2, p. 167–177, 2001.

143 ZHANG, T. **Modeling of nanoparticle transport in porous media**. Ph.D. thesis: The University of Texas at Austin, 2012.

144 KHOSRAVI, R.; CHAHARDOWLI, M.; KEYKHOSRAVI, A.; SIMJOO, M. A model for interpretation of nanoparticle-assisted oil recovery: Numerical study of nanoparticle-enhanced spontaneous imbibition experiments. **Fuel**, v. 292, p. 120174, 2021.